

**MATERIALS, SENSORS, AND MANUFACTURING METHODS FOR  
NEXT GENERATION OF PERSONAL PROTECTIVE EQUIPMENT**

**MATERIALS, SENSORS, AND MANUFACTURING METHODS FOR  
NEXT GENERATION OF PERSONAL PROTECTIVE EQUIPMENT**

By RONG WU, M.Sc.

A Thesis Submitted to the School of Graduate Studies in Partial Fulfilment of the  
Requirements for the Degree Doctor of Philosophy in Mechanical Engineering

McMaster University

© Copyright by Rong Wu, March 2023

DOCTOR OF PHILOSOPHY (2023)

Graduate Program in Department of Mechanical Engineering

McMaster University, Hamilton, Ontario, Canada.

TITLE: Materials, sensors, and manufacturing methods for next generation personal  
protective equipment

AUTHOR: Rong Wu  
M.Sc. (McMaster University, Hamilton, Canada)

SUPERVISOR: Dr. P. Ravi Selvaganapathy

PAGES: xxvii, 190

## **LAY ABSTRACT**

Personal Protective Equipment (PPE) is equipment worn to minimize exposure to hazards that cause injuries and illnesses in both the workplace and daily life. During the COVID-19 pandemic, there was a severe shortage of PPE worldwide due to the high demand for this equipment. This shortage drew people's attention to the manufacturing methods of PPE and how to overcome such difficulties during future pandemics. Meanwhile, most PPE is single-use, leading to problems regarding recycling and disposal. The main material used for PPE is Polypropylene, which is not biodegradable but can be recycled at an extra labor cost. To solve this issue, alternative materials with natural-based polymers would be ideal. Additionally, if PPE can provide specialized functions beyond protection, such as indicators or alarms, it could be especially helpful in work environments. For some industries, harmful gases exist that could lead to severe hazards after long or over-limit exposure. Workers would benefit from integrated indicators/sensors with essential PPE that provide a naked-eye-readable response, as this would eliminate the need to wear extra devices and instruments to detect and interpret signals. In other circumstances, such as deep-sea operations and the mining industry, it is important to monitor workers' physiological signals, as most medical instruments are not achievable. If a worker's physiological signal is outside the normal range, they will receive an alert to get out of the working environment and receive treatment. In this thesis, we focus on all the perspectives mentioned above. We have designed a new full-head face shield to replace the combination of a face mask and conventional face shield. Our proposed in-home fabrication method eases the difficulty level compared to traditional manufacturing methods that require industrial instruments. In addition, we use natural proteins from corn to produce a filtration material with decent performance that is also biodegradable.

Finally, we produce sensors for external harmful gas detection and user's physiological signal detection, which are implanted in the PPE material to provide both protection and indication. Overall, we have developed the next generation of PPE with improved design, manufacturing methods, materials, and sensors.

## **ABSTRACT**

Air quality including presence of different kinds of harmful chemicals and particles is an important factor for human health. Various designs of protective equipment are currently available commercially mainly focusing on one-time/short-term use in industrial environments based on using microfibrinous polypropylene to provide passive protection. During the COVID-19 pandemic, the significant shortage of PPE caused severe problem worldwide. In this thesis, we have developed a new one-piece full head and face respirator with high filtration efficiency, designed to be manufactured without industrial equipment. The environmental impact of PPE has led to interest in using natural polymers for filter materials due to their sustainability and biodegradability. We have developed a compostable zein based air filter produced by electrospinning on a craft paper-based substrate to reducing their environmental impact. The electrospun filter material is tailored to be humidity tolerant and mechanically durable by crosslinking zein with citric acid. We used a folding structure to significantly reduce pressure drop during both single filtration and long-term testing, without compromising other performances.

We also aim to develop smart PPEs that can sense the toxic contamination in surroundings and monitor physiological conditions of wearer which is necessary in different circumstances. For detecting harmful substance exposure, we demonstrated a one-step fabrication method for a colorimetric, sensitive, and selective ammonia platform. This sensor was based on simple pH-indicator immobilization electrospun mat with ability to detect concentrations of ammonia as low as 0.5 ppm in a fast response time of 10 sec. We highlighted the durable stability for gaseous and liquid interferences owing to its core-shell nanofiber structure. In other worksites, such as under water or mining industries, the non-availability of medical instruments makes it more important to

get real-time monitor of physiological signal to prevent accident. We developed the laser induced graphene-based glucose sensor with one step fabrication on Polycarbonate which is the material of the face shield. The proposed sensor had the sensitivity at  $70.1 \mu\text{A mM}^{-1} \text{cm}^{-2}$  with the detection range from 0.01 mM to 10 mM. The performance enabled the sensor to be used to monitor glucose level in sweat by implement in the face shield. Overall, we have demonstrated the development of new materials and manufacturing methods for next generation functional PPE. The active sensing function was achieved by two categories of sensor implementation: active protection with toxic gas-ammonia detection, and health monitoring function with glucose sensing.

## **ACKNOWLEDGEMENT**

Firstly, to my supervisor, Dr. Ravi Selvaganapathy, I want to express my acknowledgement to your mentorship throughout my Master and PhD career, the freedom he provided to pursue my ideas, encouraging me to collaborate with groups my interests aligned with, allowing me to explore multiple different fields. I am very grateful for your patient to listening all my concepts, and your wiliness to provide feedback to polish those ideas, and the time you spent for the individual meeting. Thank you for your understanding and caring throughout my PhD.

I am also grateful to my committee member, Dr. Chan Y. Ching and Dr. Mohammed Tauhiduzzaman for taking the time to provide me with advice and guidance on my PhD research. The discussions helped me to have a more comprehensive understanding and different perspective for my research.

I would also like to thank my family and friends, my parents, my husband for the strong support and love throughout my life. I can never thank you enough for the efforts and everything you did to make me as I am today.

Finally, I want to thank to all my labmates and collaborators, Nidhi, Sneha, Mehraneh, Liang, Rakesh, Ria, Fathalla, Islam, Neda, Shadi, Aydin, Anand, Alireza, Sreekant, Vinay, Maedeh, Panashe and Hareshan to your support and you make this journey more enjoyable, colorful and memorable.

## TABLE OF CONTENTS

Chapter 1: Introduction .....	1
1. Wearable protective equipment .....	1
1.1 Importance of wearable health protective equipment .....	1
1.2 Design of protective equipment .....	3
1.3 Manufacturing of filter material.....	5
1.3.1 Meltblown technology .....	5
1.3.2 Spunbond technology.....	7
1.3.3 Electrospinning technology .....	8
1.4 Material of protective equipment filter .....	12
1.4.1 Synthetic polymer based protective filter .....	12
1.4.2 Natural polymers and its combination with synthetic polymer for protective filter	18
2. Wearable sensors integrated with protective equipment .....	20
2.1 Importance of wearable sensors embedded in PPE .....	20
2.2 Ammonia sensor .....	21
2.2.1 Conductometric Metal oxide-based sensor for ammonia .....	21
2.2.2 Optical and colorimetric sensor for ammonia.....	23
2.3 Wearable glucose monitor sensor .....	28
2.3.1 Wearable tear glucose sensor.....	30

2.3.2 Wearable saliva glucose sensor .....	31
2.3.3 Wearable ISF glucose sensor .....	32
2.3.4 Wearable breath glucose sensor .....	33
2.3.5 Wearable sweat glucose sensor.....	34
2.3.6 Laser induced graphene based glucose sensor.....	36
3. Summary .....	36
4. Objectives of the thesis .....	38
5. Thesis organization .....	38
6. Research contributions.....	40
References.....	42
Chapter 2: Development of a one-piece full-head covered respirator with clear face visor for greater personal protection.....	62
Abstract.....	63
1. Introduction.....	64
2. Methods and materials .....	66
2.1 Fabrication of full face respirator prototypes.....	66
2.2 Relative humidity, temperature and CO <sub>2</sub> level tests .....	67
2.3 Particle filtration efficiency tests .....	68
3. Results.....	71

4. Discussion .....	75
5. Conclusions .....	78
References .....	79
Chapter 3 Efficient, Breathable, and Compostable, Multi-Layer Air Filter Material Prepared from Plant Derived Biopolymers .....	83
Abstract: .....	84
1. Introduction .....	85
2. Materials and Methods .....	87
2.1 Materials .....	87
2.2 Preparation of electrospinning solution .....	87
2.3 Preparation of electrospinning substrates .....	88
2.4 Electrospinning process .....	88
2.5 Preconditioning under humid conditions .....	90
2.6 Determination of filtration efficiency and pressure drop .....	91
2.7 Mechanical folding .....	91
2.8 Biodegradability .....	91
2.9 Surface characterization .....	92
3. Results and Discussion .....	93
3.1 Morphology of the composite zein filter and filtration performance .....	93

3.2 Effect of crosslinking .....	96
3.2.1 Morphology and air filtration performance .....	96
3.2.2 Effect of humidity on filtration performance .....	96
3.2.3 Mechanical handling stability .....	99
3.3 Air filtration performance of pleated electrospun filter .....	100
3.4 Stacking of electrospun zein filters .....	102
3.5 Extended filtration performance of composite zein filter .....	104
3.6 Biodegradability .....	107
4. Conclusions .....	109
References .....	110
Supplementary Information .....	116
Chapter 4 Porous biocompatible colorimetric nanofiber-based sensor for selective ammonia detection on personal wearable protective equipment .....	124
Abstract .....	125
1. Introduction .....	126
2. Experimental section .....	129
2.1 Materials .....	129
2.2 Preparation of electrospinning sensors .....	129
2.3 Sensor Surface characterizations .....	131

2.4 Colorimetric ammonia detection of bi-polymer sensors.....	131
3. Results and discussion .....	132
3.1 Spincoated PDMS for water repellent sensor performance .....	132
3.2 Fabrication of bi-polymer co-axial nanofiber sensors .....	134
3.3 Sensitivity performance of colorimetric ammonia sensor .....	138
3.4 Detection selectivity and interference performance of colorimetric ammonia sensor..	143
3.5 Reversibility performance of colorimetric ammonia sensor.....	146
4. Conclusion .....	147
Reference .....	148
Appendix 4 Supplementary Information .....	152
Chapter 5 Highly conductive superhydrophobic laser-induced porous hierarchical graphene film from polycarbonate and applications .....	153
1. Introduction.....	154
2. Materials and methods .....	155
2.1 Materials .....	155
2.2 Fabrication of LIG on PC polymer .....	156
2.3 Characterization .....	156
3. Results and discusstion .....	157
3.1 PC-LIG formation and laser parameters optimization.....	157

3.2 Analytical characterization of PC-LIG .....	162
3.3 Properties of PC-LIG .....	165
4. Applications .....	168
4.1 Electrochemical glucose sensor .....	169
4.2 Contact electrodes for chemiresistive sensor .....	172
4.3 Others .....	175
5. Conclusion .....	176
Reference .....	177
Appendix 5 Supplementary Information .....	186
Chapter 6 Conclusions and future direction.....	190
1. Conclusions.....	190
2. Future directions .....	192
2.1 Functional natural polymer-based filter materials for face mask application .....	192
2.2 Gas sensing .....	193
2.3 Physiological condition monitor .....	194
Reference .....	195

## LIST OF FIGURES AND TABLES

<b>Table 1.1</b> Summary of standards applicable to face coverings or face masks and respirators. ....	3
<b>Figure 1.1</b> Schematic diagram of the meltblown line [27]. .....	7
<b>Figure 1.2</b> Schematic diagram of the spun-bond process[28].....	8
<b>Figure 1.3</b> Schematic diagram of electrospinning setup (a) vertical (b) horizontal [40]. .....	9
<b>Figure 1.4</b> Schematic diagrams of electrospinning collectors (a) rotating drum, (b) wire drum, (c) disk, (d) parallel electrode, (e) mesh electrode; (f) core-shell nozzle and transmission electron microscopy (TEM) image of the coaxial PANI/PVA fiber; multi-nozzle system of (g) linear, (h) square array, (i) concentric. [Adapted from [41-47]] .....	10
<b>Figure 1.5</b> Parameter map affecting electrospinning process .....	11
<b>Figure 1.6</b> Meltblown fiber with different synthetic polymers (a) Schematic and SEM of the multilayered PP air filter; (b) Schematic and SEM of PP/PC meltblown resin with synthesis of Zeolitic imidazolate framework-8 (ZIF- 8); (c) SEM images of the morphology of PP/MgSt filter; (d) SEM images of the morphology of PLA fiber(Adapted from [25, 61-63]). .....	14
<b>Figure 1.7</b> (a) SEM of three-layer respirators with Spun-bond-Meltblown-Spun-bond combination, (b) the cross section of the PE/PP bicomponent fiber, (c)-(d) Energy-dispersive X-ray mapping images of C, Mg in Mgst-PE/PP, (e) SEM images of PTFE/EG1 on PP spun-bond fabric, (f) The cross section of PET-PA6 hollow segment-pie bicomponent fibers, (g) SEM images of the cross-sectional of lcPET/ PA6 fiber and the surface of PET/PA6 and lcPET/PA6 fibers, (h)-(l) SEM images of INS webs with several number of islands in the sea: 1, 7, 19, 37, and 108.(Adapted from [64-70]). .....	16
<b>Figure 1.8</b> (a)-(d) SEM images and fiber diameter distribution of Zein round and robbin like fibers with different concentration of solvent; (e) Schematic and SEM images of chitosan nanowhisker with PBS fiber (Adapted from [79, 84]). .....	20
<b>Figure 1.9</b> Schematic of TLAS for gas detection (Reproduced from [86]) .....	24
<b>Figure 1.10</b> (a) SEM images of yarn PbI <sub>2</sub> ; (b) In situ time-dependent $\Delta E$ values depend on NH <sub>3</sub> concentration (1, 10, 25, 50, and 100 ppm) using yarn PbI <sub>2</sub> ; (c) Reaction mechanism of the pH	

indicator BPB for the detection of NH<sub>3</sub>; (d) Optical images of BTB, MR, and MnTPP devices and the corresponding RGB color information extracted from the optical images for different concentrations of ammonia (Adapted from [99, 102]). ..... 26

**Figure 1.11** Evolution of glucose sensors from (a) continuous glucose monitor, (b) self-monitoring glucose device; (c) noninvasive or minimally-invasive detection [111] ..... 30

**Table 1.2** Glucose concentration range of different fluid types ..... 30

**Figure 2.1** Schematic of fabrication process for the full head face shield ..... 70

**Figure 2.2** Particle filtration efficiency test setup with breathing simulator ..... 71

**Figure 2.3** Relative temperature and humidity within the faceshield with time for (a)-(b) male participant and (c)-(d) female participant ..... 73

**Figure 2.4** Humidex comfort within the faceshield with time for (a) male participant and (b) female participant ..... 74

**Figure 2.5** Carbon dioxide level (ppm) within the full-face respirator with time for (a) male participant and (b) female participant. .... 77

**Figure 2.6** Filtration efficiency of the full-face respirator at different flow rates ..... 77

**Table 3.1** Electrospinning conditions for varying zein concentrations. .... 89

**Figure 3.1** Schematic of process for preparing compostable multi-layer electrospun air filter (a) Zein solution preparation (b) Electrospinning substrate preparation and (c) Multinozzle electrospinning and stacked filter assembly. .... 91

**Figure 3.2** SEM of (a) 25 %, (b) 30 %, (c) 40 % fibers under magnification of 8000x and fiber diameters of (d) 25 %, (e) 30 %, (f) 40 % of crosslinked zein solution; Air filtration including PFE and PD performance of (g) 25 %, (h) 30 %, (i) 40 % with three different electrospinning time from 5 to 25 minutes. .... 95

**Figure 3.3** (a) SEM uncrosslinked zein fiber; (b) SEM of crosslinked zein fibers; (c) SEM of uncrosslinked zein fiber exposed to moisture for 60 minutes; (d) SEM of crosslinked zein fiber exposed to moisture for 60 minutes exposed to moisture; (magnification 8000x applied under SEM)

(e) uncrosslinked zein fiber diameter distribution; (f) crosslinked zein fiber diameter distribution. .... 98

**Figure 3.4** PFE and PD of a) uncrosslinked zein filter with different time of conditioning; (b) crosslinked zein filter with different time of conditioning; (c) uncrosslinked; and (d) crosslinked zein filter after mechanical handling..... 100

**Figure 3.5** (a) Stacking study of zein filter with flat, pre-pleated and pleated surface. (b) Comparison of quality factors (Qf) between this work with different flow rate and previous studies of synthetic polymer-based as well as natural polymer-based air filters [8, 28-31] The digit after the hyphen on data labels indicates the flow rate in cm/s used in these studies. .... 104

**Figure 3.6** (a) air filtration performance of 60-minute loading test of flat, pre-pleated, and pleated zein filter; (b) air filtration performance of 60-minute loading test of flat and pleated commercial Polypropylene mask filter; Schematic and SEM image of (c) peak, (d) side wall, and (e) trench of top pleated filter; (f) peak, (g) side wall, and (h) trench of bottom pleated filter. .... 107

**Figure 3.7** Biodegradability of the developed composite zein filter (a) Zein filter degradation with 28 days (b) Cellulose filter paper degradation with 28 days. . .... 108

**Figure S3.1** (a) SEM figure of crafted tissue paper substrate (b)Cracks on uncrosslinked zein filter after humidity conditioning for 1 hour; (c) un-uniform coverage of pleated filter along the fold lines. .... 117

**Figure S3.2** PFE and PD performance with different pleat width. .... 118

**Figure S3.3** PFE and PD of pleated crosslinked zein filter at (a) 5 min; (b) 15 min; (c) 25 min, (d) PFE and PD of 2-layer stack of pleated zein filter at various face velocities. .... 119

**Figure S3.4** SEM images of (a) flat zein filter, (b) pre-pleated zein filter, after one hour loading test. .... 120

**Figure S3.5** FTIR spectrum of paper substrate, crosslinked and uncrosslinked zein electrospun layer with paper substrate. .... 121

**Figure S3.6** Photograph of NE300 electrospinner. .... 122

**Figure S3.7** Photograph of TSI 8130A for filtration..... 122

**Figure 4.1** (a) Schematic showing the bi-polymer solution preparation. First, 10 wt% of PCL was prepared and then BPB, PDMS with different ratio to PCL was added into the solution for continuous stirring. (b) Schematic of electrospinning setup. A horizontal configuration was used consisting of syringe pump, flat PP covered aluminum collector and a high voltage supply. (c) Schematic of test chamber setup. The prepared gases were controlled by MFC and mixed in the mixing channel then exposed to sensors in the test chamber with camera monitoring. .... 130

**Figure 4.2** (a) Optical photographs of sensor with spin-coated PDMS on electrospun PCL before and after ammonia exposure. (b) Spin-coated sensor response curve to various concentrations of ammonia..... 134

**Figure 4.3** (a)-(e) SEM images of samples with various ratio of PCL and PDMS. (f)-(h) Fiber diameter distribution of samples with various ratio of PCL and PDMS. .... 136

**Figure 4.4** SEM of bi-polymer fiber after acetone immersion..... 137

**Figure 4.5** FTIR of samples with PCL and PCL/PDMS with different ratios. .... 138

**Figure 4.6** The room temperature optical photos of colorimetric sensors with different dye concentration from D1-0.5%, D2-1%, D3-2%, D4-3% (a) before and (b) after ammonia exposure. (c) Relationship of the color change to the dye concentration..... 140

**Figure 4.7** Time-dependent color change of bi-polymer sensor with different ratio of PDMS to PCL (a) R1-1:1, (b) R2-2:1, (c) R3-3:1, (d) R4-4:1, when exposed to various concentration of ammonia..... 141

**Figure 4.8** (a) Maximum color change of samples with polymer ratio from 1:1 to 1:4. (b)Maximum response time of samples with polymer ratio from 1:1 to 1:4. .... 141

**Figure 4.9** (a) Concentration dependent color change of bi-polymer sensor with different ratio of PDMS to PCL. (b) The color change ( $\Delta E$ ) of bi-polymer sensor to different VOCs exposure. 143

**Figure 4.10** Humidity dependence (from 0%, 30%, 50% up to 95%) of sensor response with different dye concentration from 0.5% to 2%. The inserts are the optical images of sensor with 1% dye concentration exposed to various relative humidity levels. .... 144

**Figure 4.11** (a) Optical photograph of the sensor exposed to liquids with high pH solution of (a) bare PCL sensor and (b) bi-polymer sensor with various dye ratio samples. .... 146

**Figure S4.1** Photograph of the chamber for sensor response monitoring. .... 152

**Figure 5.1** (a) Schematic of laser irradiation on polycarbonate film; (b-c) Characterization of surface morphology of PC-LIG-500-20 under SEM with different magnifications; (d) HRTEM images PC-LIG-500-20 showing graphene crystalline; (e) Wettability of PC and PC-LIG with sessile water droplet; (f) Raman spectra of PC film and LIG-500-20; (g) XRD spectra for PC film and LIG-500-20. .... 160

**Figure 5.2** (a) The relationship between laser scanning speeds and powers to achieve graphitization on polycarbonate film. (b) Transformation process of polycarbonate film under various laser power from low to high. (c) SEM Characterization of surface morphology of PC- under different magnification of LIG-300-10, and LIG-300-20. (d) HRTEM images of LIG-300-10, and LIG-300-20 showing graphene crystalline and amorphous carbon structures. .... 162

**Figure 5.3** Characterization and properties of LIG-PC produced with various laser settings. (a) XRD spectra for LIG-300-10, LIG-300-20, and LIG-500-20; (b) Raman spectra of LIG-300-10, LIG-300-20, LIG-500-20 and LIG-500-40; (c) Sheet resistance of PC-LIG under various laser parameters within graphitization range; (d) Sheet resistance change of LIG-500-20 with 100 bending cycles; (e) contact angle of PC-LIG under various laser parameters within graphitization range (f) The electrochemical CV response of LIG-500-20 sample with 10 cycles. .... 165

**Figure 4.** Dynamic water impact test under high-speed camera on LIG-500-20 sample showing droplet bounces. .... 168

**Figure 5.5** Potential applications of PC-LIG ..... 169

**Figure 5.6** (a) Schematic of the synthesis of PC-LIG with AuNPs for glucose sensing; (b) TEM images of Au-PC-LIG; (c) The high-resolution HAADF-STEM diagram of Au-PC-LIG and EDX color mapping of (d) C, (e) Au; (f) XRD spectra for PC-500-20 and Au-PC-LIG; (g) Amperometric response of the Au-PC-LIG sensor to different concentrations of glucose. The inset illustrated a partial magnification of glucose measurement at low concentrations. (h) The corresponding glucose standard curve of Au-PC-LIG sensor (n = 3). .... 171

**Figure 5.7** (a) Schematic of fabrication of chemiresistive sensors on polycarbonate substrate with LIG contact electrodes and airbrushed CNT; (b) Sensor response for 5 different free chlorine concentrations (n=4); (c) The correlation between resistance and temperature of PC-LIG based temperature sensor (n=3). (d) Temperature variation of PC-LIG electrical heater under different electrical powers. .... 175

**Table S5.1** The scan speed conversion..... 186

**Figure S5.1** TEM images of LIG-300-10, LIG-300-20, LIG-500-20..... 186

**Figure S5.2** Sheet resistance characterization of repeat treatments on same LIG-500-20 sample. .... 186

**Figure S5.3** SEM image with hierarchical fluffy graphene of LIG-500-20..... 187

**Figure S5.4** Durability of superhydrophobicity of PC-LIG sample with (a) initial immersion in water; (b) 48 hours immersion in water. The surface of PC-LIG was covered by a clear air layer in water indicated the excellent superhydrophobicity of proposed sample. .... 187

**Figure S5.5** CV response of Au-PC-LIG sensor with and without the addition of 1mM glucose in 0.1M NaOH solution..... 188

**Figure S5.6** The parallel line design for the PC-LIG temperature sensor with copper tape connected by silver paste ..... 188

**Figure S5.7** Preliminary results of PC-LIG as electrical heater. (a-b) Temperature distribution of PC-LIG electrical heater with power supply. .... 189

**Figure S5.8** Photograph of Glowforge CO<sub>2</sub> laser machine..... 189

## LIST OF ALL ABBREVIATIONS AND SYMBOLS

3D	Three-dimensional
Ag/AgCl	Silver-silver chloride
AgNPs	Silver nanoparticles
AlGa <sub>0.5</sub> N/GaN	Aluminium gallium nitride/gallium nitride
Ar	Argon
Au	Gold
AuNPs	Gold nanoparticles
BCG	Bromocresol green
BCP	Bromocresol purple
BPB	Bromophenol blue
BTB	Bromothymol blue
C <sub>2</sub> H <sub>4</sub>	Ethylene
C <sub>2</sub> H <sub>5</sub> OH	Ethanol
CO	Carbon monoxide
CO <sub>2</sub>	Carbon dioxide
COVID-19	Coronavirus disease 2019
CR	Cresol red
CuNPs,	Copper nanoparticles
CV	Cyclic voltammetry
DCM	Dichloromethane

DI water	Deionized water
DMF	N,N- dimethylformamide
EC	Ethyl cellulose
EDX	Energy Dispersive X-Ray
EG	expanded graphite
EtOH	anhydrous ethanol
FF	Fit factor
FFR	Filtering facepiece respirators
FTIR	Fourier transform infrared
GDH	glucose dehydrogenase
GOx	glucose oxidase
H <sub>2</sub>	Hydrogen
HAADF-STEM	High-angle annular darkfield scanning transmission electron microscopy
HEMTs	high electron mobility transistors
HRTEM	high-resolution transmission electron microscopy
In <sub>2</sub> O <sub>3</sub>	Indium oxide
INS	islands-in-the sea
ISF	interstitial fluid
K <sub>3</sub> [Fe (CN) <sub>6</sub> ]	potassium hexacyanoferrate III
K <sub>4</sub> [Fe (CN) <sub>6</sub> ]	potassium hexacyanoferrate II
KCl	Potassium chloride

LCPET	Low crystallinity PET
LIG	laser-induced graphene
LOD	Limit of detection
LPM	Liter per minute
MB	Meltblown
MFC	mass flow controllers
MgSt	Magnesium stearate
MnTPP	5,10,15,20-Tetraphenyl-21H,23H-porphine manganese (III) chloride
MoO <sub>3</sub>	Molybdenum trioxide
MR	Methyl red
N <sub>2</sub>	Nitrogen
NaHCO <sub>3</sub>	Sodium bicarbonate
NaOH	sodium hydroxide
NH <sub>3</sub>	Ammonia
NO <sub>2</sub>	Nitrogen dioxide
O <sub>2</sub>	Oxygen
OSHA	Occupational Safety and Health Administration
PA6	nylon-6
PAN	Polyacrylonitrile
PANI	Polyaniline
PB	Prussian blue

PbI <sub>2</sub>	Lead(II) iodide
PC	Polycarbonate
PCL	Polycaprolactone
PD	Pressure Drop
Pd	Palladium
PDMS	Polydimethylsiloxane
PE	Polyethylene
PEI	Polyethylenimine
PEL	Permissible Exposure Limit
PEO	polyethylene oxide
PET	Polyester
PFE	Particle Filtration Efficiency
PHEIC	public health emergency
PI	Polyimide
PI	Polyimide
PLA	Polylactic acid
PM	Particulate matter
PMMA	Poly(methyl methacrylate)
PP	Polypropylene
PPE	Personal Protective equipment
PPM	Parts per million
PSA	Pressure sensitive adhesive

PSF	Polysulfone
Pt	Platinum
PTFE	polytetrafluoroethylene
PtNPs	Platinum nanoparticles
PVA	Polyvinyl Alcohol
PVB	Poly(vinyl butyral)
PVDF	Polyvinylidene fluoride
QF	quality factor
RGO	Reduced graphene oxide
RH	Relative humidity
RI	Reverse iontophoresis
SEM	Scanning Electron Microscopy
SnO <sub>2</sub>	Tin dioxide
SWCNT	single-walled carbon nanotube
TB	Thymol blue
TEM	Transmission electron microscopy
TiO <sub>2</sub>	Titanium dioxide
TLAS	Tunable laser absorption spectroscopy
VOC	Volatile Organic Compound
WHO	World Health Organisation
WO <sub>3</sub>	Tungsten trioxide
XRD	X-ray diffraction

ZIF- 8	Zeolitic imidazolate framework-8
ZnO	Zinc oxide

## **DECLARATION OF ACADEMIC ACHIEVEMENT**

Rong Wu contributed to the conception, literature search, writing, experimental design, conducting experiments, data analysis, results interpretations, and figure generation for all the chapters of this thesis.

P. Ravi Selvaganapathy contributed to formulating the concepts, experimental design, data interpretation and revision of all the chapters of the thesis.

Panashe Mudzi and Dariush Firouzi contributed to the experimental design, conducting experiments, data interpretation, writing of Chapter 2 of this thesis.

Chan Y. Ching contributed to the formulating the concepts, experimental design, data interpretation and revision of Chapter 2 of this Thesis.

Sneha Shanbhag contributed to initiating concepts, experimental design, conducting experiment data interpretation and writing of Chapter 3 of the thesis.

Mehraneh Tavakkoli Gilavan Contributed to experimental design, conducting experiment data interpretation, and writing of Chapter 5 of the thesis.

Liang Fan contributed to formulating the concept and experiment design for chapter 5 of the thesis.

Md Ali Akbar provided the Raman spectral measurements in Chapter 5.

## **Chapter 1: Introduction**

### **1. Wearable protective equipment**

#### **1.1 Importance of wearable health protective equipment**

Air quality is an important factor for human health for both daily life and in an industrial environment. There are different kinds of harmful chemicals released to the surrounding environment due to human or industrial activities. Therefore, there is a need for suitable monitoring method such as a sensor to detect them rapidly and reliably. In addition, there is also a need to protect personnel from their harmful effects in case there is a release of these and many other harmful contaminants. Study of air quality in the environment and development of mitigation methods has been become an important topic of research and development worldwide. Air pollution, including particulate matter (PM) like carbon particulates, mineral dust, aerosols, toxic gases, and biological pollutants are increasingly responsible for a range of respiratory diseases such as lung cancer, ischemic heart disease and infections leading to 3.3 million deaths per year [1], and detrimental effects on the global climate [2]. For instance, PM particles in the atmosphere environment can lead to visibility reduction by 30%, form deposits on surfaces causing damage and defacement [3] [4]. Air quality in closed settings such as within buildings is also affected by human activity and can lead to spread of biological (bacterial and viruses), particulate matter, chemical contaminants (noxious gases). Advanced air filters are currently being developed to target highly efficient removal of a range of particulate matter such as particles with an average diameter of 10 microns, 2.5 microns or 0.3 microns, while also demonstrating low pressure drop for breathability or reduced energy consumption. More development is needed in protecting against biological and chemical contaminants especially in indoor settings.

There are two main parameters to evaluate the performance of air filtration system or material, namely Particle Filtration Efficiency (PFE) and Pressure Drop (PD). PFE is defined as the ratio of the particles passing through the filter system with that launched at it as shown in Eq.1. PD which is the pressure difference, is also known as air resistance is a measure of breathability and is shown in Eq.2.

$$PFE = \eta = \left(1 - \frac{n_1}{n_2}\right) \times 100\% \quad \text{Eq.1}$$

$$PD = \Delta P = P_2 - P_1 \quad \text{Eq.2}$$

Where  $n_1$  and  $P_1$  is the particle quantity and pressure after passing the filtration system,  $n_2$  and  $P_2$  is the particle quantity and pressure before passing the filtration system.

In the context of air filters, especially for facemask applications, standards and regulations such as ASTM F2100 (medical face masks or surgical masks), ASTM F3502 (barrier face coverings),[5] or regulations such as 42 CFR Part 84 (NIOSH N95 respirators)[6] provide testing guidelines and performance criteria. These tests characterize the filter materials' particle filtration efficiency and pressure drop under extreme conditions including high salt loading and high humidity. The PD and PFE requirements for level 1 and level 2 barrier face covering and N95 respirators is provided in table 1.1 For the fibrous filter material, high PFE is easily achievable but by compromising breathability. The key optimization for any filter system especially wearable filter apparatus is maintaining high PFE with low PD.

Although the current PPE is well developed and classified, they are mostly designed for short term /one time usage based on non-biodegradable material to provide passive protection. Here, we aim to develop the next generation of PPE with good comfort level of longer term usage based on a

biodegradable material that will reduce the contamination brought by single use PPE significantly. We also aim to develop smart PPEs that can sense the toxic contamination in surroundings and monitor physical conditions of wearer.

**Table 1.1** Summary of standards applicable to face coverings or face masks and respirators.

Standard	Mask type	Class (if applicable)	Testing air flow velocity	Particulate Filtration Efficiency (%)	Differential Pressure (Pa)
ASTM F3502	Barrier face covering	Level 1	10 cm/s	20%	147.1
	Barrier face covering	Level 2	10 cm/s	50%	49.03
NIOSH (42 CFR Part 84)	Respirator	Not applicable	85 l/min for a flat sample of 100 cm <sup>2</sup> ; 14.2 cm/s for respirator	>95% @ 0.075 +/- 0.2 μm count median diameter	343 Pa (inhalation); 245 Pa (exhalation)

## 1.2 Design of protective equipment

Various designs of protective equipment, such as surgical masks, N95 respirators, face masks, and gowns are currently available commercially. Notably, many protective equipment designs in the past have focused on short-term use in industrial environments. However, there is now more demand for protective equipment in a broader range of settings including medical use, public use and so on.

Moreover, because most of these commercial filter layers used for face masks consist of fibers with diameter in micrometers, they completely scatter and reflect light. With more than 50% of the face covered, communication and social interaction is more difficult for the wearer, as recognition of facial expressions and emotions is more limited. Some of the most affected individuals are children because of their innate need for human connection. Additionally, senior and deaf population with limited hearing rely on facial expressions to communicate. As a result,

they find it difficult to communicate using existing commercial protective equipment available [7]. Therefore, the demand for transparent protective equipment is also sought after by the vulnerable people in our society [8]. A suitable device in such a setting is a face shield that can minimize coverage of the entire face significantly compared with other equipment like face mask or respirator. However, the use of a face shield is effective in reducing the wearer's short-term exposure to larger infectious aerosol particles, while it provides poor protection for smaller particles that can remain in the air for longer periods of time [9].

Furthermore, protective equipment design has to consider a good fit of the equipment to the users face for effectiveness. Fitting to keep mask or respirator sealed to provide sufficient protection is critical but is often worn with leakages leading to poor real filtration efficiency. ANSI Z88.2-2010 is the standard to define fitting quality by numeric expression of how well a tight-fitting respirator fits a wearer during a quantitative fit test. The fitting factor is the ratio of the measured particle concentration outside the respirator ( $C_{out}$ ) to inside the respirator ( $C_{in}$ ). (Fit factor =  $C_{out}/C_{in}$ ). Evaluating both filtration efficiency and fitting factor can help users benefit from the protection offered by the wearable equipment with a decent sealing while usage. Finally, current commercial products like surgical masks, N95 respirators, face shields require sophisticated and capital-intensive equipment such as press lamination, heat bonding for their fabrication. In a pandemic, due to inordinately high demand, these constraints led to shortage of PPEs. A low cost, simple fabrication method for PPEs can also facilitate widespread manufacture of these essential equipment to fight the spread of diseases especially in resource poor settings.

### **1.3 Manufacturing of filter material**

Mechanism of air filtration is to absorb, attach and capture the air pollutants by filter media. The process and efficiency are mainly depending on filter properties and nature of pollutants. Fibrous micro- and nano-filtration materials can physically retain particles, even pollutants that are much smaller compared to the pore size [10]. There are four dominant mechanisms that result in particulate matter collection including gravitation, inertial impaction, Brownian diffusion and interception [11]. Apart from the mechanisms mentioned above, gas flow conditions, particle distribution, electrostatic interaction, filter geometry also influence the filtration efficiency to some extent. There are two typical ways to manufacture fibrous filter material with micro-size of fibers: melt-blown, spun-bond.

#### **1.3.1 Meltblown technology**

Meltblown (MB) technology was developed in the early 1950s as a simple, one-step fabrication process for nonwoven material[12]. The equipment for production of meltblown polymers was shown in Figure 1.1. First, the polymer in various forms is gravity-fed at certain rate from hopper to the extruder. The molten polymer is then flowed through a filter and supplied to a metering pump (gear pump) for uniform and consistent delivery to the die assembly [13]. This die assembly consists of a polymer feed distribution system to provide uniform polymer flow, controls the dwell time across the width of the MB die and has air manifolds to provide air streams with different temperatures reaching typically 50%–80% of sound speed [14]. The molten polymer is extruded through small holes into a converging stream of hot air and elongated into a fine fiber form by the drag force. Fibers are then transported to the collector by the air stream. The significantly lower air temperature contributes to fiber solidification. The attenuated filament stream forms a

nonwoven web on the collector with almost random network of fiber distribution and then feeds into the winder system for subsequent handling [12, 15, 16]. The fiber diameter typically fabricated by MB, ranges between 0.5 and 30  $\mu\text{m}$  with random fiber orientation [15, 17, 18]. In the past years, researchers have focused more on generating meltblown nanofibers normally by changing processing conditions [19], polymer modifications [20-22], and using special dies with smaller diameter of orifice and larger ratio between length to diameter [17, 23]. Diameter of meltblown fiber can reach less than 100 nm range varies from different polymers [14].

MB technology has multiple advantages like easy operation, low energy consumption, environmentally benign processing and others [24]. However, the melt-blown manufacturing line as well as customized dies are capital intensive, sophisticated, require skilled personnel and not suitable for smaller operation. Currently, commercial air filters and face masks are often developed as microfibrinous nonwovens from melt-blowing synthetic plastics such as polypropylene and generally of single-use. Melt-blowing nonwoven filter materials with biodegradability has only been recently feasible with synthetic polylactic acid (PLA) [25] yet, PLA degrades at very slow rates under natural conditions and requires highly acidic or alkaline conditions for fast degradation [26].

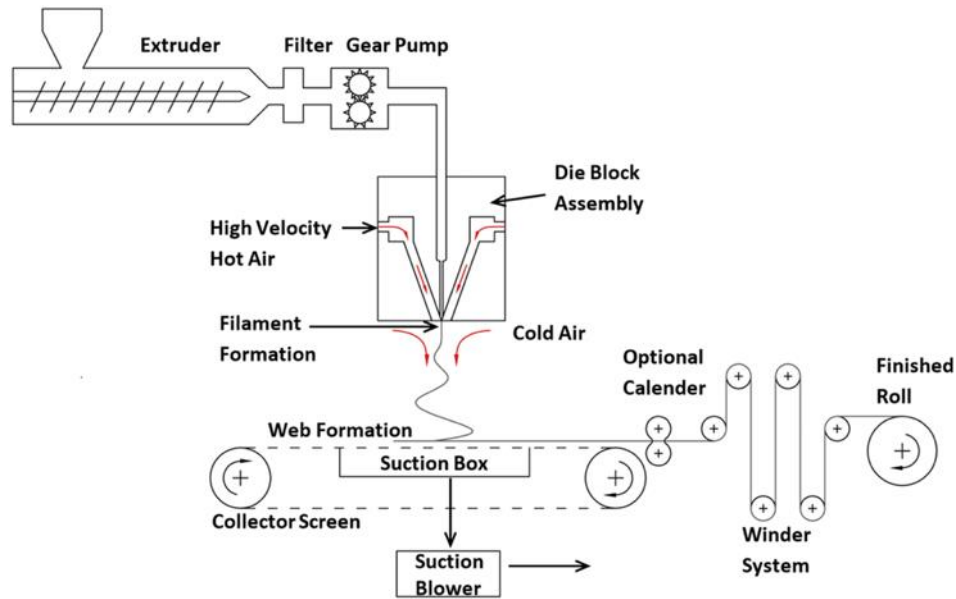


**Figure 1.1** Schematic diagram of the meltblown line [27].

### 1.3.2 Spunbond technology

Another method for generating non-woven materials is using spun-bond technology. Spun-bond nonwoven fabrication process consists mainly following steps: fiber releasing, quenching, drawing, bonding and winding as shown in Figure 1.2 [28]. Polymer resin is melted by heating and mechanical treatment and fed through the extruder long with other additives into filter followed by a gear pump. Operating temperature and pressure depend on the properties of resin material. The gear pump is used to precisely controlled volumetric flow rate of molten polymer connected with spin pack. The spin pack consists of a polymer feed distribution system (to control uniform temperature, polymer flow and residence time across the spin pack) and a spinneret made by metal block with thousands of drilled orifices on it. Several spinnerets placed side by side are used to fabricate wide web. The polymer emitted through the spinneret holes flows through the quenching chamber, where it cools and solidifies in air and then pass-through air gap inside attenuator. During the attenuation process, the fibers are stretched by the high-speed airflow, resulting in smaller

diameter fibers while moving from the spinneret to the collection belt. The vacuum under the belt helps form the filament web and then conveyed by the collection belt to bonding line where chemical bonding, thermal bonding or hydroentanglement and other bonding methods might be applied. After the bonding process, the fabric is subsequently wound and rolled [29-31]. Spun-bond fiber diameter normally ranges from 1 to 50 $\mu\text{m}$ , while the preferred range is 15–35 $\mu\text{m}$  [32]. Although spun-bond fabrication is well-developed, mature, and efficient, the equipment is large scale and expensive to purchase and maintain. It is also difficult to fabricate nanometer fiber and not feasible to utilize natural polymer similar with meltblowing process.

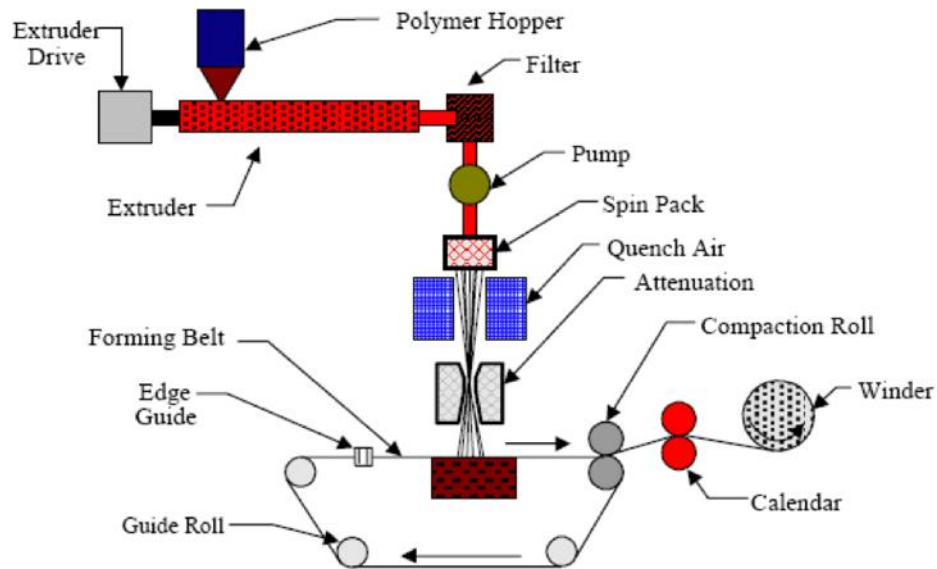


**Figure 1.2** Schematic diagram of the spun-bond process[28]

### 1.3.3 Electrospinning technology

Novel fabrication methods like electrospinning, draw spinning have been increasingly investigated for filter manufacture. The nano- and microfibers from electrospinning have high contact area and porosity and possess stable and superior properties from mechanical, chemical and even electrical

perspectives depending on the polymer used [33]. Electrospinning has been used and was important for numerous applications, such as filtration, biomedical, tissue engineering scaffold, environmental engineering, optical devices and so on during past few decades [34-38]. From previous studies, electrospinning showed the capability to produce nano- and microfiber ranging from 0.1 nm to micrometer level [39].

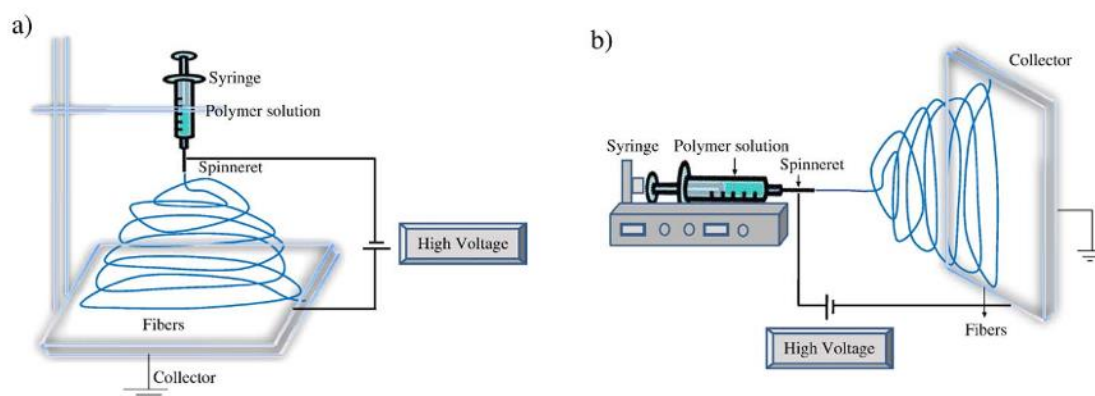


**Figure 1.3** Schematic diagram of electrospinning setup (a) vertical (b) horizontal [40].

There are two typical setups for electrospinning with orientation in the vertical and horizontal directions as in Figure 1.3. A high voltage is applied between the collector and a syringe with polymer inside to extract the nanofibers from the tip by the electric force. The electrospinning process generates an electric field by applying a high voltage between solution and collector to extract polymer solution to nanofiber. When there is an electrostatic field between a pendant droplet on the syringe tip-filled by the polymer solution and a metal collector as a counter electrode, it creates tangential stress resulting in the droplet's deformation to form a conical shape Taylor cone from polymer solution[40]. The emission of fiber from the tip of the cone is based on the strong mutual electrical repulsive force that overcomes surface tension in the polymer liquid which

is weaker force [41]. When the electric field strength overcomes the surface tension, the tip of the cone ejects a fluid jet from the syringe tip toward the metal collector.

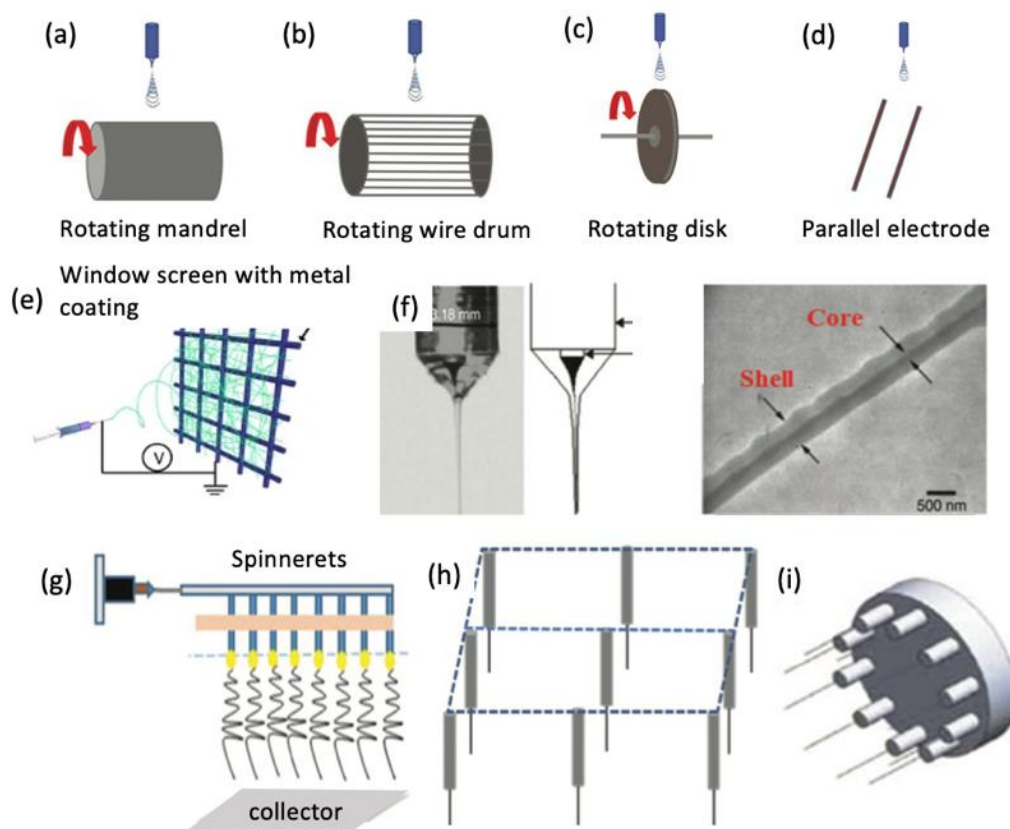


**Figure 1.4** Schematic diagrams of electrospinning collectors (a) rotating drum, (b) wire drum, (c) disk, (d) parallel electrode, (e) mesh electrode; (f) core-shell nozzle and transmission electron microscopy (TEM) image of the coaxial PANI/PVA fiber; multi-nozzle system of (g) linear, (h) square array, (i) concentric. [Adapted from [41-47]]

Different collector formats including flat, rotating drum [42], wire drum [43], disk [44], parallel electrode [45], mesh electrode [41] etc. have been used to collect the fibers and control the alignment in Figure 1.4. Also, there were various type of needle supply system used in electrospinning. Multi-nozzle/needle systems (Figure 1.4f-i) have evolved in the form of matrices

of nozzle in a line [46], square array[48], concentric array [49] to increase the throughput. Bicomponent coaxial nozzles could be used to supply inner and outer polymer solutions simultaneously to produce core-shell nanofibers [50, 51]. Several parameters could influence the electrospinning results, including ambient parameters, processing parameters, and solution parameters as illustrating in Figure 1.5 [40]. To build up a relative stable state for electrospinning, all those parameters needed to be considered and correlated. Appropriate solvent selection was critical for the electrospinning. The solvent needed to have properties like good volatility, vapour pressure, boiling point, and maintain the polymer solution's integrity. Solution viscosity and surface tension also varied for different solvent and plays an important role in the electrospinning process and results [52, 53].

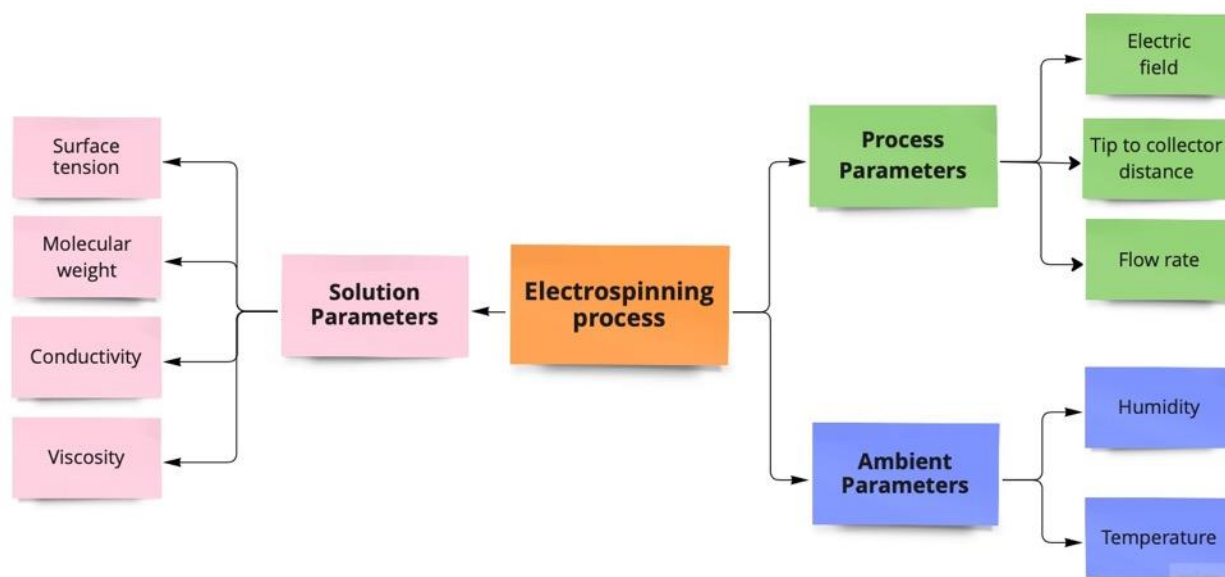


**Figure 1.5** Parameter map affecting electrospinning process

Solution-based processes like electrospinning offer a versatile processing platform to a wide range of natural or synthetic biopolymers [54, 55] compared with melt-blowing and spun-bond

technology. Furthermore, unlike melt-blowing and spun-bond which mainly produces microfibers, electrospinning has capability to control the size distribution of fiber from nanometer to micrometer range. Due to the size of some of the particulate matter such as viruses that are in the nanometer sizes, use of nanofiber can enhance the filtration efficiency of air filter. It also has been reported that the presence of nanofibers can effectively enhance the Brownian diffusion and interception filtration mechanisms of particulate filtration which are effective for particles of size 50-500nm [11, 56, 57].

## **1.4 Material of protective equipment filter**

### **1.4.1 Synthetic polymer based protective filter**

#### *1.4.1.1 Synthetic polymer for meltblowing*

Synthetic polymers like polypropylene, polylactic acid, nylon-6 and so on, were widely used in the manufacture of air filter material using both meltblown and spun-bond technology. Surgical masks made by polypropylene has been critical part of daily life during COVID-19. Presently, researchers were trying to improve the filtration performance by enhanced electrostatic force mechanism for meltblown nonwoven fabric. For example, electret perlite modified PP meltblown filter had PFE of 99.56% and PD of 290 Pa [58]. Barium titanate particles was added to produce PP electret meltblown fabric with 99.97% PFE and 95 Pa of PD at same time [59]. A multilayered PP air filter with additional step of corona charging has been evaluated by PM<sub>0.3</sub> salt particle [60]. This filter presented robust PFE of 99.03% and low PD of 82.32 Pa. In another study, magnesium stearate was used as a charge enhancer and added into PP to fabricate meltblown filter achieved PFE at 99.22% and PD at 92 Pa by multi-layer stacking and corona charging as shown in Figure 1.6a[61]. The morphology of PP/MgSt filter was relatively stable with around 2 $\mu$ m fiber diameter

and 14.2  $\mu\text{m}$  to 14.6  $\mu\text{m}$  of pore size in Figure 1.6c. By adding Magnesium stearate, the charging longevity has been enhanced to ensure the stability of filter performance. PP was also added with Polycarbonate (PC) resin as the meltblown resin with synthesis of Zeolitic imidazolate framework-8 (ZIF- 8) provided 91.68% of PFE and 46 Pa of PD aimed on  $\text{PM}_{2.5}$  (Figure 1.6b). By adding nanocrystals, the PFE has increased by 43.57% without compromising breathability[62]. The ZIF-8 nanocrystals increased the surface roughness and surface area. In this way, more small particles were captured and trapped along the airflow. Also, it polarized the surface of PM due to its positive charge. The same metal organic framework has been added in the resin blend of PP and Polyvinyl Alcohol (PVA) illustrated in Figure 1.6c[63]. This filter showed a PFE of 96.5% and PD as high as 131 Pa. However, most of meltblown nonwoven filters were based on PP which is non-biodegradable or composible. As the best of knowledge, PLA is the only biodegradable synthetic polymer can be used in meltblown process. PLA has excellent charging storage capacity to form electret via corona charging. Zhang et al. fabricated the meltblown PLA fabric as shown in Figure 1.6d has PFE of 88.5% and low PD of 27.2 Pa[25].

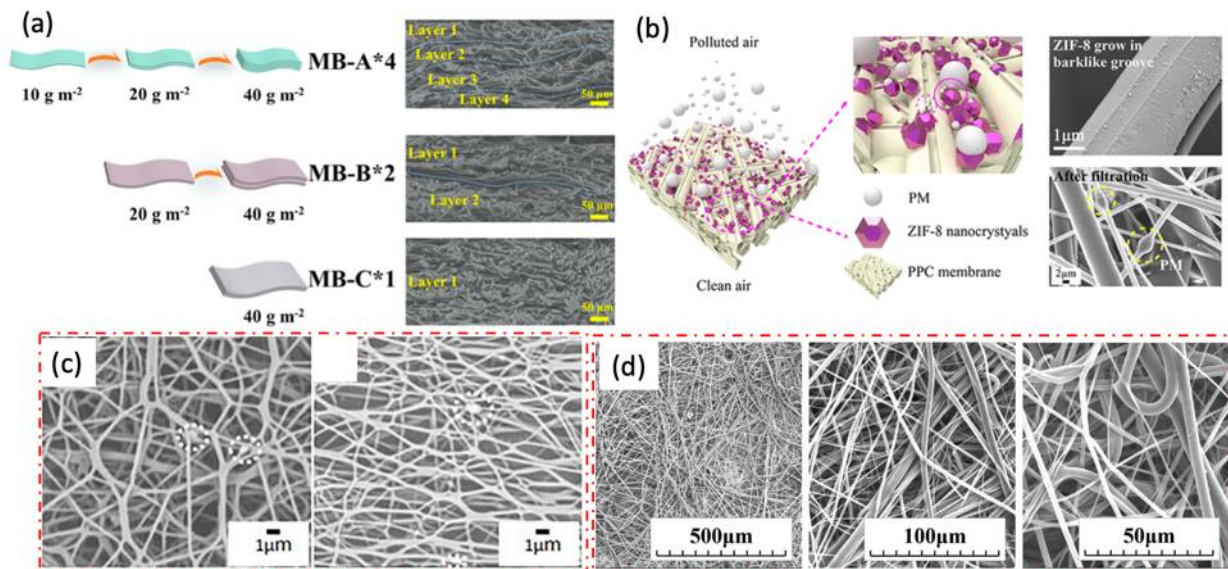


**Figure 1.6** Meltblown fiber with different synthetic polymers (a) Schematic and SEM of the multilayered PP air filter; (b) Schematic and SEM of PP/PC meltblown resin with synthesis of Zeolitic imidazolate framework-8 (ZIF- 8); (c) SEM images of the morphology of PP/MgSt filter; (d) SEM images of the morphology of PLA fiber(Adapted from [25, 61-63]).

#### *1.4.1.2 Synthetic polymer for Spunbonding*

Similar to meltblown filter, spun-bond technology worked for synthetic polymer mostly. Spun-bond fibers intended to be thicker than meltblown fibers in general and used as a sandwiched layer commercially as shown in Figure 1.7a. A PP and Polyethylene (PE) bicomponent spun-bond material with core-shell fibers has been evaluated to filter ultrafine particles (Figure 1.7b). The proposed filter provided  $97.02\% \pm 0.8\%$  of PFE and  $35.14 \pm 2.01$  Pa of PD in their study [64]. Yang. et al. reported a PP and PE bicomponent structure with MgSt particles to improve the stability of charge and also as a nucleating agent (Figure 1.7c-d). The modified filter has a PFE of 98.94% and PD of 37.92 Pa with long lasting performance in 90 days[65]. Another bicomponent spun-bond filter was investigated using Polyester (PET) and nylon-6 (PA6) with ratio of 7:3. PFE was 79.28% for the 0.37  $\mu\text{m}$  size particles and 97.68% for 2.05  $\mu\text{m}$  size particles, while the filtration resistance was nearly 140 Pa with hollow segment-pie bicomponent structure as shown in Figure 1.7f [66]. This segment-pie structure was also produced by the combination of PET, low crystallinity PET and PA6 as shown in Figure 1.7g. PFE of the lcPET/PA6 nonwoven was close to 99.9% for particles with a particle size  $>1.0$   $\mu\text{m}$  with PD around 94-96 Pa. the PET/PA6 filter provided over 99% PFE and 82-86  $\mu\text{m}$  PD with a particle size  $>4.0$   $\mu\text{m}$  [67]. Air filtration has also been investigated for PA6 and PE islands-in-the sea (INS) bicomponent spun-bond web with different fiber diameters (Figure 1.7h-l) [68]. In the INS structure, a polymer formed a matrix around fibrils as islands from cross-sectional view and the number of islands was controlled by

geometry of spinpack. This INS filter had PFE of 64.1% with 108 INS and PD of 27.0 mm H<sub>2</sub>O. PP spun-bond material coated by polytetrafluoroethylene (PTFE) and expanded graphite (EG) via electrospaying to increase the surface area and adjust the pore size has been fabricated in previous study (Figure 1.7e) [69]. Compared with original PP spun-bond material, researchers found the PFE is significantly increased from 52.18% to 85.00% with excellent antifouling capability.

The technique of both meltblown and spunbond non-woven filter materials is mature and well-developed. They provide large scale, automotive, and high throughput production of non-woven material which is widely used in PPE currently. However, both technologies suffer from limitations including difficult to apply natural polymers with biodegradability, high expense of equipment and expensive maintenance, as well as complexity of manufacturing process.

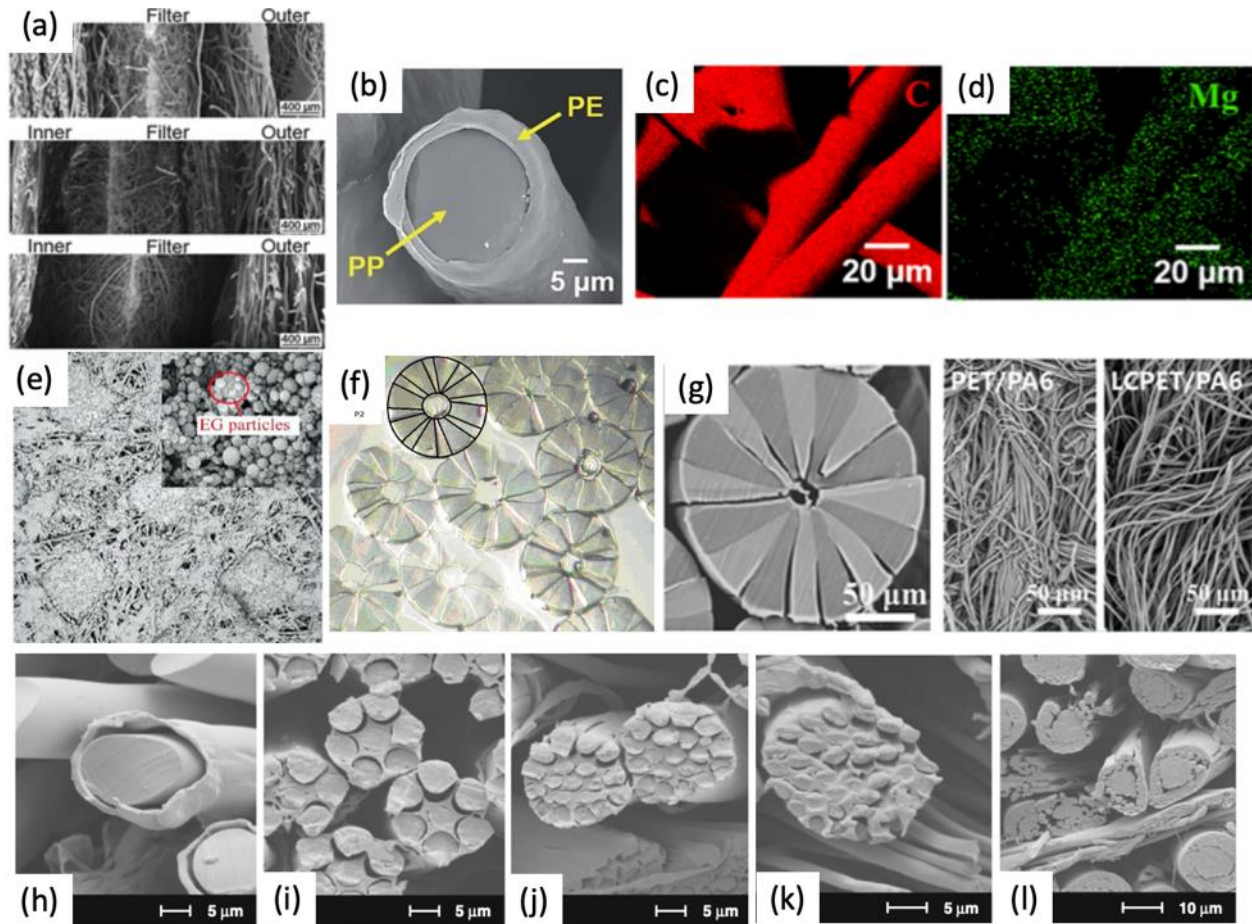


**Figure 1.7** (a) SEM of three-layer respirators with Spun-bond-Meltblown-Spun-bond combination, (b) the cross section of the PE/PP bicomponent fiber, (c)-(d) Energy-dispersive X-ray mapping images of C, Mg in Mgst-PE/PP, (e) SEM images of PTFE/EG1 on PP spun-bond fabric, (f) The cross section of PET-PA6 hollow segment-pie bicomponent fibers, (g) SEM images of the cross-sectional of lcPET/PA6 fiber and the surface of PET/PA6 and lcPET/PA6 fibers, (h)-(l) SEM images of INS webs with several number of islands in the sea: 1, 7, 19, 37, and 108. (Adapted from [64-70]).

#### ***1.4.1.3 Synthetic polymer for electrospinning***

Porous non-woven filter material have also been produced by electrospinning, and their filtration performance with fine particles investigated. For example, Polyacrylonitrile (PAN) electrospinning on the metal coating mesh filter had 95% PM<sub>2.5</sub> filtration efficiency with 90% transparency which was suitable for the indoor air protection through windows as a potential application [41]. Filter produced from PAN with bead-on-string electrospun fiber structure showed PFE with 99% of NaCl solid and Paraffin oil aerosols with average diameter of 0.3  $\mu\text{m}$ . Nanofiber of Nylon 6 has been generated by electrospinning with 80- 200 nm in diameter by various concentrations, and the PFE of nanofilters was 99.993% by 3 $\mu\text{m}$  test particles[71]. Polyimide (PI) nanofiber has also been shown to form excellent filters with 99.5% PFE of PM<sub>2.5</sub>, and high thermal stability (up to 370 °C) [72]. Electrospun polyurethane with N, N-dimethylformamide formed micrometer-sized fibers could remove the volatile organic compound from the air with rapid absorption [73]. Sub-micro size fibers of electrospun Polysulfone (PSF) had 99% removal of particles with a diameter higher than 7 $\mu\text{m}$  [74]. Besides, Polycaprolactone (PCL), polyethylene oxide (PEO), PVA, PLA etc. was also used to produce porous electrospun filter for air filtration application [75-77]. Electrospinning process is compatible with nearly one hundred synthetic polymers which is versatile compared with traditional technologies [47]. While the performance of air filters is of utmost importance to protect human health, the COVID-19 pandemic has also raised much attention to the disposal and environmental implications of air filter media and face masks which are usually single use devices [78]. This in turn has driven much attention to the development of recyclable and biodegradable or compostable air filters. Although, polypropylene (PP) can be collected and recycled, reverse supply chains for collecting used filters and facemasks

at community scale, separating the filter layers and reprocessing these into functional filters is a challenge.

#### **1.4.2 Natural polymers and its combination with synthetic polymer for protective filter**

Recently, natural polymers such as protein, collagen, silk etc. have been considered as alternatives to fossil fuel derived polymers to make the filter due to their environmental sustainability and biodegradability. Zein as a plant-based polymer is derived from corn and has been widely used in electrospinning air filters. Zein filter were fabricated on cellulose-based substrate with two different morphologies of nanofibers fabricated with different concentration of solvent using electrospinning (Figure 1.8a-d) [79]. Flat ribbon fiber filter had a higher PFE at 99% for  $PM_{0.3}$  and a PD at 109 Pa compared with the round fiber. The cellulose paper towel was also used as a substrate for gelation protein nanofibers from electrospinning. It had PFE up to 82.0% for particles smaller than  $1\mu m$  and 98.80-99.98% for particles larger than  $1\mu m$  and PD around 125-185 Pa[80]. Fan et al. fabricated a hierarchically structured air filter by pickering emulsion with zein and cellulose nanofibrils attached on wood pulp microfiber fabrics. This filter had PFE aimed on  $PM_{2.5-10}$  stayed in the same range of 95.54–98.96% and PD of 109.9-113.2 Pa [81]. Since most of natural nanofibers were relatively delicate and fragile with less robustness of mechanical property compared with synthetic polymers, researchers also combined natural and biodegradable synthetic polymers to fabricate air filters with less comprising biodegradability and sustainability. For the combination with biodegradable synthetic polymers, electrospun PVA with Cellulose Nanocrystals Composite nanofibrous filter achieved 99.1%  $PM_{2.5}$  removal rate with 91Pa pressure drop [82]. Cao et al. fabricated a silk-based fibroin combined with PEO filter by electrospinning technology, providing PFE of 99.99% for  $PM_{2.5}$  and PD of 75 Pa [83]. Chitosan

and poly(butylene succinate)-based micro- and nanofiber has been evaluated as air filter as shown in Figure 1.8e [84]. This filter was able to remove 98.3% of  $PM_{2.5}$  with a low PD at 59 Pa. Filter based on combination of zein and PVA produced by electrospinning had PFE over 97% of  $PM_{0.3}$  [85].

Although the natural filters have been widely investigated and developed, there are still some issues with their performance. Unlike synthetic polymers, natural fibers do not get charged easily and don't retain charge. Therefore, achieving high PFE requires smaller pore sizes and dependence on mechanical filtration which results in higher pressure drop and poorer breathability. Additionally, they are also hygroscopic to some degree and typically swell on exposure to humidity as well as become mechanically weak. By blending with biodegradable synthetic polymers, some of these issues can be tackled. However, those synthetic biopolymers degrade at extremely slow rates under natural conditions as compared with natural polymers [26]. Therefore, a suitable biopolymer-based filter fabricated using green solvents that can achieve high PFE and good breathability while being mechanically stable under humidity conditions is essential for promoting sustainable use of PPEs.

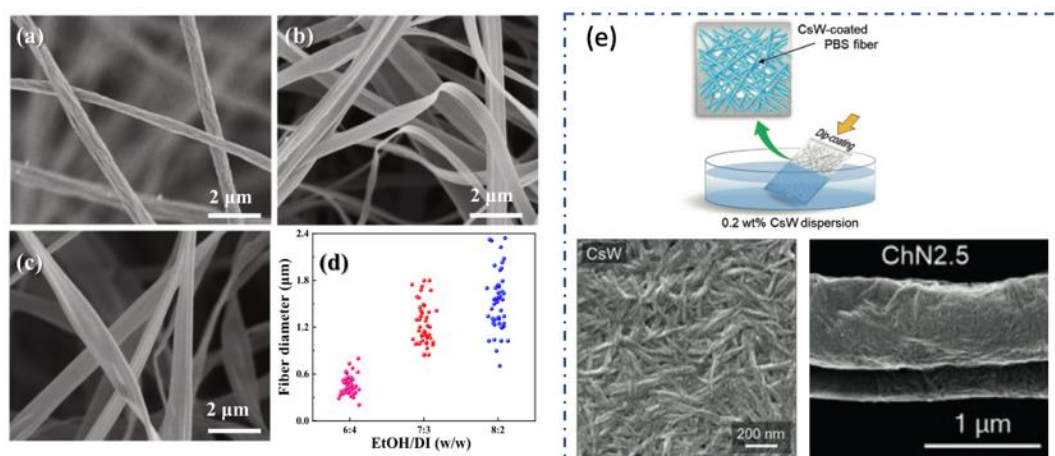


**Figure 1.8** (a)-(d)SEM images and fiber diameter distribution of Zein round and robbin like fibers with different concentration of solvent; (e) Schematic and SEM images of chitosan nanowhisiker with PBS fiber (Adapted from [79, 84]).

## **2. Wearable sensors integrated with protective equipment**

### **2.1 Importance of wearable sensors embedded in PPE**

Currently, wearable protective equipment such as PPEs are passive and provide protection from exposure to hazardous substances in the environment. However, they are not able to indicate the presence or absence of toxic contamination in the ambient environment. Development of such an active PPE that can not only monitor the environment, but also biophysical parameters of the wearer would be the next generation of this technology and would provide greater safety to the user. There are two kinds of monitoring are important for users of personnel protective equipment. These include monitoring their ambient environment for potentially toxic gases such as carbon monoxide, nitrogen oxide, ozone, sulfur dioxide or ammonia that may be present in an industrial setting or even particulate matter 2.5 or 10 that may be present in some cities. The other, is to monitor the user's health condition through biophysical or biochemical monitoring that can help identify critical issues that require medical attention.

In the first category, ammonia is a good example of the type of contaminant that requires active PPEs. Nowadays, human activities emit about 2.1-8.1 tons per year into the atmosphere of ammonia. Because ammonia is highly toxic and corrosive to the skin, eyes and lungs, inhalation of it above safe levels can cause significant morbidity and even mortality [86]. According to the Occupational Safety and Health Administration (OSHA), the limit of human exposure to  $\text{NH}_3$  is 25 ppm for 8 hours and 35 ppm for 10 minutes [87]. Additionally, Ammonia is frequently used

and is a common contaminant in industry like dairy plants, breweries, and juice processing factories petrochemical facilities and so on [88]. Therefore, one of the focuses of this thesis is development of suitable, wearable ammonia detection technology integrated into active PPE to enable preventions of lethal accidents caused by its overexposure. Similarly, personal physiological measurements can also be integrated into active PPEs. These are important for personnel working in extreme environments such as in a deep mine or underwater. Many physiological parameters such as glucose level, blood pressure, pH, electrolytes, dopamine and others can be monitored of which glucose is probably the one that is most critical. Therefore, another focus of this thesis is development of suitable fabrication technology that can enable the integrated of electrodes for sensing of biochemical parameters such as glucose.

## **2.2 Ammonia sensor**

A variety of sensing technologies are available for  $\text{NH}_3$  detection currently. The most common detection methods fall into three broad categories: conductometric solid-state sensing (metal oxide-based sensors, conducting polymer sensors), optical sensing (tunable laser absorption spectroscopy, nondispersive infrared sensors) and other modes of sensing (electrochemical sensors, surface acoustic wave sensors, colorimetric sensors etc.) [86]. In this part, we mainly focus on conductometric metal oxide-based sensor, optical sensor, and colorimetric sensor.

### **2.2.1 Conductometric Metal oxide-based sensor for ammonia**

The metal oxide was widely used as the solid-state sensing mechanism based on variation in electrical properties due to its simple fabrication and low cost. The electronic structure of the metal oxide was the important factor for specific gases detection. The gas sensing mainly involved two parts: receptor to recognize the target gas by electronic reaction on surface of metal oxides and

transducer to convert surface reaction into an electrical change. The receptor function depended on the chemical properties of surface oxygen in the metal oxide. The metal oxide nanocomposites were incorporated with noble metal nanoparticles such as Pd, Pt, Au with catalytic properties to improve and enhance the sensing performance[89]. Transducer function highly depended on the potential barriers at the grain boundaries to accomplish the conversion of electrical signal, which increased under oxygen atmospheric conditions because the electrons on tip of metal oxide surface were trapped by the charged atmospheric oxygen leads to decreasing of conductivity [90]. SnO<sub>2</sub>, ZnO, WO<sub>3</sub>, TiO<sub>2</sub>, and MoO<sub>3</sub> were the most popular metal oxides used in ammonia detection [91, 92]. As mentioned above, to enhance the performance, additive loading was widely used. Pd-doped ZnO-based ammonia sensor yielded enhanced sensing performance with a 5ppm detection limit and 3s and 9s for response and recovery time [93]. Su et al. reported further enhanced structures of ternary nanocomposites with Pd/SnO<sub>2</sub>/RGO (Reduced graphene oxide) via one-pot route consisting of noble metals, metal oxides and graphene[94]. This sensor had high sensitivity down to 5ppm of ammonia, relatively large testing range between 5 to 150 ppm and 7min of response time at room-temperature. The metal-oxide based sensor could also be enhanced by adding the metal oxide dopant into another base reported by Qi et al[95]. They utilized SnO<sub>2</sub> nanoparticle coated In<sub>2</sub>O<sub>3</sub> nanofiber structure as sensing material. The mixture of the two metal oxides produced a great synergy, with the SnO<sub>2</sub> nanoparticles on the In<sub>2</sub>O<sub>3</sub> nanofibers providing more reaction sites for the gas molecules. This combination significantly increased the response signal more than 5 times, shortened the response time from 16 to 7s and recovery time from 15 to 10s at 1ppm concentration. However, metal oxide sensing has some significant limitations, such as lack of selectivity during gas mixture detection [96]. Although metal oxide sensor has simplicity and low-cost fabrication process, its sensing response is not visual, and the signal always needs to be

converted while using, which makes it not feasible to be applied in many circumstances. Additionally, the liquid interference was not evaluated in these sensors since they were based on electronic elements. To achieve multiple time usage, additional heating treatment is necessary which is another limitation for daily usage.

### **2.2.2 Optical and colorimetric sensor for ammonia**

Among the gas sensors using optical absorption, tunable laser absorption spectroscopy (TLAS) has been well developed for  $\text{NH}_3$  gas detection. Ammonia gas is capable of absorbing light at the infrared spectral region as the molecules of gas are excited by laser oscillations at those wavelengths. Usually, for the detection of ammonia gas, wavelengths in the spectral range of 1450 to 1560 nm are chosen. The schematic of TLAS for ammonia sensing has been shown in Figure 1.9. The incident light from the tuned light from the semiconductor laser emitter is split and passes through the ammonia gas and reference cell simultaneously and reaches each photodetector. Emitted light is converted into an electrical signal by a photodetector and used to calculate the analyte concentration. Guo et al. developed a portable ammonia sensor based on TLAS with 0.16 ppm of detection limit and a response time of 184 s [97]. Although the TLAS is one of the best choices commercially for gas analysis due to its high selectivity and accuracy, the sensitivity is limited to the absorption coefficient and TLAS requires very high threshold currents and low temperatures to confine the carriers to the junction region. More importantly, the large size and high cost of the devices makes it not suitable to use for wearable sensors.

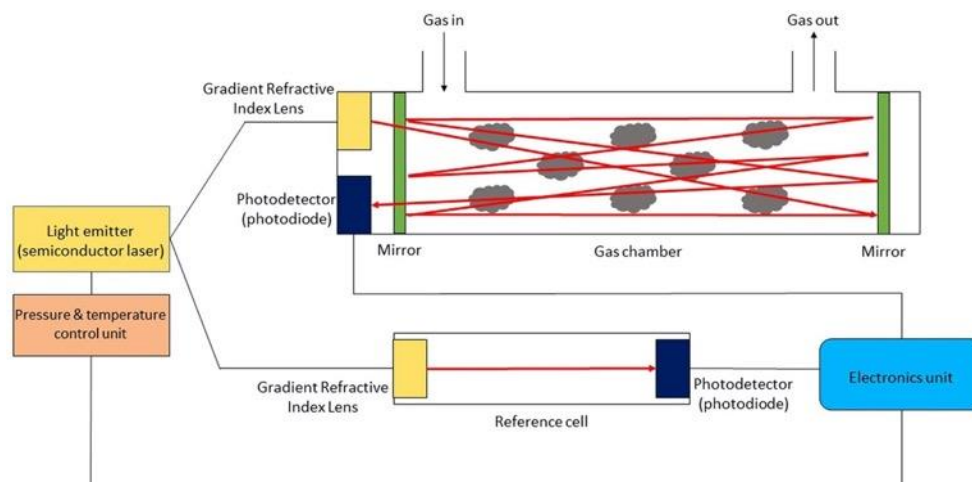


**Figure 1.9** Schematic of TLAS for gas detection (Reproduced from [86])

Colorimetric sensing mechanism is also widely employed in ammonia sensors. Colorimetric sensors provide optical measurements from the interaction of mostly porous substrate with the target gas. These sensors are based on the color change produced by chemical reaction which is incorporated in the sensing substrate. In previous study, a sensitive and reversible colorimetric sensor was reported with sodium hydroxide modified ultrathin PANI film on a commercial cellulose filter paper [98]. The PANI film was decomposed and converted from an emerald salt (green) form to an emerald base (blue) form after its reaction with ammonia. This sensor had a detection limit of 10 ppm detection limit of vapour ammonia up to 50 ppm detected by naked eyes, reaction time less than 30 s and showed reversibility for over 50 cycles. However, the selectivity of proposed sensor was not tested. Kim et al. fabricated colorimetric dye-loaded nanofiber yarn with lead(II) iodide ( $\text{PbI}_2$ ) for ammonia detection as well as other gases (Figure 1.10a-b) [99]. The yarn shaded from bright yellow color to lighter yellow nearly white color with 1 ppm detection limit for ammonia within 20 s of response time and 1-100 ppm detection range. However, the

thread fabrication using heavy metal-based dye has potential hazard while usage especially for protective equipment like masks due to accidental release and related toxicity issues.

Various pH indicators were widely used to fabricate colorimetric sensors for ammonia. The reversible reaction of pH indicators can be triggered by alkaline gas ammonia as shown in Figure 1.10c for bromophenol blue (BPB) dye. The color change depends on the deprotonation and protonation of pH indicators. The colour change occurs at pH 3.0 (yellow)-4.6 (blue), 3.8 (yellow)-5.4 (blue), 5.2 (yellowish green)-6.8 (purple), 6.0 (yellow)-7.6 (green), 7.0 (yellow)-8.8 (red) and 8.0 (yellow)-9.2 (blue) for solutions of BPB, bromocresol green (BCG), bromocresol purple (BCP), bromothymol blue (BTB), cresol red (CR) and thymol blue (TB), respectively[100]. Colorimetric films combined with optical waveguides has been developed as well[101]. The pH indicators including BPB, BCG and BCP have been added into poly(vinyl butyral) (PVB), ethyl cellulose (EC) and poly(methyl methacrylate) (PMMA) to fabricate a colorimetric film. Gas measurement was based on the optical readout and transducer after color change with limitation as low as 0.25 ppm, detection range up to 10 ppm, response time less than 1 hour and decent selectivity among other gaseous species ( $C_2H_5OH$ ,  $C_2H_4$ ,  $H_2$ ,  $CO_2$ ,  $CO$ ,  $NO_2$ ). Even though this sensor has high sensitivity, the setup requires a readout electronics and multiple other parts which limits the incorporation with wearable equipment and their response time was longer than desired. Colorimetric sensing threads based on 5,10,15,20-Tetraphenyl-21H,23H-porphine manganese (III) chloride (MnTPP), methyl red (MR), and BTB covered by Polydimethylsiloxane (PDMS) provided the detection limit of 50-1000 ppm as shown in Figure 1.10d [102]. The response time varied based on the thickness of PDMS coating from 70.2-101.5 s. This eye detectable thread can be used in woven garment easily, but still is difficult to combined with wearable filter equipment like masks that use non-woven material without introducing extra leakage from stitching.

Additionally, the relatively long reaction time due to the large thickness of thread and PDMS coating is another limitation.

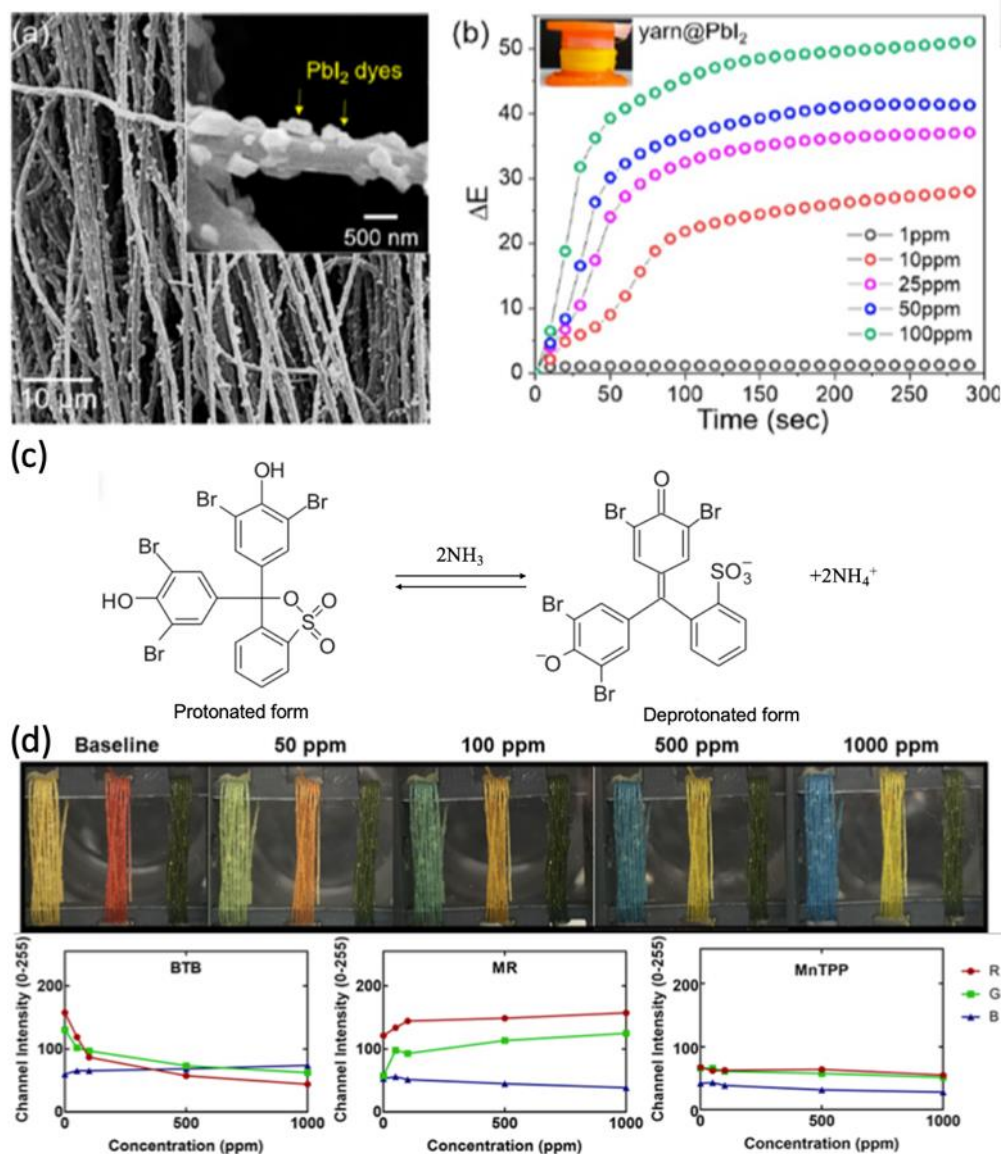


**Figure 1.10** (a) SEM images of yarn PbI<sub>2</sub>; (b) In situ time-dependent  $\Delta E$  values depend on NH<sub>3</sub> concentration (1, 10, 25, 50, and 100 ppm) using yarn PbI<sub>2</sub>; (c) Reaction mechanism of the pH indicator BPB for the detection of NH<sub>3</sub>; (d) Optical images of BTB, MR, and MnTPP devices

and the corresponding RGB color information extracted from the optical images for different concentrations of ammonia (Adapted from [99, 102]).

Electrospun nanofibers have attracted a great interest as a support medium for gas sensors as a way to enhance the sensing performance (response time, sensitivity etc.) by increasing the contacting area between sensing material and target gas. Micro or nanofibrous membranes greatly increase the surface-to-volume ratio and allow uniform immobilization of the dye. Electrospinning has also been used as a method to produce nano and microfibrinous substrate with ammonia sensing colorimetric dyes. Hoang et al. fabricated the polyacrylonitrile mats by electrospinning with bromocresol green to detect ammonia with excellent selectivity among common volatile organic solvents, with less than 1 minute response time, 1ppm detection limit and detection range from 1-100ppm[103]. Although the sensor performance was good, pH dye based colorimetric sensor in this work can also generate false positives due to interferents such as basic liquids, vapors or aerosols in the environment. Most of the ammonia sensors that have been developed use pH sensors and were developed for gas sensing in ambient environment where the pH does not change. Therefore, selectivity towards pH changes were not considered. There were also not designed for PPEs where the air that flows through the sensor is actually breathed in by the user wherein material toxicity is a far more important consideration. The pH of human exhaled breathe condensate was 7.83 that might lead to the color change for the pH dye-based sensors imbedded in PPE. Therefore, it is necessary to have a liquid resistant coating with air permeability on such sensors[104].

### **2.3 Wearable glucose monitor sensor**

Glucose is the primary source of energy for cellular activity in living organisms. Maintaining proper glucose concentrations in the blood is critical, and the homeostatic system in human physiology strictly regulates glucose levels [105]. Glucose monitoring technology has been used in the management of diabetes for decades. Blood glucose level is a key indicator of health condition, especially with the symptoms associated with diabetes. Diabetes is one of the most widely spread modern lifestyle diseases, affecting hundreds of millions of people, and ranking as one of the leading causes of death worldwide [106]. During past decades, there has been tremendous progress made toward development of glucose sensors. Although the first generation of glucose sensor started from enzymatic methods with either glucose dehydrogenase (GDH) or glucose oxidase (GOx), several limitations exist due to their dependence of enzyme activity on temperature, humidity, interference, etc. These limitations have led researchers to explore enzyme-free detection, where glucose can be oxidized directly on the electrode surface. Most of the current commercially available methods extract blood or are implanted in the body for continuous monitoring as shown in Figure 1.11. However, these invasive methods are painful and can lead to infections and other complications if not used properly which has led to research and development of several non-invasive methods where glucose present in other body fluids such as tears, saliva, interstitial fluid (ISF), sweat and breath can be analysed [107]. The noninvasive detection is based on the reliable relationship between glucose level of these other biological fluids and blood. The concentration range of glucose in different type of biological fluids is shown in Table 1.2 which is critical to define the detection limit of different sensors [107-110]. The relatively low concentration in biofluids compared with blood raise the concern of reliability and accuracy. There

are extensively work aiming on noninvasive glucose sensing development to enhance the performance from various perspectives.

In the context of protective equipment, monitoring of physiological parameters in a worker is of importance in industries such as mining, mineral and oil exploration under the sea, where the workers can be under physiological stresses that can aggravate underlying health conditions and accessibility to immediate medical care may not be feasible. Glucose monitoring is of use in conditions where the worker can be diabetic and requires periodic monitoring to determine its levels so that blood sugar levels can be maintained using medication doses or food.

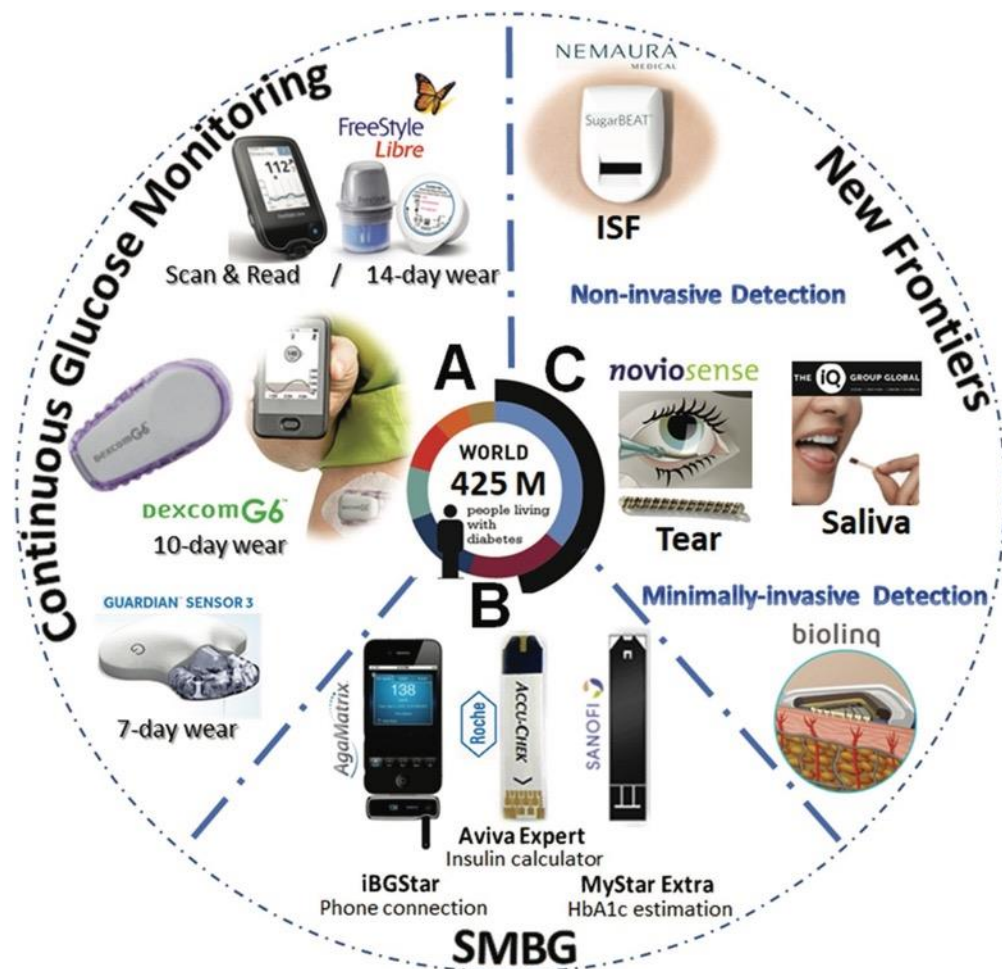


**Figure 1.11** Evolution of glucose sensors from (a) continuous glucose monitor, (b) self-monitoring glucose device; (c) noninvasive or minimally-invasive detection [111]

**Table 1.2** Glucose concentration range of different fluid types

Fluid type	Glucose concentration
Blood	2–40mM
ISF	1.99–22.2mM
Saliva	0.008–1.77mM
Sweat	0.01–1.11mM
Tear	0.05–5mM
Breath	0.16–3.6mM

### 2.3.1 Wearable tear glucose sensor

Electrochemical and field effect transistor sensor has major developments for blood glucose sensing in the past decades. Human tear, excreted by the lachrymal gland is an emerging body fluid that can be used for healthcare monitoring applications. Due to the challenge during tear collection, these sensors were integrated into contact lenses and glasses in previous studies. Yao et al. demonstrated a contact lens glucose sensor based amperometric with PET polymer and metal deposition, following by lift-off in acetone. The electrodes with PET polymer were shaped in a contact lens form and coated with glucose oxidase and titania sol-gel membrane, and then covered with nafion. The sensitivity of this sensor was  $240 \mu\text{A cm}^{-2} \text{mM}^{-1}$  [112]. Kim et al. developed transparent graphene and as Field-effect transistor tear glucose sensor and antenna to minimize the visual disturbance. The graphene-silver nanowire hybrid structure had excellent electrical and mechanical properties with immobilized GOx to enhance selectivity and sensitivity. This device had capability to detect glucose concentration of as low as  $1\mu\text{M}$  [113]. Besides of contact lens platform, Wang et al. demonstrated an eyeglasses-based tear biosensing device to monitor glucose and other biomarkers [114]. The fluidic channel was placed onto the nose bridge pad of glasses to collect tear and detection mechanism was based on electrodes with GOx enzyme with screen

printed electrodes. Despite significant works have been demonstrated by researchers, there are still concerns about the tear glucose sensors. One concern is eye irritation which is common and compromise the correlation between glucose level in blood and tear [115]. The other could be the availability of tear in a consistent and periodic basis. Additionally, tear glucose sensor is not suitable for implement in PPE since all the equipment will not offer direct contact with eyes to collect tear. This prevents tears from being a source of glucose sensors embedded in PPE.

### **2.3.2 Wearable saliva glucose sensor**

The well-developed electrochemical enzyme-based glucose sensor was also being used for glucose sensing in saliva. Saliva is an attractive biological fluid produced by the salivary glands and more easily to access compared with tear. Correlation between blood glucose levels and salivary glucose confirms the clinical relevance of saliva in blood glucose monitoring[116]. To prevent interference from food or other components in oral cavity, large biomolecules mixed in saliva were filtered out by the Polyvinylidene fluoride (PVDF) membrane conventionally, allowing external testing of glucose in saliva with testing range from 0.017–1.11 mM and sensitivity of  $26.6 \mu\text{A cm}^{-2} \text{mM}^{-1}$  [117]. A new mouthguard-type of glucose sensor was demonstrated to monitor glucose level directly in oral cavity with a wireless transmitter [118]. The sensor utilized Pt and Ag/AgCl as electrode based on the GOx enzymatic mechanism. The enzyme was immobilized on the Pt working electrode and mounted on the polyethylene terephthalate glycol surface of the mouthguard copolymer The glucose sensor was capable of highly sensitive detection in the glucose range of 5-1000  $\mu\text{M}$  within 60 s in artificial saliva with exponential response. There were many studies related to improve the sensitivity and stability of saliva glucose sensing [111, 119]. However, it is still quite challenge to measure glucose by saliva. Some of the studies were carried

by artificial saliva and the accuracy of glucose measurement can be interfered with by various impurities in saliva from ingested food or drink and digested metabolites especially for directly detection in real oral cavity. Saliva sensing is also ‘invasive’ considering an in-mouth extraction is needed. Additionally, the materials and components need to be fully biocompatible to prevent potential long-term effect. The antifouling property also needs to be considered for in-situ sensors after usage in mouth. All those limitations make saliva glucose sensing is not feasible to be combined with PPE.

### **2.3.3 Wearable ISF glucose sensor**

Cutaneous ISF surrounds the cells and provides nutrition via diffusion through the capillary endothelium, which results in a reliable correlation between blood and ISF glucose levels [120]. Reverse iontophoresis (RI) is the most recognized method for extracting ISF to the skin surface by applying an electric field without piercing the skin or contacting the blood. Due to the negative charge of human’s skin, the positively charged sodium ion flux forms a predominant ionic flow towards the cathode which also results in the glucose movement towards the same electrode [121]. A commercial product based on this mechanism, namely GlucoWatch, was already available in the market [122]. But it was associated with multiple problems such as skin irritation after long time usage, 2-3 hours long warm up time and so on. Wang et al. designed a tattoo-type RI glucose sensor with amperometric glucose detection [123]. A screen-printed tattoo consisted of Ag/AgCl electrode and Prussian blue (PB) working electrode with immobilized GOx enzyme on the flexible tattoo paper platform. The sensor had sensitivity of 23 nA/  $\mu$ M with 3  $\mu$ M LOD for glucose sensing. By validating simultaneous glucose measurements using a commercial blood glucose meter, the performance of the tattoo-based electrodes was assessed by comparing glucose signals recorded

before and after meals. Further investigation on calibration and long-term performance still needed to be studied. Chen et al. demonstrated a clinical level patch-based glucose sensor on a gold electrode-based paper battery [124]. Positively charged hyaluronic acid was used to enhance ISF collection by breaking the balance between ISF filtration and reabsorption. This multilayered biosensor consisted of polymethyl methacrylate, spin-coated polyimide, nanostructured deposited thin gold film, electrochemically deposited PB transducer layer, and the enzymatic GOx immobilization layer. The results showed an improved correlation between blood and ISF glucose level by clinical trials on patients with high sensitivity ( $130.4 \mu\text{A}/\text{mM}$ ). Even though glucose level in ISF has better correlation with blood, there are still challenges. The inconsistent amount and extraction rate of ISF leads to effect on consistency and stability of glucose measurement. Also, the extraction of ISF still causes pain to some extent. This invasive/in-vivo way of obtaining samples keeps them from being used for sensors integrated with PPE.

#### **2.3.4 Wearable breath glucose sensor**

Combining the well-developed glucose sensor with exhaled breath condensate is another non-invasive way to monitor glucose level in body. The breath-blood glucose ratio was determined to be 0.08 in healthy human and 0.09 in patients with diabetes[125]. Chu et al. developed immobilized aluminum gallium nitride (AlGaN)/GaN high electron mobility transistors (HEMTs) to sense glucose in exhaled breath condensate. The proposed sensor could detect glucose ranging from  $0.5\text{nM}$  to  $125\mu\text{M}$  which was suitable for the average glucose level in exhaled breath condensate[126]. Tankasala et al. designed a temperature-based selective collection and condensation of exhaled breath for glucose detection[127]. The exhaled gas was collected and condensed by setting a threshold temperature for the purpose of collecting exhaled breath

condensates with higher concentrations of glucose. The glucose level in most of collected condensates was between 13.6  $\mu\text{M}$  which was more concentrate than normal breath. However, the calibration curve and standard baseline still needed further development. Compared with other noninvasive methods, breath condensate is still under development. There are multiple challenges of this method. First, due to the low concentration of glucose in the exhaled gas, condensate sensing requires large volume of sample which makes sample storage and collection more difficult. Also, fluctuations in pH during respiration can easily lead to inaccuracy of enzyme-based glucose sensors. However, breath detection is the most direct way to incorporate with PPE based on its working principle. By combining highly sensitive, non-enzyme based glucose sensor with PPE such as face mask, face shield, offers the potential opportunity for development of next generation PPE with function of health condition monitoring.

### **2.3.5 Wearable sweat glucose sensor**

Sweat is important for non-invasive sensing because it is widely distributed throughout the body compared to other biological fluids, and it is responsive enough to reflect the physiological state of the core body in a timely manner. The rapid diffusion of small molecules (e.g. glucose) in sweat makes it very feasible to collect fresh sweat samples at short intervals, which can be readily monitored once combined with a glucose sensing device. A correlation of the glucose level between blood and sweat has been reported that 0.3 mM glucose in sweat corresponds to 300 mg  $\text{dL}^{-1}$  glucose in blood [128]. Kim et al. designed a stretchable sweat sensor patch by graphene doped with gold and combined with an Au mesh for electrochemical glucose[129]. This sensor used GOx functionalized PB electrode with serpentine gold mesh and Au-graphene as the sensing element on a soft silicone membrane. The excellent electrical property of Au-graphene based on

its large electrochemically active surface prompted the sensing performance of patch. Glucose detection limit of this patch was 10  $\mu\text{M}$  with 0.01-0.7 mM sensing range. Further development was a sensing system with upgraded sweat uptake design by waterproof layers [130]. The design enabled small volume of sample down to 1  $\mu\text{L}$ . Simultaneous analysis of pH, humidity and temperature was achievable to better understand the correction of sweat glucose measurement. However, the stability, repeatability and reproducibility remain challenging. A new epidermal microfluidic biosensor has been reported by Martin et al. [131]. The PDMS microfluidic channel fabricated with photolithography enabled rapid filling of the detection reservoir. GOx immobilized PB electrode was used as sensing area with a 50  $\mu\text{M}$  detection limit. The glucose level in sweat was relatively low with dilution, it required relatively high sensitivity of sensors. In addition, the form of the band or patch needed to be tightly integrated between the skin and the sensing area and also had potential risk of contamination, which was also challenging. Forehead is one of the places with extensive accumulation of sweat over human body. The sweat sensor eases the difficulty level to collect biofluid compared with other fluids, and it is most suitable to be combined with wearable protection equipment. The face shield is one of the commonly used PPE and inevitably comes in contact with the forehead when fixing the face shield. This is an excellent source for collecting sweat. Incorporating a glucose sensor in the face shield is a potential possibility for developing the next generation of PPE. Currently, most of the biofluid-based glucose sensors are on a single platform and an integrated system has not been developed by combining them with other protective equipment such as face shield and masks. In this way, protection can be provided while continuous monitoring, which is one of the objectives of this thesis.

### **2.3.6 Laser induced graphene based glucose sensor**

The three-dimensional graphene framework fabricated from laser scribing method was first proposed by Tour et.al showed the porous structure with large surface area, high electrical conductivity, excellent chemical and thermal stability [132]. Metal nanoparticle modified graphene nanomaterial has great performance for glucose sensing and is on recent research focus. It exhibits excellent electrocatalytic properties relying on the modified metal. Tour's group also developed a solution based synthetic thin film by high temperature and pressure treatment and vacuum drying, followed by laser scribing to form porous LIG [133]. Other nanoparticles including AuNPs, PtNPs, and AgNPs has also been fabricated on the LIG surface to functionalize the graphene [134]. The Au modified LIG in previous study by the electrodeposition method has shown the sensitivity of  $0.024 \pm 0.001$  mA/mM to glucose as skin wearable sensor [135].  $\text{Co}_3\text{O}_4$  NPs were also fabricated by high temperature treatment and vacuum drying on LIG [136]. The fabricated sensor showed glucose sensitivity of  $0.214$  mA  $\text{mM}^{-1} \text{cm}^{-2}$ . However, the proposed method before required large-scale instrument, conditioning limitation to fabricate, also relatively expensive and involved in chemical reagent which will lead to liquid waste contamination. The bonding between nanoparticles and substrate graphene might also experience falling off effect after long time usage.

### **3. Summary**

Based on the different working and living circumstances, there are different harmful compounds released into the surrounding environment. Air quality is an important factor effecting human health, both in daily life and in industrial environments. It is essential to have a well-designed system that can provide both protection and monitoring. As to protection provided by wearable device, different user groups and situations should be considered in the design of protection

equipment, including children, the elderly and people with disabilities. the use of disposable protective gear has created tons of waste pollution that is either not recyclable or difficult to recycle since the beginning of the covid pandemic. This has led to increased interest in the development of recyclable and biodegradable or compostable air filters. In addition to design, the investigation of recyclable and biodegradable protective materials with decent filtration performance is critical. The traditional technology like spun-bond and melt-blown is highly commercialized and used as fabrication process over decades. However, both are hard to be combined with natural polymers which is important for sustainable manufacturing. This in turn has raised interest in newer nano- and microfiber fabrication methods, particularly electrospinning using natural polymers. Therefore, using ‘clean’ solvent and natural material during fabrication process with high filtration efficiency and good breathability benefits from both human being and environment. Most natural polymer-based filters are relatively vulnerable compared to synthetic polymer-based and are sensitive to humid environment. Such a filter with robust moisture and mechanical properties is yet to be developed. The integration of sensors will further into PPEs can enable the development of next generation of wearable equipment that is active and responsive in protecting the health of the wearer. The sensors integrated into PPEs are needed both to monitor the environment of wearer but also in some situations to monitor the physiological parameters of the wearer. Glucose levels are one such model physiological parameter of importance. Diabetes is the most widely spread and one of the leading causes of death worldwide, a modern lifestyle disease that affects hundreds of millions of people. Blood glucose levels are a key indicator of health status. Measurement of glucose levels by blood sampling can be irritating due to needle piercing and potentially infectious. Therefore, here we focus on integrating the glucose sensor into the wearable devices via sweat sensing based on correlation between blood glucose levels and sweat glucose as a technology

demonstrator for physiological monitoring. Harmful gases in the environment are important to monitor and ammonia is a model for noxious gases found in industrial and agricultural settings. Colorimetric sensing mechanism is the most feasible and straightforward in daily usage. Even though ammonia sensor is well developed, combination between wearable device and ammonia sensor which provide naked eye- based alerting still needs to be further developed. In addition, disturbances in the working environment, such as exposure to high pH liquids, can have a significant effect on pH-based dye colorimetric methods should also be avoided.

#### **4. Objectives of the thesis**

The objective of this thesis is the development of technologies for next generation of personal protective equipment that is well designed, sustainable and active in monitoring of environmental and physiological parameters with capability to provide basic protection and physiological monitor like glucose during the daily usage. One of the focus has been development of well-designed PPEs that provide protection against aerosols and particulate matter while still allowing visualization of the face and mouth of the wearer which is important for a segment of the population. The next focus was on developing sustainable non-wovens for filtration applications, especially face masks. The other two focuses are the development of colorimetric sensing platform for integration with non-woven materials that is capable of instantaneous, power free sensing of environmental gas contaminants such as ammonia as well as an electrochemical sensing platform for physiological parameters with glucose as a model analyte.

#### **5. Thesis organization**

The thesis is organized in the sandwich format and a consists of 5 main chapters part from this one. The next four chapters details the contribution towards various aims and focus areas of this thesis

and description of these chapters are provided below. The thesis ends with a chapter conclusions and future potential

#### Chapter 2:

Chapter 2 focuses on optimal design and fabrication of new personnel protective equipment for air filtration based on development of a one-piece full head covered face. This chapter describes the development of a one-piece full head covered face shield for greater personal protection. It describes the fabrication details of the novel design, comfort level while long time usage, and evaluation of other parameters including temperature, humidity, carbon dioxide level and filtration efficiency. This study showed that the proposed novel design would be suitable for different circumstances with sufficient protection.

#### Chapter 3:

Chapter 3 is on optimal material and manufacturing of wearable protective equipment filter with biodegradability and improved filtration performance. This chapter details the development of bio-polymer filter with a pleated design that contains hierarchical structure to improve comprehensive performance with high filtration efficiency and low pressure drop to small aerosol particles. The stability test also be illustrated including high humidity and mechanical handling which shows the robustness of proposed crosslinked zein air filter. The long-term performance is also verified by conducting extended loading test for both composite zein filter and commercialized filter material.

#### Chapter 4:

Chapter 4 focuses on the development of a colorimetric platform technology for next generation of PPE to identify gaseous contaminants in the environment. This chapter describes the development of a low-cost electrospun reusable colorimetric sensor for ammonia detection. It

states the advantages of single-nozzle electrospinning method to fabricate bi-polymer based gas sensor. Sensing performances including sensitivity, detection range, reaction time and tolerance to both gaseous and liquid interferences are described and evaluated.

Chapter 5:

Chapter 5 focuses on the development an electrochemical sensing platform for physioalological monitoring in PPE. This chapter describes the development of glucose sensor (as a model) based on low-cost superhydrophobic 3D laser induced graphene from Polycarbonate. The fabrication method is stated in detail with optimization of parameters. The mechanism of graphene formation and glucose sensing is also explained. Other applications based on the developed materials are simply described. It also shows great potential for combination with face shield to enhance the function of next generation of PPE.

Chapter 6:

This chapter states the conclusions of thesis and future potential works for next generation of PPE from the combination of design and material, functional sensor implements and potential of function fulfillment perspectives.

## **6. Research contributions**

The primary objective of this thesis is the development of new materials and manufacturing methods for next generation PPE. The protective equipment developed is designed to achieve long-time usage without blocking facial features, and potentially be biodegradable and sustainable for the filter material. This would benefit the environment compared with current products. The developed protective equipment also has the capability for toxic gas-ammonia detection to provide

active protection along with health monitoring function for glucose levels in the body. The contributions made in this thesis can be divided based on each project.

Chapter 2: The applied contributions that resulted from this chapter are the development of a novel full-head, one-piece design of face shield. The proposed design provides splash protection and particulate filtration comparable to traditional face shield and mask combination, while providing a clear view of the wearing individual's face. The full-face respirator does not require the use of special industrial equipment or expertise for its fabrication, which is attractive to some developing countries in meeting their PPE requirements in emergency situations.

Chapter 3: We have developed a pleated design that contains hierarchical structure to improve comprehensive performance with high filtration efficiency and low pressure drop. These pleated hierarchical structures provide a solution to the commonly poor breathability of electrospinning filter material. The extended long-term loading test also helps understand the pattern of particle accumulations on the proposed pleated structure. Also, the pleated filter material design is proved to be a universal approach for other filter materials to significantly improve the breathability of filters. This method provides the solution without complicate modification of fabrication, by simply adding one step of adding folded structure. This method can also be used as the filter material in the novel design of face shield as a next step.

Chapter 4: Here, to fabricate the liquid-tolerant porous ammonia sensor, a one-step bi-polymer electrospinning with a single nozzle setup has been used. Notably, the bi-polymer nanofiber has a core-shell-like structure under characterization. The formation of the coated nanofiber structure based on the linker formation and bloom-out phenomenon eases the difficulties for core-shell structure fabrication to a great extent. During traditional core-shell nozzle electrospinning, there

are multiple challenges, including nozzle clog formation, flow control, and a complicated setup. The proposed method solves these challenges partially with comparable performance of nanofiber mat. Additionally, the water repellent ammonia sensor improves the resistance of current colorimetric sensor to liquid contact, which benefits the wearer especially those working in industrial environments.

Chapter 5: Along with the investigation of PPE embedded glucose sensors, the fundamentals for the formation of laser-induced graphene (LIG) have been stated. One of the critical requirements of LIG formation is aromatic ring chemical compounds of treated polymers. The other finding is the requirement of laser energy. Different transaction energies are needed for laser treatment on various polymers, which may sit in completely different ranges. For the LIG based glucose sensing platform, the proposed way improves the environmental friendliness of polycarbonate, which can be used to convert waste polymers into highly conductive materials that can potentially be used as electrothermal materials, sensing materials, and electrodes. This approach offers a new approach to the recycling and reuse of polycarbonate polymer, which is one of the major pollutants in the ocean.

## References

- [1] J. Rockström *et al.*, "A safe operating space for humanity," *nature*, vol. 461, no. 7263, pp. 472-475, 2009.
- [2] Y. Wang, J. Li, H. Jing, Q. Zhang, J. Jiang, and P. Biswas, "Laboratory evaluation and calibration of three low-cost particle sensors for particulate matter measurement," *Aerosol science and technology*, vol. 49, no. 11, pp. 1063-1077, 2015.

- [3] J. Wu, W. Cheng, H. Lu, Y. Shi, and Y. He, "The Effect of Particulate Matter on Visibility in Hangzhou, China," *Journal of Environmental Science and Management*, vol. 21, no. 1, 2018.
- [4] H. Al-Thani, M. Koç, and R. J. Isaifan, "A review on the direct effect of particulate atmospheric pollution on materials and its mitigation for sustainable cities and societies," *Environmental Science and Pollution Research*, vol. 25, no. 28, pp. 27839-27857, 2018/10/01 2018, doi: 10.1007/s11356-018-2952-8.
- [5] *Standard Specification for Barrier Face Coverings*, A. S. f. T. a. Materials, February 15, 2021 2021.
- [6] *Approval of respiratory protective devices*, T. N. I. f. O. S. a. Health, 1995.
- [7] C. Alexander, "The city as a mechanism for sustaining human contact," in *People and buildings*: Routledge, 2017, pp. 406-434.
- [8] J. Avossa, T. Batt, T. Pelet, S. P. Sidjanski, K. Schönenberger, and R. M. Rossi, "Polyamide Nanofiber-Based Air Filters for Transparent Face Masks," *ACS Applied Nano Materials*, vol. 4, no. 11, pp. 12401-12406, 2021/11/26 2021, doi: 10.1021/acsanm.1c02843.
- [9] W. G. Lindsley, J. D. Noti, F. M. Blachere, J. V. Szalajda, and D. H. Beezhold, "Efficacy of face shields against cough aerosol droplets from a cough simulator," *Journal of occupational and environmental hygiene*, vol. 11, no. 8, pp. 509-518, 2014.
- [10] V. V. Kadam, L. Wang, and R. Padhye, "Electrospun nanofibre materials to filter air pollutants – A review," *Journal of Industrial Textiles*, vol. 47, no. 8, pp. 2253-2280, 2018/05/01 2016, doi: 10.1177/1528083716676812.

- [11] S. Ramakrishnan, J. Johnson, M. Muzwar, R. Chetty, and K. Arul Prakash, "Numerical modeling of nanofibrous filter media and performance characteristics," *Chemical Engineering Science*, vol. 262, p. 118019, 2022/11/23/ 2022, doi: <https://doi.org/10.1016/j.ces.2022.118019>.
- [12] K. C. Dutton, "Overview and analysis of the meltblown process and parameters," *Journal of Textile and Apparel, Technology and Management*, vol. 6, no. 1, 2009.
- [13] W. Han, S. Xie, J. Shi, and X. Wang, "Study on airflow field and fiber motion with new melt blowing die," *Polymer Engineering & Science*, vol. 59, no. 6, pp. 1182-1189, 2019.
- [14] J. Drabek and M. Zatloukal, "Meltblown technology for production of polymeric microfibers/nanofibers: A review," *Physics of Fluids*, vol. 31, no. 9, p. 091301, 2019.
- [15] R. R. Bresee and W.-C. Ko, "Fiber formation during melt blowing," *International nonwovens journal*, no. 2, pp. 1558925003os-1200209, 2003.
- [16] A. De Rovère, R. L. Shambaugh, and E. A. O'rear, "Investigation of gravity-spun, melt-spun, and melt-blown polypropylene fibers using atomic force microscopy," *Journal of applied polymer science*, vol. 77, no. 9, pp. 1921-1937, 2000.
- [17] C. J. Ellison, A. Phatak, D. W. Giles, C. W. Macosko, and F. S. Bates, "Melt blown nanofibers: Fiber diameter distributions and onset of fiber breakup," *Polymer*, vol. 48, no. 11, pp. 3306-3316, 2007.
- [18] M. A. Hassan, B. Y. Yeom, A. Wilkie, B. Pourdeyhimi, and S. A. Khan, "Fabrication of nanofiber meltblown membranes and their filtration properties," *Journal of membrane science*, vol. 427, pp. 336-344, 2013.

- [19] G. F. Ward, "Meltblown nanofibres for nonwoven filtration applications," *Filtration & separation*, vol. 38, no. 9, pp. 42-43, 2001.
- [20] F. Zuo, D. H. Tan, Z. Wang, S. Jeung, C. W. Macosko, and F. S. Bates, "Nanofibers from melt blown fiber-in-fiber polymer blends," *ACS Macro Letters*, vol. 2, no. 4, pp. 301-305, 2013.
- [21] Z. Wang, X. Liu, C. W. Macosko, and F. S. Bates, "Nanofibers from water-extractable melt-blown immiscible polymer blends," *Polymer*, vol. 101, pp. 269-273, 2016.
- [22] R. Nayak *et al.*, "Fabrication and characterisation of polypropylene nanofibres by meltblowing process using different fluids," *Journal of Materials Science*, vol. 48, no. 1, pp. 273-281, 2013.
- [23] R. Nayak, R. Padhye, I. L. Kyratzis, Y. B. Truong, and L. Arnold, "Recent advances in nanofibre fabrication techniques," *Textile Research Journal*, vol. 82, no. 2, pp. 129-147, 2012.
- [24] M. Guo, H. Liang, Z. Luo, Q. Chen, and W. Wei, "Study on melt-blown processing, web structure of polypropylene nonwovens and its BTX adsorption," *Fibers and Polymers*, vol. 17, no. 2, pp. 257-265, 2016, doi: 10.1007/s12221-016-5592-y.
- [25] J. Zhang, G. Chen, G. S. Bhat, H. Azari, and H. Pen, "Electret characteristics of melt-blown polylactic acid fabrics for air filtration application," *Journal of Applied Polymer Science*, vol. 137, no. 4, p. 48309, 2020, doi: <https://doi.org/10.1002/app.48309>.

- [26] X. Y. D. Soo *et al.*, "Polylactic acid face masks: Are these the sustainable solutions in times of COVID-19 pandemic?," *Science of The Total Environment*, vol. 807, p. 151084, 2022/02/10/ 2022, doi: <https://doi.org/10.1016/j.scitotenv.2021.151084>.
- [27] J. Drabek and M. Zatloukal, "Influence of long chain branching on fiber diameter distribution for polypropylene nonwovens produced by melt blown process," *Journal of Rheology*, vol. 63, no. 4, pp. 519-532, 2019.
- [28] N. Fedorova, "Investigation of the utility of islands-in-the-sea bicomponent fiber technology in the spunbond process [dissertation]," *NC State University, Raleigh*, 2006.
- [29] P. Sikdar, G. S Bhat, D. Hinchliffe, S. Islam, and B. Condon, "Microstructure and physical properties of composite nonwovens produced by incorporating cotton fibers in elastic spunbond and meltblown webs for medical textiles," *Journal of Industrial Textiles*, vol. 51, no. 4\_suppl, pp. 6028S-6050S, 2022.
- [30] K. Chen, A. Ghosal, A. L. Yarin, and B. Pourdeyhimi, "Modeling of spunbond formation process of polymer nonwovens," *Polymer*, vol. 187, p. 121902, 2020.
- [31] H. Lim, "A review of spunbond process," *Journal of Textile and Apparel, Technology and Management*, vol. 6, no. 3, 2010.
- [32] V. K. Midha and A. Dakuri, "Spun bonding Technology and Fabric Properties: a Review," *Journal of Textile Engineering & Fashion Technology*, vol. 1, no. 4, 2017, doi: 10.15406/jteft.2017.01.00023.
- [33] I. Alghoraibi and S. Alomari, "Different Methods for Nanofiber Design and Fabrication," in *Handbook of Nanofibers*, 2018, ch. Chapter 11-2, pp. 1-46.

- [34] Y. Li *et al.*, "Multifunctional fibroblasts enhanced via thermal and freeze-drying post-treatments of aligned electrospun nanofiber membranes," *Advanced Fiber Materials*, vol. 3, no. 1, pp. 26-37, 2021.
- [35] Y. Li *et al.*, "Recent advances on water-splitting electrocatalysis mediated by noble-metal-based nanostructured materials," *Advanced Energy Materials*, vol. 10, no. 11, p. 1903120, 2020.
- [36] H. Zhao and Y. Lei, "3D nanostructures for the next generation of high-performance nanodevices for electrochemical energy conversion and storage," *Advanced Energy Materials*, vol. 10, no. 28, p. 2001460, 2020.
- [37] S. Ahmed and C. M. Hussain, *Green and Sustainable Advanced Materials, Volume 2: Applications*. John Wiley & Sons, 2018.
- [38] D. Liang, B. S. Hsiao, and B. Chu, "Functional electrospun nanofibrous scaffolds for biomedical applications," *Advanced drug delivery reviews*, vol. 59, no. 14, pp. 1392-1412, 2007.
- [39] A. A. Almetwally, M. El-Sakhawy, M. Elshakankery, and M. Kasem, "Technology of nano-fibers: Production techniques and properties-Critical review," *J. Text. Assoc*, vol. 78, no. 1, pp. 5-14, 2017.
- [40] N. Bhardwaj and S. C. Kundu, "Electrospinning: a fascinating fiber fabrication technique," *Biotechnol Adv*, vol. 28, no. 3, pp. 325-47, May-Jun 2010, doi: 10.1016/j.biotechadv.2010.01.004.

- [41] C. Liu *et al.*, "Transparent air filter for high-efficiency PM<sub>2.5</sub> capture," *Nature communications*, vol. 6, no. 1, pp. 1-9, 2015.
- [42] J. A. Matthews, G. E. Wnek, D. G. Simpson, and G. L. Bowlin, "Electrospinning of collagen nanofibers," *Biomacromolecules*, vol. 3, no. 2, pp. 232-238, 2002.
- [43] P. Katta, M. Alessandro, R. Ramsier, and G. Chase, "Continuous electrospinning of aligned polymer nanofibers onto a wire drum collector," *Nano letters*, vol. 4, no. 11, pp. 2215-2218, 2004.
- [44] C. Xu, R. Inai, M. Kotaki, and S. Ramakrishna, "Aligned biodegradable nanofibrous structure: a potential scaffold for blood vessel engineering," *Biomaterials*, vol. 25, no. 5, pp. 877-886, 2004.
- [45] D. Li, Y. Wang, and Y. Xia, "Electrospinning of polymeric and ceramic nanofibers as uniaxially aligned arrays," *Nano letters*, vol. 3, no. 8, pp. 1167-1171, 2003.
- [46] A. Khalf and S. V. Madihally, "Recent advances in multiaxial electrospinning for drug delivery," *European Journal of Pharmaceutics and Biopharmaceutics*, vol. 112, pp. 1-17, 2017.
- [47] Y. Li *et al.*, "Developments of Advanced Electrospinning Techniques: A Critical Review," *Advanced Materials Technologies*, vol. 6, no. 11, 2021, doi: 10.1002/admt.202100410.
- [48] S. Theron, A. L. Yarin, E. Zussman, and E. Kroll, "Multiple jets in electrospinning: experiment and modeling," *Polymer*, vol. 46, no. 9, pp. 2889-2899, 2005.

- [49] W. Tomaszewski and M. Szadkowski, "Investigation of electrospinning with the use of a multi-jet electrospinning head," *Fibres and Textiles in Eastern Europe*, vol. 13, no. 4, p. 22, 2005.
- [50] H. Qu, S. Wei, and Z. Guo, "Coaxial electrospun nanostructures and their applications," *Journal of Materials Chemistry A*, vol. 1, no. 38, pp. 11513-11528, 2013.
- [51] Y. Lu *et al.*, "Coaxial electrospun fibers: applications in drug delivery and tissue engineering," *Wiley Interdisciplinary Reviews: Nanomedicine and Nanobiotechnology*, vol. 8, no. 5, pp. 654-677, 2016.
- [52] F. E. Ahmed, B. S. Lalia, and R. Hashaikeh, "A review on electrospinning for membrane fabrication: Challenges and applications," *Desalination*, vol. 356, pp. 15-30, 2015, doi: 10.1016/j.desal.2014.09.033.
- [53] W. E. Teo and S. Ramakrishna, "A review on electrospinning design and nanofibre assemblies," *Nanotechnology*, vol. 17, no. 14, pp. R89-R106, Jul 28 2006, doi: 10.1088/0957-4484/17/14/R01.
- [54] Y. Deng, T. Lu, J. Cui, S. Keshari Samal, R. Xiong, and C. Huang, "Bio-based electrospun nanofiber as building blocks for a novel eco-friendly air filtration membrane: A review," *Separation and Purification Technology*, vol. 277, p. 119623, 2021/12/15/ 2021, doi: <https://doi.org/10.1016/j.seppur.2021.119623>.
- [55] D. Lv *et al.*, "Green Electrospun Nanofibers and Their Application in Air Filtration," *Macromolecular Materials and Engineering*, vol. 303, no. 12, p. 1800336, 2018, doi: <https://doi.org/10.1002/mame.201800336>.

- [56] B. Maze, H. V. Tafreshi, Q. Wang, and B. Pourdeyhimi, "A simulation of unsteady-state filtration via nanofiber media at reduced operating pressures," *Journal of aerosol science*, vol. 38, no. 5, pp. 550-571, 2007.
- [57] T. Xia, Y. Bian, L. Zhang, and C. Chen, "Relationship between pressure drop and face velocity for electrospun nanofiber filters," *Energy and Buildings*, vol. 158, pp. 987-999, 2018/01/01/ 2018, doi: <https://doi.org/10.1016/j.enbuild.2017.10.073>.
- [58] A. Brochocka, K. Majchrzycka, and K. Makowski, "Modified melt-blown nonwovens for respiratory protective devices against nanoparticles," *Fibres & Textiles in Eastern Europe*, 2013.
- [59] A. Kilic, E. Shim, and B. Pourdeyhimi, "Electrostatic capture efficiency enhancement of polypropylene electret filters with barium titanate," *Aerosol Science and Technology*, vol. 49, no. 8, pp. 666-673, 2015.
- [60] X. Zhang *et al.*, "Multi-Layered, Corona Charged Melt Blown Nonwovens as High Performance PM(0.3) Air Filters," *Polymers (Basel)*, vol. 13, no. 4, Feb 4 2021, doi: 10.3390/polym13040485.
- [61] H. Zhang, J. Liu, X. Zhang, C. Huang, and X. Jin, "Design of electret polypropylene melt blown air filtration material containing nucleating agent for effective PM2.5 capture," *RSC Adv*, vol. 8, no. 15, pp. 7932-7941, Feb 19 2018, doi: 10.1039/c7ra10916d.
- [62] T. T. Li *et al.*, "Zeolitic Imidazolate Framework-8/Polypropylene-Polycarbonate Barklike Meltblown Fibrous Membranes by a Facile in Situ Growth Method for Efficient PM(2.5) Capture," *ACS Appl Mater Interfaces*, vol. 12, no. 7, pp. 8730-8739, Feb 19 2020, doi: 10.1021/acsami.9b21340.

- [63] T. T. Li *et al.*, "Polypropylene/Polyvinyl Alcohol/Metal-Organic Framework-Based Melt-Blown Electrospun Composite Membranes for Highly Efficient Filtration of PM(2.5)," *Nanomaterials (Basel)*, vol. 10, no. 10, Oct 14 2020, doi: 10.3390/nano10102025.
- [64] J. Liu *et al.*, "Low resistance bicomponent spunbond materials for fresh air filtration with ultra-high dust holding capacity," *RSC Advances*, vol. 7, no. 69, pp. 43879-43887, 2017, doi: 10.1039/c7ra07694k.
- [65] J. Liu, H. Zhang, H. Gong, X. Zhang, Y. Wang, and X. Jin, "Polyethylene/Polypropylene Bicomponent Spunbond Air Filtration Materials Containing Magnesium Stearate for Efficient Fine Particle Capture," *ACS Appl Mater Interfaces*, vol. 11, no. 43, pp. 40592-40601, Oct 30 2019, doi: 10.1021/acsami.9b13162.
- [66] Z. Heng, Q. Xiaoming, Z. Qi, and Y. Zhaohang, "Research on structure characteristics and filtration performances of PET-PA6 hollow segmented-pie bicomponent spunbond nonwovens fibrillated by hydro entangle method," *Journal of Industrial Textiles*, vol. 45, no. 1, pp. 48-65, 2014, doi: 10.1177/1528083714521073.
- [67] Y. Duo *et al.*, "Easily splittable hollow segmented-pie microfiber nonwoven material with excellent filtration and thermal-wet comfort for energy savings," *Journal of Materials Research and Technology*, vol. 17, pp. 876-887, 2022, doi: 10.1016/j.jmrt.2022.01.047.
- [68] B. Y. Yeom and B. Pourdeyhimi, "Aerosol filtration properties of PA6/PE islands-in-the-sea bicomponent spunbond web fibrillated by high-pressure water jets," *Journal of Materials Science*, vol. 46, no. 17, pp. 5761-5767, 2011, doi: 10.1007/s10853-011-5531-7.

- [69] Q. Peng *et al.*, "Preparation of electrospayed composite coated microporous filter for particulate matter capture," *Nano Select*, vol. 3, no. 3, pp. 555-566, 2021, doi: 10.1002/nano.202100186.
- [70] W. Yim, D. Cheng, S. H. Patel, R. Kou, Y. S. Meng, and J. V. Jokerst, "KN95 and N95 Respirators Retain Filtration Efficiency despite a Loss of Dipole Charge during Decontamination," *ACS Applied Materials & Interfaces*, vol. 12, no. 49, pp. 54473-54480, 2020/12/09 2020, doi: 10.1021/acsami.0c17333.
- [71] Y. Ahn *et al.*, "Development of high efficiency nanofilters made of nanofibers," *Current Applied Physics*, vol. 6, no. 6, pp. 1030-1035, 2006.
- [72] R. Zhang *et al.*, "Nanofiber air filters with high-temperature stability for efficient PM2. 5 removal from the pollution sources," *Nano letters*, vol. 16, no. 6, pp. 3642-3649, 2016.
- [73] E. Scholten, L. Bromberg, G. C. Rutledge, and T. A. Hatton, "Electrospun polyurethane fibers for absorption of volatile organic compounds from air," *ACS applied materials & interfaces*, vol. 3, no. 10, pp. 3902-3909, 2011.
- [74] R. Gopal *et al.*, "Electrospun nanofibrous polysulfone membranes as pre-filters: Particulate removal," *Journal of membrane science*, vol. 289, no. 1-2, pp. 210-219, 2007.
- [75] X. Huang *et al.*, "Hierarchical electrospun nanofibers treated by solvent vapor annealing as air filtration mat for high-efficiency PM2. 5 capture," *Sci. China Mater*, vol. 62, no. 3, pp. 423-436, 2019.

- [76] Z. Cheng, Y. Zhang, Z. Han, L. Cui, L. Kang, and F. Zhang, "A novel preparation of anti-layered poly (vinylalcohol)–polyacrylonitrile (PVA/PAN) membrane for air filtration by electrospinning," *RSC advances*, vol. 6, no. 88, pp. 85545-85550, 2016.
- [77] H. Li, Z. Wang, H. Zhang, and Z. Pan, "Nanoporous PLA/(chitosan nanoparticle) composite fibrous membranes with excellent air filtration and antibacterial performance," *Polymers*, vol. 10, no. 10, p. 1085, 2018.
- [78] S. Sangkham, "Face mask and medical waste disposal during the novel COVID-19 pandemic in Asia," *Case Studies in Chemical and Environmental Engineering*, vol. 2, p. 100052, 2020/09/01/ 2020, doi: <https://doi.org/10.1016/j.cscee.2020.100052>.
- [79] J. Hu, Z. Xiong, Y. Liu, and J. Lin, "A biodegradable composite filter made from electrospun zein fibers underlaid on the cellulose paper towel," *International Journal of Biological Macromolecules*, vol. 204, pp. 419-428, 2022.
- [80] H. Souzandeh, L. Scudiero, Y. Wang, and W.-H. Zhong, "A disposable multi-functional air filter: paper towel/protein nanofibers with gradient porous structures for capturing pollutants of broad species and sizes," *ACS Sustainable Chemistry & Engineering*, vol. 5, no. 7, pp. 6209-6217, 2017.
- [81] X. Fan, Y. Wang, W.-H. Zhong, and S. Pan, "Hierarchically structured all-biomass air filters with high filtration efficiency and low air pressure drop based on pickering emulsion," *ACS applied materials & interfaces*, vol. 11, no. 15, pp. 14266-14274, 2019.
- [82] Q. Zhang, Q. Li, T. M. Young, D. P. Harper, and S. Wang, "A novel method for fabricating an electrospun poly (vinyl alcohol)/cellulose nanocrystals composite nanofibrous filter

- with low air resistance for high-efficiency filtration of particulate matter," *ACS Sustainable Chemistry & Engineering*, vol. 7, no. 9, pp. 8706-8714, 2019.
- [83] X. Gao, J. Gou, L. Zhang, S. Duan, and C. Li, "A silk fibroin based green nano-filter for air filtration," *RSC advances*, vol. 8, no. 15, pp. 8181-8189, 2018.
- [84] S. Choi *et al.*, "Biodegradable, efficient, and breathable multi-use face mask filter," *Advanced Science*, vol. 8, no. 6, p. 2003155, 2021.
- [85] X. Yu *et al.*, "Hydrophobic cross-linked zein-based nanofibers with efficient air filtration and improved moisture stability," *Chemical Engineering Journal*, vol. 396, p. 125373, 2020.
- [86] D. Kwak, Y. Lei, and R. Maric, "Ammonia gas sensors: A comprehensive review," *Talanta*, vol. 204, pp. 713-730, 2019.
- [87] G. K. Mani and J. B. B. Rayappan, "A highly selective and wide range ammonia sensor— Nanostructured ZnO: Co thin film," *Materials Science and Engineering: B*, vol. 191, pp. 41-50, 2015.
- [88] S. Giddey, S. Badwal, and A. Kulkarni, "Review of electrochemical ammonia production technologies and materials," *International Journal of Hydrogen Energy*, vol. 38, no. 34, pp. 14576-14594, 2013.
- [89] G. Korotcenkov and B. K. Cho, "Metal oxide composites in conductometric gas sensors: Achievements and challenges," *Sensors and Actuators B: Chemical*, vol. 244, pp. 182-210, 2017, doi: 10.1016/j.snb.2016.12.117.

- [90] C. S. Rout, M. Hegde, A. Govindaraj, and C. Rao, "Ammonia sensors based on metal oxide nanostructures," *Nanotechnology*, vol. 18, no. 20, p. 205504, 2007.
- [91] J. Huang, J. Wang, C. Gu, K. Yu, F. Meng, and J. Liu, "A novel highly sensitive gas ionization sensor for ammonia detection," *Sensors and Actuators A: Physical*, vol. 150, no. 2, pp. 218-223, 2009.
- [92] Y. Zhao and Y. Zhu, "Room temperature ammonia sensing properties of W18O49 nanowires," *Sensors and Actuators B: Chemical*, vol. 137, no. 1, pp. 27-31, 2009.
- [93] Y. Zeng *et al.*, "Enhanced ammonia sensing performances of Pd-sensitized flowerlike ZnO nanostructure," *Sensors and Actuators B: Chemical*, vol. 156, no. 1, pp. 395-400, 2011.
- [94] P.-G. Su and L.-Y. Yang, "NH<sub>3</sub> gas sensor based on Pd/SnO<sub>2</sub>/RGO ternary composite operated at room-temperature," *Sensors and Actuators B: Chemical*, vol. 223, pp. 202-208, 2016.
- [95] Q. Qi *et al.*, "SnO<sub>2</sub> nanoparticle-coated In<sub>2</sub>O<sub>3</sub> nanofibers with improved NH<sub>3</sub> sensing properties," *Sensors and Actuators B: Chemical*, vol. 194, pp. 440-446, 2014.
- [96] G. Korotcenkov, "Metal oxides for solid-state gas sensors: What determines our choice?," *Materials Science and Engineering: B*, vol. 139, no. 1, pp. 1-23, 2007.
- [97] X. Guo *et al.*, "A portable sensor for in-situ measurement of ammonia based on near-infrared laser absorption spectroscopy," *Optics and Lasers in Engineering*, vol. 115, pp. 243-248, 2019.

- [98] Y. Gu and J. Huang, "Colorimetric detection of gaseous ammonia by polyaniline nanocoating of natural cellulose substances," *Colloids and Surfaces A: Physicochemical and Engineering Aspects*, vol. 433, pp. 166-172, 2013.
- [99] D.-H. Kim *et al.*, "Colorimetric dye-loaded nanofiber yarn: Eye-readable and weavable gas sensing platform," *ACS nano*, vol. 14, no. 12, pp. 16907-16918, 2020.
- [100] Y. Sadaoka, Y. Sakai, and M. Yamada, "Optical properties of sulfonephthalein dyes entrapped within polymer matrices for quantification of ammonia vapour and humidity in air," *Journal of Materials Chemistry*, vol. 3, no. 8, pp. 877-881, 1993.
- [101] J. Courbat, D. Briand, J. Damon-Lacoste, J. Wöllenstein, and N. De Rooij, "Evaluation of pH indicator-based colorimetric films for ammonia detection using optical waveguides," *Sensors and Actuators B: Chemical*, vol. 143, no. 1, pp. 62-70, 2009.
- [102] R. E. Oweyung, M. J. Panzer, and S. R. Sonkusale, "Colorimetric gas sensing washable threads for smart textiles," *Scientific reports*, vol. 9, no. 1, pp. 1-8, 2019.
- [103] A. T. Hoang, Y. B. Cho, J.-S. Park, Y. Yang, and Y. S. Kim, "Sensitive naked-eye detection of gaseous ammonia based on dye-impregnated nanoporous polyacrylonitrile mats," *Sensors and Actuators B: Chemical*, vol. 230, pp. 250-259, 2016, doi: 10.1016/j.snb.2016.02.058.
- [104] J. Hunt, "Exhaled breath condensate pH assays," *Immunology and allergy clinics of North America*, vol. 27, no. 4, pp. 597-606, 2007.
- [105] E. D. Rosen and B. M. Spiegelman, "Adipocytes as regulators of energy balance and glucose homeostasis," *Nature*, vol. 444, no. 7121, pp. 847-853, 2006.

- [106] D. R. Whiting, L. Guariguata, C. Weil, and J. Shaw, "IDF diabetes atlas: global estimates of the prevalence of diabetes for 2011 and 2030," *Diabetes research and clinical practice*, vol. 94, no. 3, pp. 311-321, 2011.
- [107] H. Lee, Y. J. Hong, S. Baik, T. Hyeon, and D. H. Kim, "Enzyme-based glucose sensor: from invasive to wearable device," *Advanced healthcare materials*, vol. 7, no. 8, p. 1701150, 2018.
- [108] D. Bruen, C. Delaney, L. Florea, and D. Diamond, "Glucose sensing for diabetes monitoring: recent developments," *Sensors*, vol. 17, no. 8, p. 1866, 2017.
- [109] J. C. Claussen *et al.*, "Nanostructuring platinum nanoparticles on multilayered graphene petal nanosheets for electrochemical biosensing," *Advanced Functional Materials*, vol. 22, no. 16, pp. 3399-3405, 2012.
- [110] P. Makaram, D. Owens, and J. Aceros, "Trends in nanomaterial-based non-invasive diabetes sensing technologies," *Diagnostics*, vol. 4, no. 2, pp. 27-46, 2014.
- [111] H. Teymourian, A. Barfidokht, and J. Wang, "Electrochemical glucose sensors in diabetes management: an updated review (2010-2020)," *Chem Soc Rev*, vol. 49, no. 21, pp. 7671-7709, Nov 7 2020, doi: 10.1039/d0cs00304b.
- [112] H. Yao, A. J. Shum, M. Cowan, I. Lähdesmäki, and B. A. Parviz, "A contact lens with embedded sensor for monitoring tear glucose level," *Biosensors and Bioelectronics*, vol. 26, no. 7, pp. 3290-3296, 2011/03/15/ 2011, doi: <https://doi.org/10.1016/j.bios.2010.12.042>.

- [113] J. Kim *et al.*, "Wearable smart sensor systems integrated on soft contact lenses for wireless ocular diagnostics," *Nat Commun*, vol. 8, p. 14997, Apr 27 2017, doi: 10.1038/ncomms14997.
- [114] J. R. Sempionatto *et al.*, "Eyeglasses-based tear biosensing system: Non-invasive detection of alcohol, vitamins and glucose," *Biosensors and Bioelectronics*, vol. 137, pp. 161-170, 2019.
- [115] M. X. Chu *et al.*, "Soft contact lens biosensor for in situ monitoring of tear glucose as non-invasive blood sugar assessment," *Talanta*, vol. 83, no. 3, pp. 960-965, 2011.
- [116] R. Agrawal *et al.*, "Noninvasive method for glucose level estimation by saliva," *J Diabetes Metab*, vol. 4, no. 5, p. 266, 2013.
- [117] W. Zhang, Y. Du, and M. L. Wang, "Noninvasive glucose monitoring using saliva nano-biosensor," *Sensing and Bio-Sensing Research*, vol. 4, pp. 23-29, 2015.
- [118] T. Arakawa *et al.*, "Mouthguard biosensor with telemetry system for monitoring of saliva glucose: A novel cavitas sensor," *Biosensors and Bioelectronics*, vol. 84, pp. 106-111, 2016.
- [119] J. Kim, A. S. Campbell, and J. Wang, "Wearable non-invasive epidermal glucose sensors: A review," *Talanta*, vol. 177, pp. 163-170, Jan 15 2018, doi: 10.1016/j.talanta.2017.08.077.
- [120] J. Heikenfeld *et al.*, "Accessing analytes in biofluids for peripheral biochemical monitoring," *Nature biotechnology*, vol. 37, no. 4, pp. 407-419, 2019.
- [121] G. Rao *et al.*, "Reverse iontophoresis: Noninvasive glucose monitoring in vivo in humans," *Pharmaceutical research*, vol. 12, no. 12, pp. 1869-1873, 1995.

- [122] M. Tierney, J. Tamada, R. Potts, L. Jovanovic, S. Garg, and C. R. Team, "Clinical evaluation of the GlucoWatch® biographer: a continual, non-invasive glucose monitor for patients with diabetes," *Biosensors and Bioelectronics*, vol. 16, no. 9-12, pp. 621-629, 2001.
- [123] A. J. Bandodkar, W. Jia, C. Yardımcı, X. Wang, J. Ramirez, and J. Wang, "Tattoo-based noninvasive glucose monitoring: a proof-of-concept study," *Analytical chemistry*, vol. 87, no. 1, pp. 394-398, 2015.
- [124] Y. Chen *et al.*, "Skin-like biosensor system via electrochemical channels for noninvasive blood glucose monitoring," *Science advances*, vol. 3, no. 12, p. e1701629, 2017.
- [125] K. Roberts, A. Jaffe, C. Verge, and P. S. Thomas, "Noninvasive monitoring of glucose levels: is exhaled breath the answer?," *Journal of diabetes science and technology*, vol. 6, no. 3, pp. 659-664, 2012.
- [126] B. H. Chu *et al.*, "Aluminum Gallium Nitride (GaN)/GaN High Electron Mobility Transistor-Based Sensors for Glucose Detection in Exhaled Breath Condensate," *Journal of Diabetes Science and Technology*, vol. 4, no. 1, pp. 171-179, 2010, doi: 10.1177/193229681000400122.
- [127] D. Tankasala, G. P. Ng, M. S. Smith, J. R. Bendell, and J. C. Linnes, "Selective collection and condensation of exhaled breath for glucose detection," in *2018 40th Annual International Conference of the IEEE Engineering in Medicine and Biology Society (EMBC)*, 2018: IEEE, pp. 3890-3893.
- [128] S. Y. Oh *et al.*, "Skin-Attachable, Stretchable Electrochemical Sweat Sensor for Glucose and pH Detection," *ACS Appl Mater Interfaces*, vol. 10, no. 16, pp. 13729-13740, Apr 25 2018, doi: 10.1021/acsami.8b03342.

- [129] H. Lee *et al.*, "A graphene-based electrochemical device with thermoresponsive microneedles for diabetes monitoring and therapy," *Nat Nanotechnol*, vol. 11, no. 6, pp. 566-572, Jun 2016, doi: 10.1038/nnano.2016.38.
- [130] H. Lee *et al.*, "Wearable/disposable sweat-based glucose monitoring device with multistage transdermal drug delivery module," *Science advances*, vol. 3, no. 3, p. e1601314, 2017.
- [131] A. Martín *et al.*, "Epidermal microfluidic electrochemical detection system: Enhanced sweat sampling and metabolite detection," *ACS sensors*, vol. 2, no. 12, pp. 1860-1868, 2017.
- [132] J. Lin *et al.*, "Laser-induced porous graphene films from commercial polymers," *Nature communications*, vol. 5, no. 1, p. 5714, 2014.
- [133] R. Ye *et al.*, "In situ formation of metal oxide nanocrystals embedded in laser-induced graphene," *Acs Nano*, vol. 9, no. 9, pp. 9244-9251, 2015.
- [134] Z. You *et al.*, "Laser-induced noble metal nanoparticle-graphene composites enabled flexible biosensor for pathogen detection," *Biosensors and Bioelectronics*, vol. 150, p. 111896, 2020.
- [135] Y. Luo *et al.*, "Stretchable and Flexible Non-Enzymatic Glucose Sensor Based on Poly(ether sulfone)-Derived Laser-Induced Graphene for Wearable Skin Diagnostics," *Advanced Materials Technologies*, vol. 7, no. 9, p. 2101571, 2022.

- [136] J. Zhao *et al.*, "Co<sub>3</sub>O<sub>4</sub> nanoparticles embedded in laser-induced graphene for a flexible and highly sensitive enzyme-free glucose biosensor," *Sensors and Actuators B: Chemical*, vol. 347, p. 130653, 2021.

## **Chapter 2: Development of a one-piece full-head covered respirator with clear face visor for greater personal protection**

Rong Wu<sup>1#</sup>, Panashe Mudzi<sup>1#</sup>, Dariush Firouzi<sup>1,2</sup>, Chan Y. Ching<sup>1</sup>, P. Ravi Selvaganapathy<sup>1\*</sup>

<sup>1</sup>Department of Mechanical Engineering, McMaster University, Hamilton, ON CANADA

<sup>2</sup>RONCO, 70 Planchet Road, Concord, ON L4K 2C7, Canada

\*Corresponding Author: [selvaga@mcmaster.ca](mailto:selvaga@mcmaster.ca); +1 905 525 9140 ext. 27435

#Equal contribution

### **KEYWORDS:**

Full face respirator, filtration, personal protection equipment, one-piece, low cost.

### **Status: Ready to submit**

**Contribution:** The proposed design in this chapter provides novel design substitutes traditional face shield and mask combination, while providing a clear view of the wearing individual's face and good filtration performance with common tools and materials for urgent demand.

## **Abstract**

Due to supply chain shortages of personal protective equipment (PPE) during the COVID-19 pandemic, the ability to quickly manufacture high quality PPEs using simple methods has become important especially during global pandemics. Here, we have developed a new one-piece full head covered full face respirator that has high level of filtration efficiency and can be made without industrial equipment for use in an emergency when conventional PPEs are not available. Prototypes using nonwoven polypropylene and woven cloth fabric, polycarbonate visor and foam were fabricated. A pressure sensitive adhesive was used to bond all the components together which provides a relatively simple method for manufacture without the need for specialized industrial equipment and useful in resource poor settings. Tests were performed to characterize the performance of the full-face respirator by measuring the filtration efficiency based on difference of particle concentration between ambient environment, the inside temperature, humidity and carbon dioxide level during use. The particle filtration results measured at breathing rates ranging between 6 l/min (rest breathing rate) and 90 l/min (extreme breathing rate) with 75nm median diameter of NaCl particles showed that the face shield with polypropylene fabric had a filtration efficiency of 95% to 99%. Temperature and humidity levels were comparable to that of wearing N95 respirator over the same time period. Carbon dioxide levels below 2000ppm for 2ply design mostly and below 1290 ppm for 1ply design were significantly below the recommended limit of 5,000 ppm which is the Permissible Exposure Limit (PEL) established by OSHA and were around the levels that were comfortable and did not produce even mild cognitive impairment. Due to the simplicity and means of fabrication, the full-face respirator provides an attractive alternative design to wearing both a face mask and face shield and may be of use in emergency situations or in resource poor settings.

## **1. Introduction**

Since the World Health Organisation (WHO) declared the Coronavirus disease 2019 (COVID-19) outbreak a worldwide public health emergency (PHEIC) in January 2020, the public demand and use of personal protective equipment (PPE) has grown exponentially[1]. This has led briefly to a worldwide shortage of PPE and resulted in the PPE market whiplashed by arbitrary price increases and lack of access to PPE for health care workers [2] . Transmission of the COVID-19 virus through inhalation of droplets that are generated during expiratory events such as talking, sneezing, breathing and coughing was one of the important ways it was spread [3] . The common types of PPE that healthcare workers and the general public use in order to protect their facial areas from splashes, sprays, and spatter of body fluids are mainly a combination of face shields and either medical masks or N95 respirators [4]. Due to the developing evidence regarding transmission of COVID-19, the WHO recommendations relating to the use of PPE in handling of patients with/suspected of infection have evolved [5]. Different clinical environments require different PPE during the COVID-19 pandemic. For instance, a healthcare worker within a one-meter radius of the patient is required to have eye protection, medical mask, disposable gowns and gloves at the same time. Within high-risk areas, it is recommended for health workers to wear a scrub cap visor or face shield, face mask, disposable gown and gloves [5]. The WHO also recommend the use of PPE in a community setting in the context of COVID-19 [1].

The use of traditional face shields without full head coverage can significantly reduce short-term exposure of healthcare workers from larger infectious aerosol particles; however, they are less effective against smaller particles that are able to remain airborne for extended periods of time, thereby increasing the chances of them flowing around the face shield to be inhaled [6]. Another

study showed that face shields block a small portion of cough aerosol for small respiratory aerosols but when it is worn in addition to a face mask, the surface contamination on the face mask is reduced and hence leads to a reduction in hand contamination when the face mask is removed [7]. There are normally two factors that influence the performance of face masks, high filtration efficiency filter materials and the design of fitting. Fitting to keep mask sealed to provide sufficient protection is critical but masks are often worn with poor fit and leakages leading to poor actual filtration efficiency. A tight fitting mask is also not recommended to be worn over long durations of time especially during events like sneezing where the internal pressure can affect internal organs [8]. Therefore, a face shield is a necessary additional layer of PPE to a face mask to provide better protection and minimize leakage and contamination of the user from splashes. There is growing interest in developing next generation PPE which reduces the number of type of PPE to be worn simultaneously for better protection.

In this paper we introduce a new design of a full-face respirator for infection control. This PPE offers comparable performance to the combination of the conventional face shield and face mask for splash prevention and particulate filtration while providing a clear view of the wearer's face. The full-face respirator was fabricated without the use of special industrial equipment or expertise, which can be appealing to a number of developing countries to meet their PPE requirements in emergencies. The prototypes were tested for particle filtration efficiency (PFE) using a manikin head form connected to a breathing simulator and a *PortaCount*<sup>®</sup> Respirator Fit Tester. We also monitored and report the change in internal conditions within the respirator such as temperature, relative humidity and carbon dioxide levels using a male and female subject wearing the full head face shield. Overall, we investigated the new design and fabrication method of 'full-face respirator' that can be manufactured with minimal resources and has the potential to replace wearing of both

a face mask and face shield by public and health care workers under an emergency when conventional PPEs are not available.

## **2. Methods and materials**

### **2.1 Fabrication of full face respirator prototypes**

The main factors taken into consideration for the design and fabrication method were cost and simplicity. Currently, the mass-produced PPE are made using specialized industrial machines which may not be cost effective for some developing countries to obtain during a global pandemic. To tackle this challenge, the current full face respirator was designed to allow for fabrication without specialized industrial equipment, and all the apparatus used were intended to be easily accessible or in time periods where there is a severe shortage of respirators.

A schematic of the fabrication process is illustrated in Figure 2.1 The (50 g/m<sup>2</sup>) Spunbonded Polypropylene (PP) fabric was from Nolar Industries Ltd, Concord, ON, Canada, while the woven cotton fabric (122.8 g/m<sup>2</sup>) was from RONCO, Concord, ON, Canada. Pressure sensitive adhesive (PSA - 9472LE) with a width of 12.7 mm was from Adheco Ltd, Scarborough, ON, Canada. The polycarbonate film, 25.4 × 25.4 mm strips of foam and 25.4 mm wide elastic were bought from Amazon Inc. The fabric roll was cut into separate components of the face shield hood as shown in Figure 2.1(a). Polycarbonate was cut into a 290 mm × 180 mm film as shown in Figure 2.1 (b) for use as the visor. Foam and elastic band strips were cut to an unstretched length of 29 mm. PSA was used to bond together all the components into a complete full face respirator as shown in Figure 2.1 (c). The elastic band was used as the first support on the head when wearing the prototypes. Three prototypes were produced that included one with a single ply of PP, double ply

of PP and single ply of woven cotton cloth. Hand pressing was adequate for the PSA to bond all the parts together with no need for special manufacturing equipment.

## **2.2 Relative humidity, temperature and CO<sub>2</sub> level tests**

The change in the relative humidity, temperature and CO<sub>2</sub> level inside the full head face shield was measured on two volunteers from both genders (a healthy male and female in their 20s) for three different material combinations while they were performing sedentary work over a 100 min period to evaluate the comfort level of proposed respirator in the daily usage circumstance. The ambient temperature was 20 to 22°C, with 20% relative humidity (RH%) and CO<sub>2</sub> level of 350 ppm. The humidity and temperature were measured using a sensor set (39175K45, McMaster-Carr, US) that measures both the test and ambient conditions simultaneously with  $\pm 5\%$  and  $\pm 1^\circ\text{C}$  accuracy, respectively. The detector consists of a sensor was attached inside the full-face respirator hood's dead space using PSA and another external sensor with an LED display that measures room ambient humidity and temperature conditions. In this way, both the environment inside the respirator and conditions in the ambient room were monitored and recorded. The tests were performed with the respirator hood being worn continuously for 100 minutes at a moderate breathing rate (wearer was sitting with minimal walking movements). During the first 20 minutes, the changes in relative humidity and temperature were recorded every minutes. From 20 minutes onwards, the readings were recorded at 10-minute intervals. The ambient relative humidity and temperature conditions were recorded before and during each test. Two repeats were performed and recorded with different participants.

The CO<sub>2</sub> levels (ppm) inside the full face respirator was measured using a mini carbon dioxide detector (model number JSM-131SC, KKmoon, Amazon, CA) with <15% detection error and a

recommended temperature and humidity range of 18-50 °C and 10-70% RH, respectively. The sensor was attached inside the hood dead space using PSA and the CO<sub>2</sub> levels were monitored and manually recorded over the 100 min interval at a sampling rate of one per minute in the first 20 minutes and at 10-minute intervals thereafter. Same as Humidity test above, two repeats were performed and recorded with different participants. The ambient carbon dioxide concentration was recorded before each test. The tests were repeated for three different material combinations including cotton, single and double layer of PP with same design.

### **2.3 Particle filtration efficiency tests**

The full-face respirator was tested for its particle filtration efficiency using a *PortaCount*<sup>®</sup> Fit Tester Model 8048 (TSI Incorporated, Shoreview, MN, U.S.) under normal laboratory ventilation and using similar protocols as the ANSI Z88.10-2010 respirator Fit testing methods. Instead of testing on humans for filtration efficiency a manikin was used and tests were performed at different breathing rate equivalent of rest and exercise. However, movement effects conduct by human users are not involved with the manikin setup in this study. The portacount device measures the amount of sodium chloride particles (with concentration of 2,000 to 3,000 particles/cc and count median diameter of ~75nm) that are filtered through the full-face respirator hood from the ambient [9]. The salt particles in the ambient was generated by a TSI Particle Generator Model 8026 (TSI Incorporated, Shoreview, MN, U.S.) which was positioned 1.8 m away from the *PortaCount*<sup>®</sup> Fit Tester. The full-face respirator was placed on a manikin head in order to simulate the user by connected to a breathing simulator and fastened to the manikin in the same manner as that worn in normal use. An opening on the full-face respirator was made to sample the air inside the face shield. A sampling tube was run from this opening to the *PortaCount*<sup>®</sup> Fit Tester as shown in Figure 2.2.

The breathing airflow was simulated by connecting the manikin to a breathing simulator (Michigan Instruments, Kentwood, U.S) which can replicate air coming to and from the human lung with a breathing rate range of 2 to 1,100 bpm at +/- 1 bpm accuracy. In this instance, the breathing simulator was operated only in the inhaling mode since this is the process that allows the particles to filter into the hood. The breathing volume and breathing rate from the simulator were adjusted and controlled using the breathing simulator module. The tests were conducted at flow rates ranging from 6 l/min to 90 l/min (lpm) from the breathing simulator and the filtration efficiency was obtained once the PortaCount® Fit Tester readings were stable. A resting person has a normal minute volume of about 5-8 lpm which increases with exercise to 40-60 lpm during moderate exercise[10]. Fit factor values (ratio of concentration of particles in ambient air to its concentration inside the full-face respirator) were obtained directly from the PortaCount® Fit Tester device which were then converted to filtration efficiency using the equation below.

$$\text{Filtration efficiency} = \left(1 - \frac{1}{\text{FF}}\right) \times 100 \quad (1)$$

Where:

FF(Fit factor) = Concentration of particles in ambient/ in the respirator.

Tests were also performed and repeated for three times with retightening and repositioning using a similar full face respirator made from a single ply of cotton woven fabric for comparison.

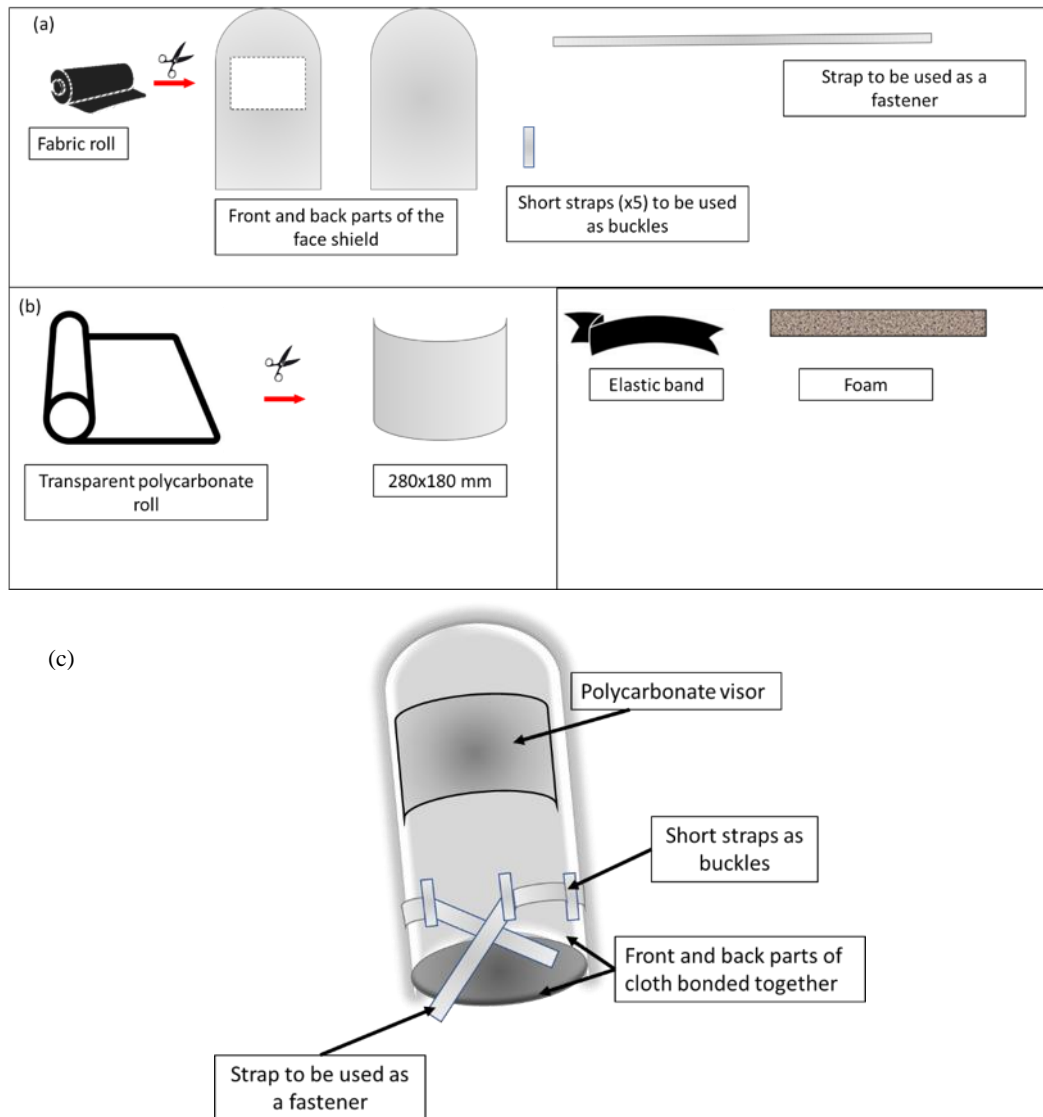


**Figure 2.1** Schematic of fabrication process for the full head face shield

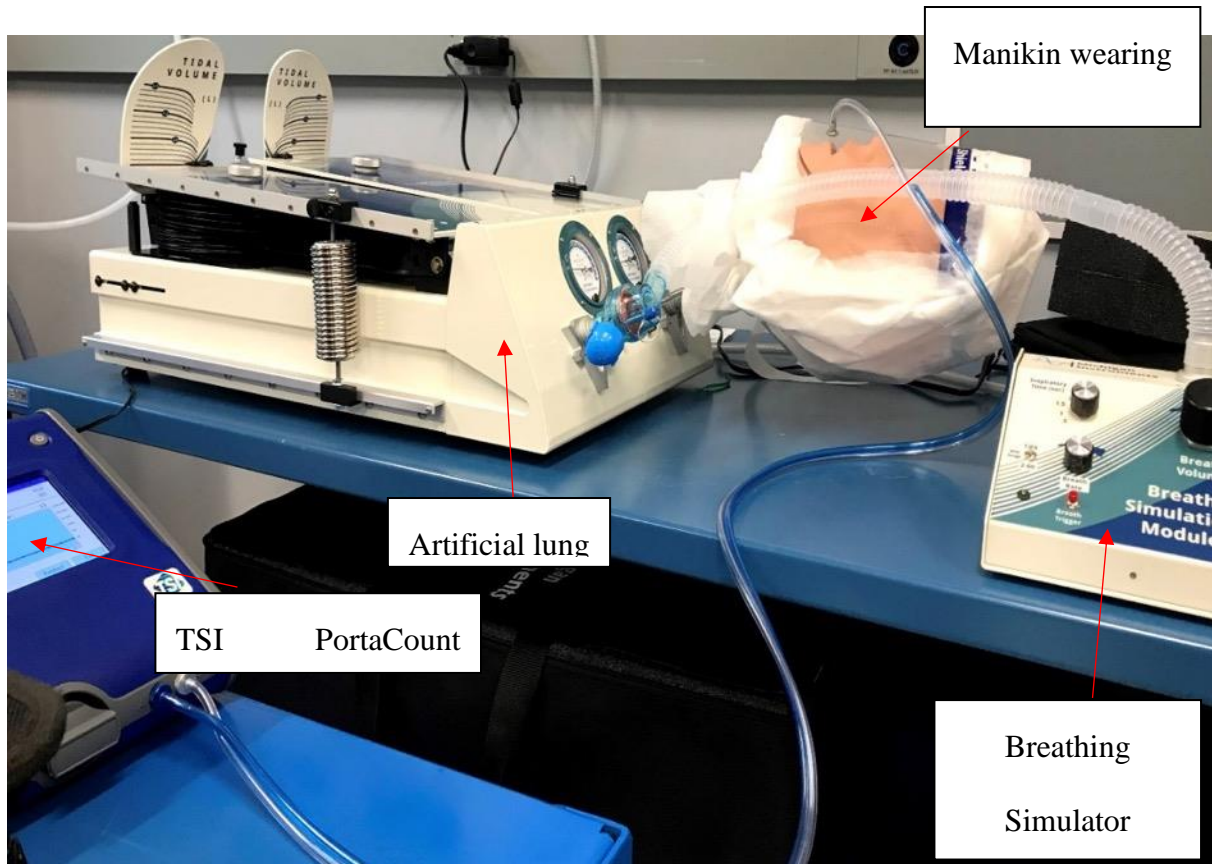


**Figure 2.2** Particle filtration efficiency test setup with breathing simulator

### 3. Results

The change in relative humidity and temperature inside the full-face respirator with time is shown in Figure 2.3. There is a rapid increase in the relative humidity within the first few minutes of wearing the full-face respirator. The relative humidity then stabilizes out after about 10 minutes at 70-80% for the male participant and 50-70% for the female participant. The rate of increase in RH for both the single and double ply full face respirator is almost similar for the male participant; however, the cotton full face respirator showed a much steeper increase but stabilized to about the

same value as the other two full face respirator. There is an increase in the temperature but not as rapidly as the relative humidity. The temperature stabilizes out after about 20 minutes to the range 25-30°C for both the test subjects. A stable value would be reached when there is an equilibrium between the metabolic heat production and heat removal from the respirator.

To evaluate the comfort level for the user, the humidex was calculated as [11]

$$\text{Humidex} = T(^{\circ}\text{C}) + 0.55 \times \left( 6.11 \times e^{5417.75 \times \left( \frac{1}{273.16} - \frac{1}{D} \right)} - 10 \right) \quad (2)$$

Where:

T= Temperature in the respirator

D= Dewpoint in Kelvins in the respirator

and are plotted in Figure 2.4. All three prototype full face respirator show a similar trend of rapid increase in humidex values within the first 20 minutes. Afterwards, the values stabilizes with the ones from the 2 ply full face respirator having the highest humidex values for the male participant and the cotton cloth one for the female participant.

The change in carbon dioxide level (ppm) over the course of using the full-face respirator for 100 minutes is shown in Figure 2.5. Both male and female participants were evaluated and recorded. All the results from male participant are relatively stable for all the respirator configurations below 2000, whereas female participant started with high level of carbon dioxide concentration at initial stage, following by a decrease trend.

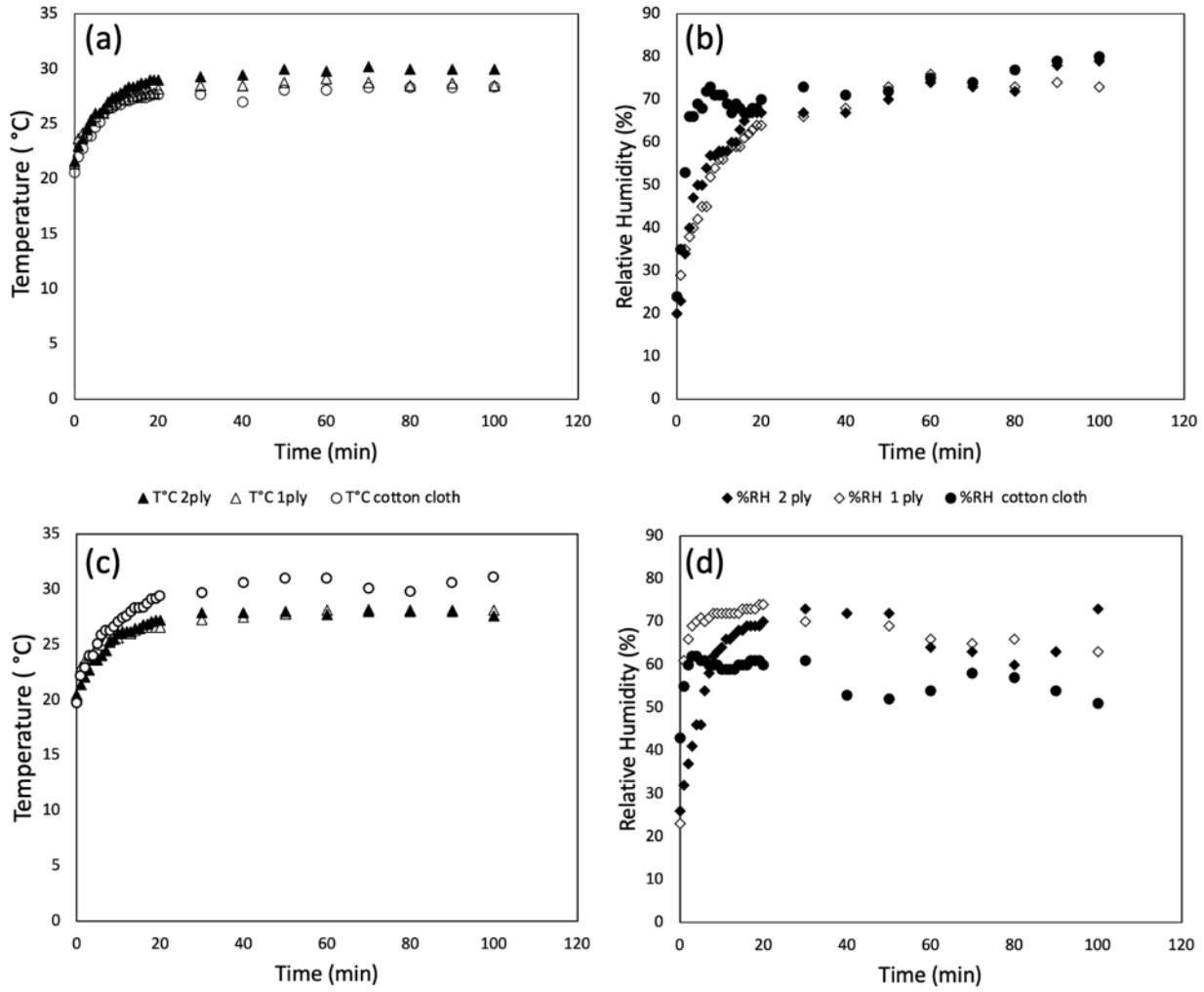


**Figure 2.3** Relative temperature and humidity within the faceshield with time for (a)-(b) male participant and (c)-(d) female participant

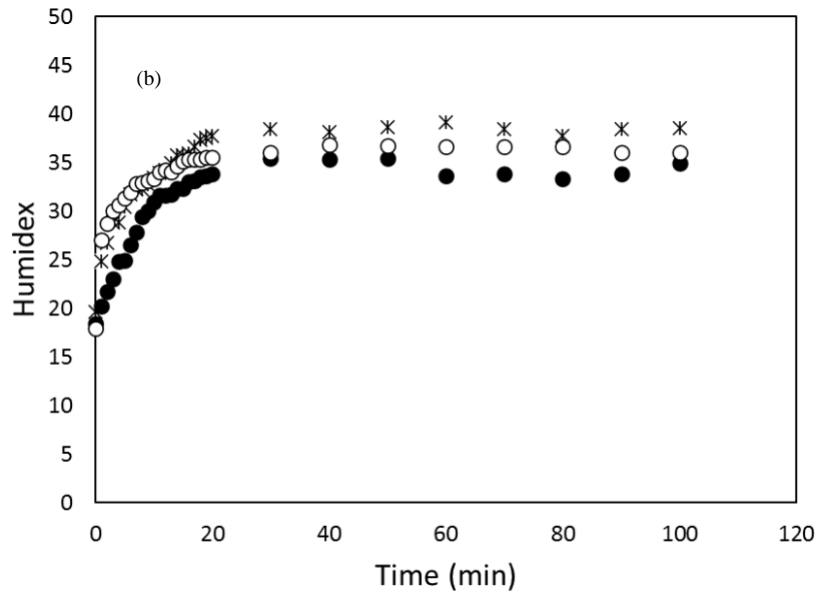
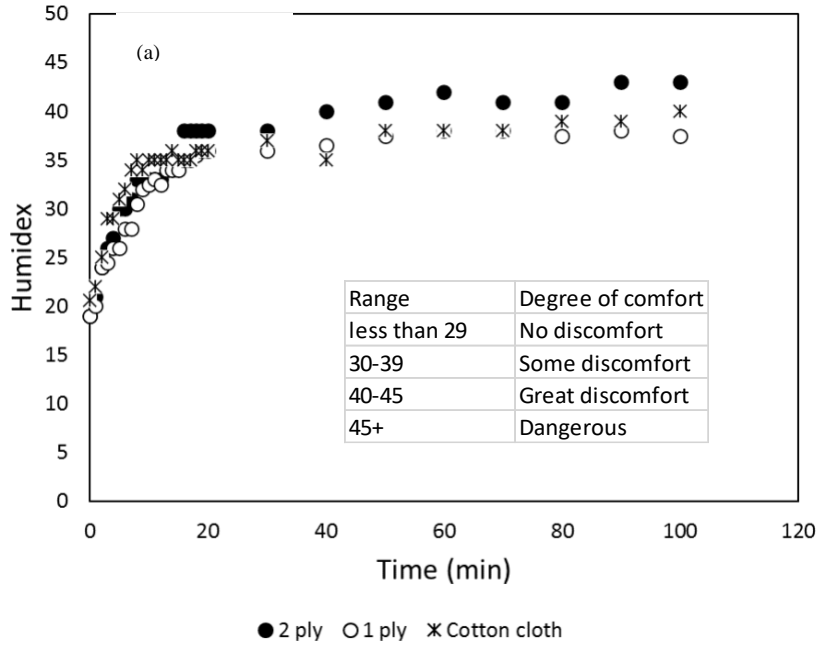


**Figure 2.4** Humidex comfort within the faceshield with time for (a) male participant and (b) female participant

The filtration efficiency results (particle concentration range from 0.01 to  $2.5 \times 10^5$  particles/cm<sup>3</sup> and sizes 0.02 to greater than 1 micrometer) [12] of the three prototype full face respirator at

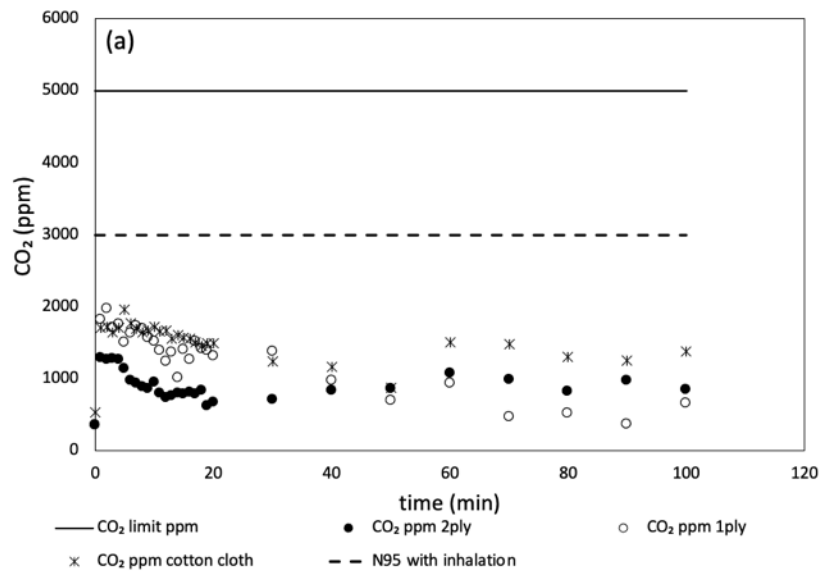
different flow rates are shown in Figure 2.6. Both double ply and single ply full-face respirator shown stable efficiency while all the tests. The double ply full-face respirator has the highest filtration efficiency of 95 to 97% followed by the single ply respirator at 80 to 93% over the range of tested flow rates. There are more fluctuations along efficiency of cloth (woven cotton) full-face respirator with a trend of increasing. It shows a low filtration efficiency at a value around 80%.

#### **4. Discussion**

The trend of relative humidity and temperature inside the full-face respirator changes is similar to the observation of a study carried out on N95 filtering facepiece respirators (FFR) in which the temperature and relative humidity reached a stable value after 10 minutes and 30 minutes respectively [13]. The stable temperature and relative humidity in that study [13] after 1 hour with the participants walking on a treadmill at 5.6 km/h were approximately 33°C and 91%, respectively. The higher values obtained in that study are likely due to the relatively higher physical activity of the participants. The same trend is observed for temperature change after 20 minutes when the temperature in a double ply full-face respirator was slightly higher than that of the single ply one. The differences between the single and double ply face shields are insignificant given the small variations in the ambient conditions and the human participants.

As to the humidex changes which is an important factor of comfort level, despite these small differences, all the prototypes stabilize within the ‘some discomfort’ level [14]. However, the 2 ply full face respirator with the male participant showed an average value within the ‘great discomfort’ levels for the male participant which may have been influenced by changes in ambient conditions as well as their level of hydration during the test. The most desirable design is to achieve a humidex value as low as possible, while having a high filtration efficiency.

Carbon dioxide level is another factor to evaluate the safety and comfort level of respirators as shown in Figure 2.5. It can be observed that the recorded values are significantly below the recommended carbon dioxide limit of 5,000 ppm over an 8-hour workday specified by [15]. Nevertheless, mild high-level cognitive effects have been noted even when the carbon dioxide levels are around 1400 ppm [16]. This shows that the ability of the full-face respirator can expel the carbon dioxide exhaled and maintain the concentration at a lower range is important. It should be noted that these levels are below those within a N95 respirator [17].



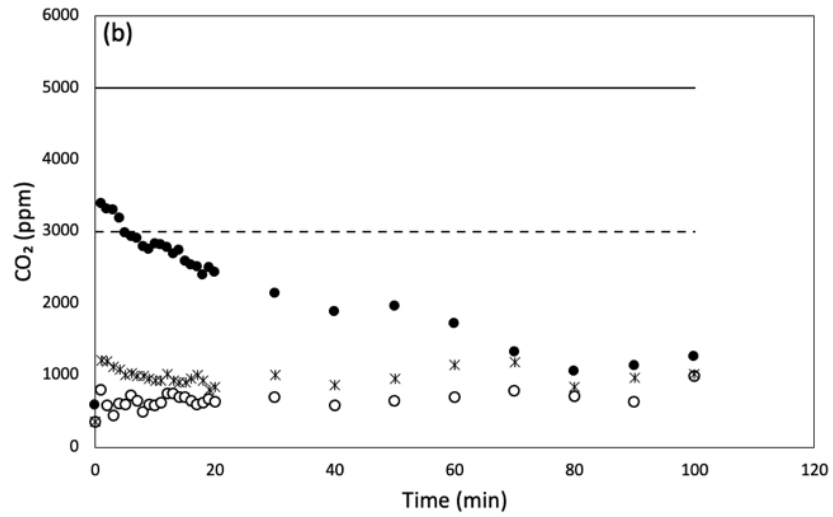


**Figure 2.5** Carbon dioxide level (ppm) within the full-face respirator with time for (a) male participant and (b) female participant.

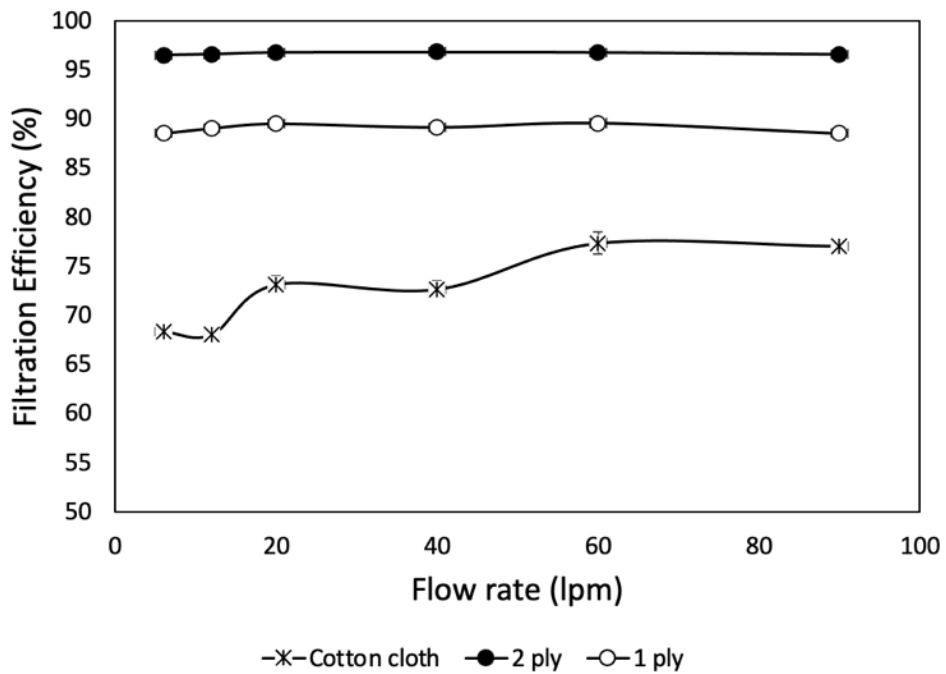


**Figure 2.6** Filtration efficiency of the full-face respirator at different flow rates

For the assessment of filtration performance, the double ply full-face respirator is expected to have the highest filtration efficiency, followed by the single ply respirator since the filtration would be improved by adding another layer of fabric. The superiority of nonwovens in terms of filtration capability can be seen by comparing them with cloth (cotton woven) full face respirators and has been adopted by most N95 and surgical masks [18]. There is an increase in the filtration efficiency for the cloth full face respirator when the flow rate is increased from 6 lpm to 40 lpm as compared to the other two prototypes. This may be due to its material properties which filter air less effectively than the 1 or 2 ply full-face respirator making the filtration efficiency change quicker as breathing rate is increased.

## **5. Conclusions**

A full-face respirator fabricated using only pressure sensitive adhesive (PSA) to bond all the components together has been designed and fabricated. Prototypes fabricated using a single and two plies of nonwoven polypropylene and one ply of woven cotton fabric were tested. Particle filtration efficiency tests were carried out at different flow rates using a breathing simulator and a PortaCount® Fit Tester device. Temperature, humidity and carbon dioxide measurements within the full-face respirator when worn by a male and female participant doing sedentary work were carried out over a continuous period of 100 minutes. The particle filtration efficiency of the double ply full face respirator (averaging 96%) was higher than that of the single ply (averaging 93%) one followed by the one with woven cotton cloth (averaging 75%). Temperature and relative humidity changes of the single and double ply full face respirator were comparable to one another and show a similar trend of a rapid increase from ambient conditions within the first 20 minutes. The

humidex levels within the full face respirator were in the “some discomfort” level while the 2 ply full face respirator showed a “great discomfort” level at extended times. Carbon dioxide levels remained significantly lower than that of the recommended 8 hr exposure limit of 5,000 ppm over the duration of the tests. The results show better performance of carbon dioxide level to that of a standard N95 respirator over the same period of time. Due to the significant performance and ease of manufacturing of the prototype, the full-face respirator has significant potential for manufacture and use by health care workers and the public.

### **ACKNOWLEDGMENTS**

The authors acknowledge funding support from the Ontario Together Fund and the Federal Development (FEDDEV) Agency of Ontario. PRS acknowledges support from the Distinguished Engineering Professor Award from McMaster University.

### **FUNDING STATEMENT**

This research was partially funded through support from the RONCO PPE, Canada.

### **CONTRIBUTION OF AUTHOR**

Rong Wu participated in the fabrication of devices, led the test for humidity and temperature monitor, and also the filtration performance test.

### **DATA AVAILABILITY STATEMENT**

The authors confirm that the data supporting the findings of this study are available within the article [and/or] its supplementary materials.

### **References**

- [1] W. H. Organization. Rational Use of Personal Protective Equipment for Coronavirus Disease 2019 (COVID-19) Interim Guidance 27 [Online] Available: [https://apps.who.int/iris/bitstream/handle/10665/331215/WHO-2019-nCov-IPCPE\\_use-2020.1-eng.pdf](https://apps.who.int/iris/bitstream/handle/10665/331215/WHO-2019-nCov-IPCPE_use-2020.1-eng.pdf)
- [2] T. Burki, "Global shortage of personal protective equipment," *The Lancet Infectious Diseases*, vol. 20, no. 7, pp. 785-786, 2020.
- [3] C. L. Stewart, L. W. Thornblade, D. J. Diamond, Y. Fong, and L. G. Melstrom, "Personal protective equipment and COVID-19: a review for surgeons," *Annals of surgery*, vol. 272, no. 2, pp. e132-e138, 2020.
- [4] R. J. Roberge, "Face shields for infection control: A review," *Journal of occupational and environmental hygiene*, vol. 13, no. 4, pp. 235-242, 2016.
- [5] Z. Jessop *et al.*, "Personal protective equipment for surgeons during COVID-19 pandemic: systematic review of availability, usage and rationing," *Journal of British Surgery*, vol. 107, no. 10, pp. 1262-1280, 2020.
- [6] W. G. Lindsley, J. D. Noti, F. M. Blachere, J. V. Szalajda, and D. H. Beezhold, "Efficacy of face shields against cough aerosol droplets from a cough simulator," *Journal of occupational and environmental hygiene*, vol. 11, no. 8, pp. 509-518, 2014.
- [7] W. G. Lindsley, F. M. Blachere, B. F. Law, D. H. Beezhold, and J. D. Noti, "Efficacy of face masks, neck gaiters and face shields for reducing the expulsion of simulated cough-generated aerosols," *Aerosol Science and Technology*, vol. 55, no. 4, pp. 449-457, 2021.

- [8] V. Arumuru, J. Pasa, and S. S. Samantaray, "Experimental visualization of sneezing and efficacy of face masks and shields," *Physics of Fluids*, vol. 32, no. 11, p. 115129, 2020.
- [9] S. Rengasamy *et al.*, "A comparison of total inward leakage measured using sodium chloride (NaCl) and corn oil aerosol methods for air-purifying respirators," *Journal of occupational and environmental hygiene*, vol. 15, no. 8, pp. 616-627, 2018.
- [10] M. Zuurbier, G. Hoek, P. v. d. Hazel, and B. Brunekreef, "Minute ventilation of cyclists, car and bus passengers: an experimental study," *Environmental health*, vol. 8, no. 1, pp. 1-10, 2009.
- [11] N. Shartova, D. Shaposhnikov, P. Konstantinov, and B. Revich, "Cardiovascular mortality during heat waves in temperate climate: an association with bioclimatic indices," *International Journal of Environmental Health Research*, vol. 28, no. 5, pp. 522-534, 2018.
- [12] T. incorporaed. PORTACOUNT® RESPIRATOR FIT TESTER Manual [Online] Available: <https://www.kenelec.com.au/wp-content/uploads/2022/06/TSI-8040-8048-PortaCount-Respirator-Fit-Tester-Manual-revF-May-2021.pdf>
- [13] R. J. Roberge, J.-H. Kim, and S. Benson, "N95 filtering facepiece respirator deadspace temperature and humidity," *Journal of occupational and environmental hygiene*, vol. 9, no. 3, pp. 166-171, 2012.
- [14] C. C. f. O. H. a. Safety. "Humidex Rating and Work." [https://www.ccohs.ca/oshanswers/phys\\_agents/humidex.html](https://www.ccohs.ca/oshanswers/phys_agents/humidex.html) (accessed Sep 09, 2022).
- [15] O. S. a. H. Administration. "Carbon Dioxide Health Hazard Information Sheet ." [https://www.osha.gov/dts/chemicalsampling/data/CH\\_225400.html](https://www.osha.gov/dts/chemicalsampling/data/CH_225400.html) (accessed Sep 09, 2022).

- [16] B. Du, M. C. Tandoc, M. L. Mack, and J. A. Siegel, "Indoor CO<sub>2</sub> concentrations and cognitive function: a critical review," *Indoor air*, vol. 30, no. 6, pp. 1067-1082, 2020.
- [17] H. Salati, M. Khamooshi, S. Vahaji, F. C. Christo, D. F. Fletcher, and K. Inthavong, "N95 respirator mask breathing leads to excessive carbon dioxide inhalation and reduced heat transfer in a human nasal cavity," *Phys Fluids (1994)*, vol. 33, no. 8, p. 081913, Aug 2021, doi: 10.1063/5.0061574.
- [18] S. N. Rogak, T. A. Sipkens, M. Guan, H. Nikookar, D. Vargas Figueroa, and J. Wang, "Properties of materials considered for improvised masks," *Aerosol Science and Technology*, vol. 55, no. 4, pp. 398-413, 2021.

## **Chapter 3 Efficient, Breathable, and Compostable, Multi-Layer Air Filter Material Prepared from Plant Derived Biopolymers**

Rong Wu<sup>a†</sup>, Sneha Shanbhag<sup>a†</sup>, P.Ravi Selvaganapathy<sup>\*a,b</sup>

<sup>a</sup> Department of Mechanical Engineering, McMaster University, 1280 Main St W, Hamilton L8S 4L8

<sup>b</sup> Department of Biomedical Engineering, McMaster University, 1280 Main St W, Hamilton L8S 4L8

† Denotes equal contributions from these authors.

\* Authors to Whom Correspondence Should Be Addressed.

E-mail: [selvaga@mcmaster.ca](mailto:selvaga@mcmaster.ca)

**Keywords:** Compostable facemask; pleats; zein; plant biopolymer; air filter

**Status: Published**

**Full citation:** Wu, Rong, Sneha Shanbhag, and P. Ravi Selvaganapathy. "Efficient, Breathable, and Compostable Multilayer Air Filter Material Prepared from Plant-Derived Biopolymers." *Membranes* 13.4 (2023): 380.

**Contribution:** This chapter proposed the development of filter material with excellent filtration performance and tolerance to humidity and mechanical handling. Owe to its composability, it led to less environmental impact and pollution compared with current synthetic polymer based filter materials.

**Abstract:**

State-of-art facemasks and respirators are fabricated as single-use devices using microfibrinous polypropylene fabrics which are challenging to be collected and recycled at a community scale. Compostable facemasks and respirators can offer a viable alternative to reducing their environmental impact. In this work, we have developed a compostable air filter produced by electrospinning plant derived protein, zein on a craft paper-based substrate. The electrospun material is tailored to be humidity tolerant and mechanically durable by crosslinking zein with citric acid. The electrospun material demonstrated a high particle filtration efficiency (PFE) of 91.15 % and a high pressure drop (PD) of 191.2 Pa using aerosol particle diameter of  $75 \pm 2$  nm at a face velocity of 10 cm/s. We deployed a pleated structure to reduce the PD or improve breathability of the electrospun material without compromising PFE over short and long duration tests. Over a 1-hour salt loading test, the PD of a single layer pleated filter increased from 28.9 Pa to 39.1 Pa while that of the flat sample increased from 169.3 Pa to 327 Pa. Stacking of pleated layers enhanced PFE while retaining low PD; a 2-layer stack with a pleat width of 5 mm offers a PFE of  $95.4 \pm 0.34\%$  PFE and a low PD of  $75.2 \pm 6.1$  Pa.

## **1. Introduction**

Air pollutants such as particulate matter like black carbon, mineral dust, aerosols, toxic gases, and biological pollutants are increasingly responsible for a range of respiratory diseases. Advanced air filter materials are being developed to target highly efficient removal of a range of particulate matter such as particles with an average diameter of 10 microns, 2.5 microns or 0.3 microns, while also demonstrating low pressure drop for breathability or reduced energy consumption. While the performance of the filtration media and face masks is of utmost importance to protect human health, the SARS-CoV-2 pandemic has also raised much attention to the disposal and environmental implications of air filter media and face masks which are usually single use devices.[1] This in turn has driven much attention to the development of recyclable and biodegradable or compostable air filter materials.

Biodegradable or compostable air filter media and facemasks produced from bio-derived, or waste-derived biopolymers offer a viable alternative to reducing the environmental impact of air filters and facemasks.[2] Air filter media and face masks are often developed as microfibrinous nonwovens from melt-blowing synthetic plastics such as polypropylene. Melt-blown microfibers exposed to an electret process offer high filtration efficiencies for submicron particles while maintaining a low pressure drop.[3] Although, polypropylene can be collected and recycled, reverse supply chains for collecting used filters and facemasks at community scale, separating the filter layers and reprocessing these into functional filters is a challenge. Melt-blowing biopolymers to produce nonwoven filter materials has currently only been feasible with polylactic acid (PLA),[4] a commercially produced synthetic biopolymer that degrades at slow rates under natural conditions.[5] Solution-based processes like electrospinning offer a versatile processing platform

to a wide range of natural or synthetic biopolymers that more readily degrade under natural conditions in soil or water.[2, 6] However, unlike melt-blowing which produces microfibers, electrospinning produces nanofibrous filter mats which have smaller fiber and pore diameters.

Bio-based air filter materials and facemasks need to meet the performance standards for its intended application while being compostable. Several groups have developed electrospun air filter materials using a range of biopolymers such as polylactic acid, proteins such as zein, cellulose acetate, and chitosan.[2] In previously reported studies on electrospun zein air filter materials, the particle filtration efficiencies range from 93 – 99.99 % and the pressure drop ranges between 90 - 175 Pa. However, these studies involved testing the nanofibrous filter materials under lower air flow rates of 2 - 6 cm/s, and their expected pressure drop would exceed the limits required for breathability when extrapolated to air flow velocity of 10 cm/s as required by ASTM standard F3502 for barrier face coverings (facemasks for bioaerosols).[7-9]

Reducing the pressure drop can be achieved via modification to the process parameters to obtain more hierarchical fibrous structures,[10, 11] or by modifying the structure of the electrospun filter through post processing techniques. The former approach requires modification to the electrospinning nozzle to create low and high solution concentration zones, which in turn produce a bimodal distribution in fiber sizes. This approach may be feasible for certain biopolymers and solvent systems. However, the latter approach of post processing such as creating mechanical structures to lower the pressure drop can be applied to any nanofibrous filter mat. To the best of our knowledge, mechanical structuring has not been explored in the context of electrospun air filter materials or facemasks.

In this work, we have developed a compostable air filter material produced by electrospinning plant derived protein, zein on a craft paper-based substrate with high particle filtration efficiency. We assess this filter material for a barrier face covering application or facemasks for bioaerosols as provided in ASTM F3502 standard ( equipment and aerosol used is identical to that required by NIOSH in 42 CFR Part 84 for testing N95 respirators). We examine the effect of concentration of solution and behavior of electrospun zein materials in humidified testing conditions. We also examine approaches to enhance the moisture tolerance and robustness of the electrospun zein filter material. We also investigate mechanical structuring to enhance particle filtration efficiency and reduce pressure drop of nanofibrous filter materials. As such, we report a composite nanofibrous filter design that demonstrates high filtration efficiency and low pressure drop over long durations and under high flow rates that have not been demonstrated before.

## **2. Materials and Methods**

### **2.1 Materials**

Cellulose based Japanese craft tissue paper, Tengujo (13 gsm) was sourced from a craft paper supplier (Japanese Paper Place, Toronto, Canada). Zein from maize (grade Z3625), citric acid (ACS reagent, 95%), sodium hydroxide (ACS reagent, 97%) and anhydrous ethanol (EtOH,  $\geq 99.9\%$ ) were procured from Sigma-Aldrich Inc. Whatman grade 2 filter paper was purchased from Fisher Scientific. Nonwoven meltblown polypropylene fabric supplied by Ronco Canada was used as the polypropylene based filtration material for comparison.

### **2.2 Preparation of electrospinning solution**

Anhydrous ethanol was first diluted to 70% concentration (v/V) using deionized water. Uncrosslinked zein solution of concentrations 25%, 30% and 40% (w/V) were prepared in 70%

ethanol. Crosslinked zein solutions were prepared using an experimental protocol reported elsewhere.[12] Briefly, a citric acid solution of 9% concentration (w/V) and a sodium hydroxide solution with a concentration of 0.125 mg/mL were respectively prepared using 70% ethanol as the solvent. The pH of the citric acid solution was adjusted to 4 by a dropwise addition of sodium hydroxide solution to it while monitoring the pH of the solution using a pH meter (Ohaus, Model number ST2100-F). Zein solution of 50% concentration (w/V) was prepared using the pH 4 citric acid solution, and it was aged for 48 hours prior to preparing crosslinked zein solutions with it. The aged 50% zein solution was then diluted using 70% ethanol to concentration of 25%, 30% and 40% crosslinked zein (w/V). A simplified process describing the preparation of the electrospinning solution is provided in Figure 3.1a.

### **2.3 Preparation of electrospinning substrates**

Tengujo paper (13 gsm) was first flattened using a hot iron to remove creases. Flat sheets of Tengujo paper were cut to a size of 8" x 15". To prepare folded substrates, we first cut strips from a transparent acetate sheet to a width of 1 mm, 5 mm, 10 mm and 20 mm. Tengujo paper was pleated in an accordion format using the acetate strip as a guide to prepare 6 sheets each of 1 mm, 5 mm, 10 mm and 20 mm accordion folds. Further, 3 sheets of each of the pleated widths were stretched out to prepare pre-pleated flat sheets. A schematic of the pleating process is described in Figure 3.1b.

### **2.4 Electrospinning process**

Electrospinning of the zein solution was carried out using 6 parallel nozzles with inner diameter of 0.8 mm with a multinozzle electrospinner/electrosprayer with a drum collector (Inovenso, NE300) as shown in Figure S3.6. A schematic of the electrospinning process is provided in Figure

3.1c. First, we used flat substrates to electrospin uncrosslinked and crosslinked solutions of zein with varying concentrations as described above. All solutions were electrospun on a drum collector at a temperature of 24 °C, relative humidity conditions between 50-60%, distance of 10 cm between the drum and the nozzles, lateral drum displacement of 5.5 cm (side to side) at a speed of 1 cm/s, and a drum speed of 100 rpm. The electrospinning voltage and solution flow rate however was varied with varying concentration. The viscosity was changed significantly with increasing of concentration. Both the voltage and flow rate were adjusted to get the balance for continuous fiber. Table 3.1 summarizes the electrospinning conditions used at various solution concentrations. Each of the various concentrations tested was electrospun at various times of 5, 15 and 25 minutes respectively. Finally, to prepare pleated and pre-pleated electrospun samples, we electrospun 30% crosslinked zein solution onto all pleated tissue papers, while stretching out the folds over the drum, and taping the sides of the substrate down. The pleated samples then used for further testing were prepared by allowing the folds to be regained by the sample (due to spring back) after electrospinning. Similarly, the pre-pleated samples were prepared by stretching out and testing the samples in a flat format.

**Table 3.1** Electrospinning conditions for varying zein concentrations.

Concentration (% w/V)	25 %			30 %			40 %		
Substrate type	Flat			Flat			Flat		
voltage (kV)	21kV			23 kV			25 kV		
flow rate (mL/h)	6			8			10		
Number of nozzles	6			6			6		
Relative Humidity (%)	50-60			50-60			50-60		
Temperature (°C)	24			24			24		
Distance (cm)	10			10			10		
Homogeneity/Lateral distance (cm)	5.5			5.5			5.5		
Homogeneity speed (cm/s)	1			1			1		
Drum speed (rpm)	100			100			100		
Spinning time (min)	5	15	25	5	15	25	5	15	25

## 2.5 Preconditioning under humid conditions

For testing the effect of humidity on the filter efficiency of the filter materials, we exposed a subset of samples of the crosslinked and uncrosslinked electrospun samples to  $85 \pm 5\%$  RH at  $25\text{ }^\circ\text{C}$  for 1 hour using a temperature-humidity/environmental chamber (ESPEC North America Inc., ESL-2CW). Following exposure to the humidified environment, the particle filtration efficiency and pressure drop were tested under identical test conditions as before exposure, which are further detailed in the next section.

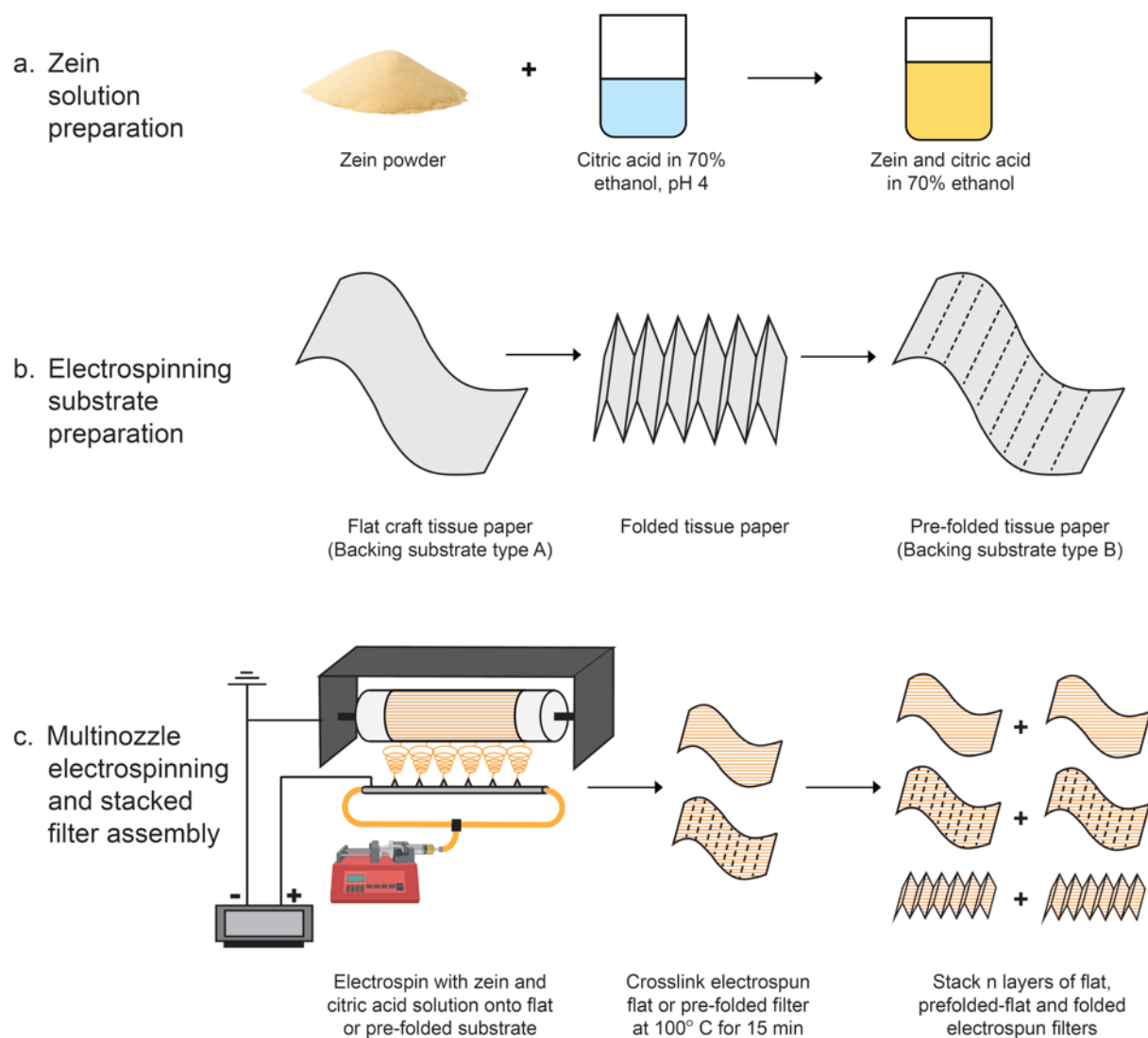


**Figure 3.1** Schematic of process for preparing compostable multi-layer electrospun air filter (a) Zein solution preparation (b)Electrospinning substrate preparation and (c)Multinozzle electrospinning and stacked filter assembly.

## **2.6 Determination of filtration efficiency and pressure drop**

The filtration efficiency of the fabric (test area of 100 cm<sup>2</sup>) was tested using the TSI Certitest automated filter tester 8130A as shown in Figure S3.7 using a sodium chloride aerosol with a count median particle diameter of  $75 \pm 2$  nm (corresponds to 260 nm mass median diameter) at a flow rate of 60 lpm or a face velocity of 10 cm/s as described in the ASTM F3502 standard for testing the particle filtration efficiency and pressure drop of the samples. Finally, we also conducted a salt loading test using above mentioned airflow conditions where the filtration efficiency and pressure drop profile for unconditioned flat, pleated, and pre-pleated samples was monitored as the sample was continuously exposed to an aerosol concentration of 20 mg/m<sup>3</sup> for a duration of 1 hour.

## **2.7 Mechanical folding**

Electrospun filter samples based on the selected configurations were exposed to mechanical handling and then characterized again for their performance in terms of filtration efficiency and pressure drop. To mimic mechanical handling during use, we manually folded the electrospun filter repeatedly for at least 4 times, and then unfolded it prior to taking a measurement and studied the degree of detachment of the fibers after mechanical handling.

## **2.8 Biodegradability**

Biodegradability tests were conducted in an aerobic soil compost mixture and were carried out at  $58 \pm 2^\circ\text{C}$  (ASTM 5338), over a period of 28 days. Briefly, squares (5 cm x 5 cm) of Tengujo tissue paper effectively weighing 0.72 g were distributed in 240 g of moist compost. Similarly, tissue

paper squares with a crosslinked electrospun zein coating with a total weight of 0.82 g was distributed between layers of 240 g of moist compost. Finally, similar size squares of Whatman Grade 2 filter paper weighing 1 g were used as a cellulosic standard material and were distributed between several layers of 240 g of moist compost. In each case, consecutive layers of compost and few squares of the respective paper were spread out in a sealable glass container. A few drops of water were added to ensure the contents remained moist. The container was then left open with gap to aerate the sample and placed in an oven maintained at  $58 \pm 2^\circ\text{C}$ . For each sample type, we had 2 containers containing the respective sample. The disintegration of the samples was observed at the end of every week by extracting 2 squares of each paper/filter type. Soil was brushed off gently from the extracted paper samples and they were gently washed with water and dried for 2 hours in an oven at  $90^\circ\text{C}$ . Photographs of the clean samples were taken to demonstrate the degradation of the samples under composting conditions.

## **2.9 Surface characterization**

We collected scanning electron microscopy (SEM) images to investigate the surface and fiber morphology of the electrospun samples using a TESCAN VEGA -II LSU SEM. Sections (0.5cm x 0.5cm) of electrospun fabric samples around the central area were coated with 5-10 nm layer of gold using a sputter coater to improve the surface conductivity and SEM images were collected at 20 kV in the secondary electron imaging mode. SEM images were collected for electrospun samples for each concentration condition for crosslinked and uncrosslinked samples. Additionally, SEM images were also collected after before and after exposing the electrospun samples to high humidity, mechanical handling and salt loading tests.

### 3. Results and Discussion

#### 3.1 Morphology of the composite zein filter and filtration performance

We characterized the morphologies of electrospun zein fibers prepared from 25 % , 30% and 40 % (w/V) of zein solutions respectively using SEM. The distribution of the fiber diameter of zein fibers was obtained from the SEM images. As shown in Figure 3.2, the fiber diameters and structures are significantly different for various concentrations. It can be seen from Figure 3.2a that the fibers from 25% concentration of zein solution consist of ultrafine fibers with a ‘beads on string’ structure, whereas bead-free fibers were obtained from 30% and 40% concentration of zein solution. By comparison between Figure 3.2b and c, ribbon-like, wide, and flat zein fibrous structures can be found in the SEM of 40 % solution concentration caused by the high volatility of ethanol that produces a skin on the jets of the zein solution as has been described in previous studies.[13, 14] Fiber diameter distributions for the various concentrations studied are illustrated in Figures 3.2d-f. The average fiber diameters for the 25%, 30% and 40% solutions are 0.15 $\mu\text{m}$ , 0.30 $\mu\text{m}$ , and 0.34 $\mu\text{m}$ , respectively. For the formation of fibers , a minimum concentration of solution needs to be satisfied. In the previous studies, a mixture of beads and fibers is obtained at low solution concentration. With increasing solution concentration, the shape of the beads on the fibers change from spherical to spindle-like, and finally due to the higher viscosity resistance of solution uniform fibers with increased diameters are formed.[15] However, formation of continuous fibers is unstable at high concentrations because of the difficulty to maintain the flow of the viscous solution at the needle tip, which would also lead to formation of larger fibers.[16] From SEM images and fiber diameter distribution, 30 % of zein solution produced the most stable and continuous fiber for composite filter based on the balance of solution viscosity and

electrospinning parameters. Our tested concentration range is similar to previous reports of zein based air filters.[8, 9, 11]

To evaluate the structural advantages of fibers prepared from various solution concentrations, we investigated the air filtration performance of composite zein filters with different duration of electrospinning time. Both particulate filtration efficiency (PFE) and pressure drop (PD) were characterized as shown in Figure 3.2g-i. Notably, the PFE and PD of the Tengujo tissue paper substrate is  $0.77 \pm 0.13\%$  and  $2.1 \pm 0.4$  Pa, indicating that the increase in PFE and PD should be mainly attributed to electrospun fibers. The SEM image of substrate was shown in Figure S1a. At the lowest spinning time of 5 minutes, the filter produced from 40% zein presents the lowest PD ( $18.2 \pm 0.4$  Pa) but also the lowest PFE ( $16.97 \pm 0.41 \%$ ) with flow rate at 85 lpm. In contrast, the thinner nanofiber filter from 30 % zein offers a higher PFE ( $30.73 \pm 0.52 \%$ ), but also offers a higher airflow resistance rendering a larger pressure drop ( $23.1 \pm 0.6$  Pa). The 25 % zein solution produced the finest fibers, with a bead on string structure but offers a slightly lower PFE ( $25.89 \pm 0.77 \%$ ) and PD ( $19.2 \pm 0.4$  Pa) probably because of the incomplete or nonuniform surface coverage for the 5 minutes sample, resulting from a smaller Taylor cone. Interestingly, filtration efficiency of filters prepared with 30 % zein spun for 25 minutes was 91.15% which is the best among all three concentrations but its pressure drop was as high as 192.2 Pa. The fiber sizes of the 30 % zein solution appear to favor the interception of the salt aerosol particles (0.075  $\mu\text{m}$  count median particle size) used in PFE tests resulting in the high removal efficiency.[9] Due to its higher filtration efficiency and absence of beaded structures, the 30 % zein solution was selected in following experiments and further analysis.

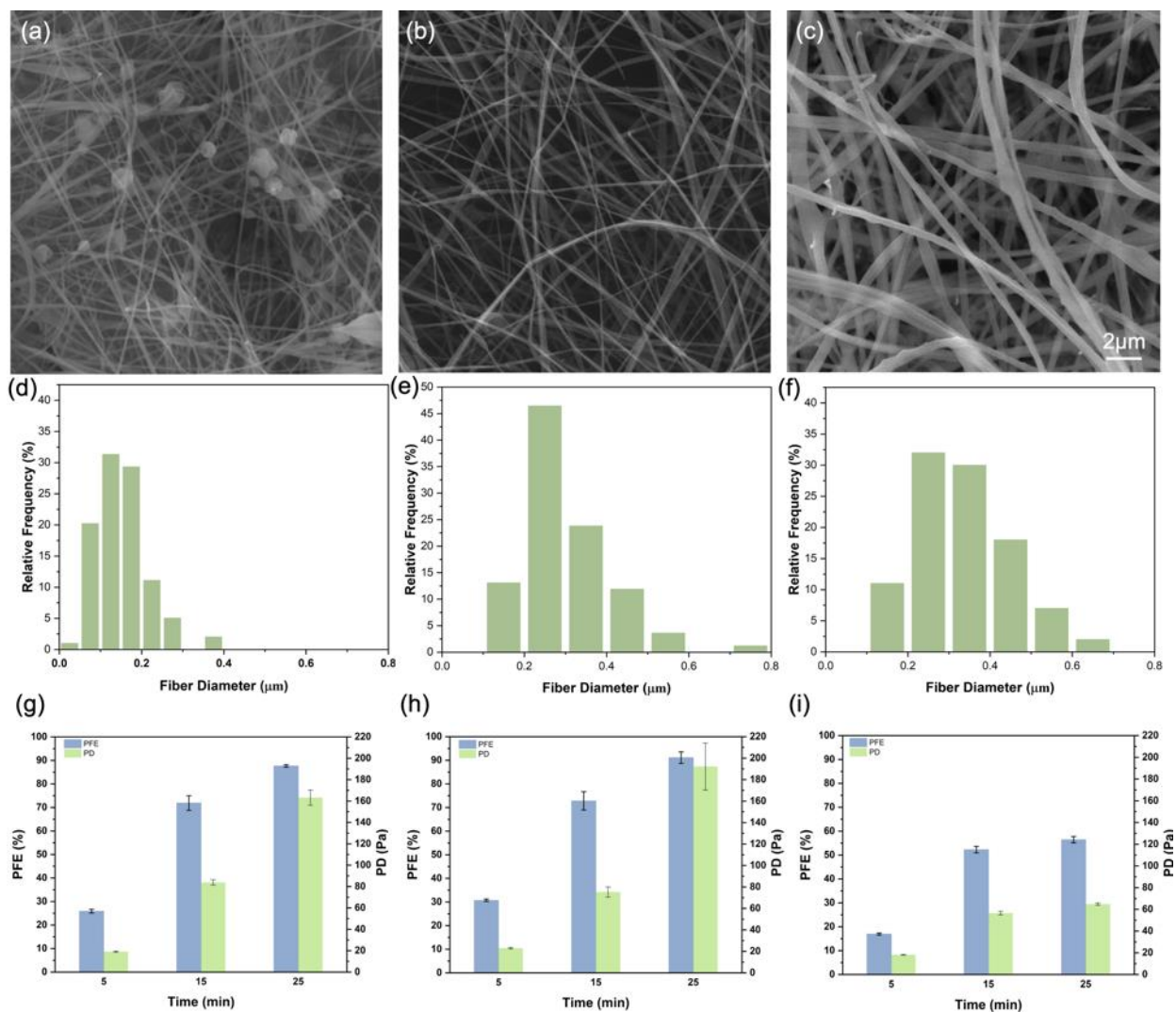


**Figure 3.2** SEM of (a) 25 %, (b) 30 %, (c) 40 % fibers under magnification of 8000x and fiber diameters of (d) 25 %, (e) 30 %, (f) 40 % of crosslinked zein solution; Air filtration including PFE and PD performance of (g) 25 %, (h) 30 %, (i) 40 % with three different electrospinning time from 5 to 25 minutes.

## **3.2 Effect of crosslinking**

### **3.2.1 Morphology and air filtration performance**

The electrospun fibers of crosslinked solution and uncrosslinked solution were characterized under SEM as shown in Figures 3a and b under identical magnification. Both conditions produce smooth and continuous fiber by electrospinning effectively. The average diameter of crosslinked fiber is higher than uncrosslinked fiber, which is  $0.30\mu\text{m}$  and  $0.16\mu\text{m}$ , respectively in Figures 3.3e - f. As reported previously, 9% citric acid was used as crosslinker since it shows remarkable improvement of multiple properties as crosslinker for high concentration protein solution from previous studies.[17] During the crosslinking process, the reaction between an amine group of zein and the carboxylic acids group in citric acid result in amido linkages which might lead to a slightly larger fiber diameter compared with uncrosslinked fiber.[18] The air filtration performance was also tested for both crosslinked and uncrosslinked 25-minute electrospun filter. Uncrosslinked filter shows similar PFE at  $91.46 \pm 2.31\%$  with crosslinked filter at  $91.14 \pm 1.24\%$ , but slightly higher PD at  $189.2 \pm 18.4\text{ Pa}$  compared with  $181.3 \pm 21.9\text{ Pa}$  for crosslinked filter. The lower fiber density and decrease of the air resistance may be related to the increasing diameter of fibers of crosslinked filter.[19] The performance of both crosslinked and uncrosslinked zein is similar as they both possess various functional groups that interact with a range of particulate pollutants and enable the purification of the air.[13, 20, 21] Although uncrosslinked zein offers excellent performance of air filtration, crosslinking process improved other properties which will be discussed in next sections.

### **3.2.2 Effect of humidity on filtration performance**

The cross-linking with citric acid also affected the surface morphology of zein-based nanofibers under high relative humidity (RH 85%). The stability of filter under high humidity was evaluated

by SEM and air filtration performance for both PFE and PD with 0, 30, and 60 minutes of conditioning under high humidity conditions in Figure 3.3c-d. The fibrous structure of uncrosslinked filter was destroyed with significant swelling and fusion of fibers after 30 minutes, and cracks were visible over the entire area (Figure S3.1b), indicating that the pure zein nanofiber materials had a poor moisture resistance under high humidity for long time duration. The filtration performance decreased to  $79.24 \pm 5.35$  % after 30 minutes and  $59.75 \pm 6.22$  % after 60 minutes exposure. The PD showed a similar trend and dropped to  $136.4 \pm 19.4$  Pa at 30 minutes and  $92.9 \pm 15.3$  Pa at 60 minutes. The dramatic drop of PFE and PD is mainly attributed to the crack formation in the filter surface, the remaining function as air filter being provided by some portions of the swollen electrospun fibers. Although previous work showed good stability of uncrosslinked zein fiber under humidified conditions (10 s exposure during testing only),[22] our results demonstrate that uncrosslinked zein layer cannot resist high relative humidity as would be experienced in the enclosed region of the facemask when a person is wearing it. In contrast, crosslinked zein retained the fibrous shape as illustrated in Figure 3.3d indicates that crosslinking with citric acid improved the stability of zein nanofibers under humidified environment. The amido linkages formed during crosslinking improved the moisture tolerance of the crosslinked samples.[17]

As shown in Figures 3.4a-b, there is a slight reduction of PFE to  $89.42 \pm 2.76$  % at 30 minutes and  $87.85 \pm 4.02$  % after 60 minutes of exposure, and PD increased to  $183.6 \pm 19.0$  Pa and  $184.2 \pm 17.8$  Pa respectively. The minor loss in performance is expected to be a result of slight swelling of the zein fiber even after crosslinking process. However, the significantly lower degree of swelling resulting from the crosslinking process may have resulted in preventing the formation of

cracks on the crosslinked filter surface.[17] As such, a filter material prepared with crosslinked zein is amenable for air filtration applications where exposure to higher humidity conditions is expected. The degree of crosslinking of zein solution can be optimized to ensure long duration performance under humid conditions.

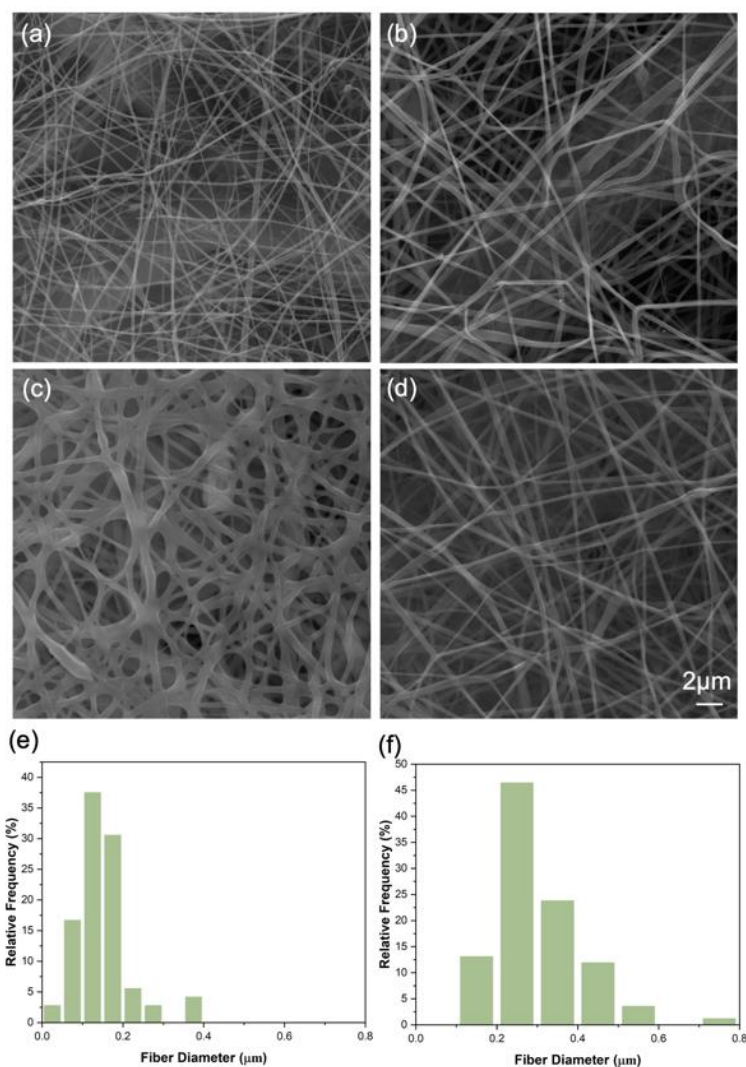


**Figure 3.3** (a) SEM uncrosslinked zein fiber; (b) SEM of crosslinked zein fibers; (c) SEM of uncrosslinked zein fiber exposed to moisture for 60 minutes; (d) SEM of crosslinked zein fiber

exposed to moisture for 60 minutes exposed to moisture; (magnification 8000x applied under SEM) (e) uncrosslinked zein fiber diameter distribution; (f) crosslinked zein fiber diameter distribution.

### **3.2.3 Mechanical handling stability**

The poor mechanical performance of nanofibrous electrospun filter materials limits its practical application as an air filter. To validate the robust mechanical handling of zein fiber fabricated in this work, both uncrosslinked and crosslinked zein filter has been tested by folding 4-5 time per test manually and the results of PFE and PD are shown in Figure 3.4c-d. PFE of crosslinked fabric remained stable indicating the robustness and durability of the crosslinked filter material. In contrast, the PFE of uncrosslinked zein layer decreased continuously with increasing number of folding. The value of PD shows similar tendency, with minor changes in the crosslinked zein, and dramatical drop of uncrosslinked fabric. The slight increase observed in the pressure drop values of the crosslinked sample is expected to have been caused by accumulation of ultra-fine particles with repeated testing on the same sample. We expect two factors to influence the performance of the filter material after mechanical handling; the first is bonding or attachment between zein layer and the paper substrate, and the second is the mechanical property of zein fibers. We observed that the crosslinked fiber did not detach from the paper substrate easily after exposing to repeated folding and testing suggesting that the crosslinking process not only formed linkages between the zein fibers but also with the paper substrate, thereby enhancing its mechanical stability. Additionally, the formation of amido linkage is also expected to improve the tensile strength of the crosslinked zein fibers.[17, 23]

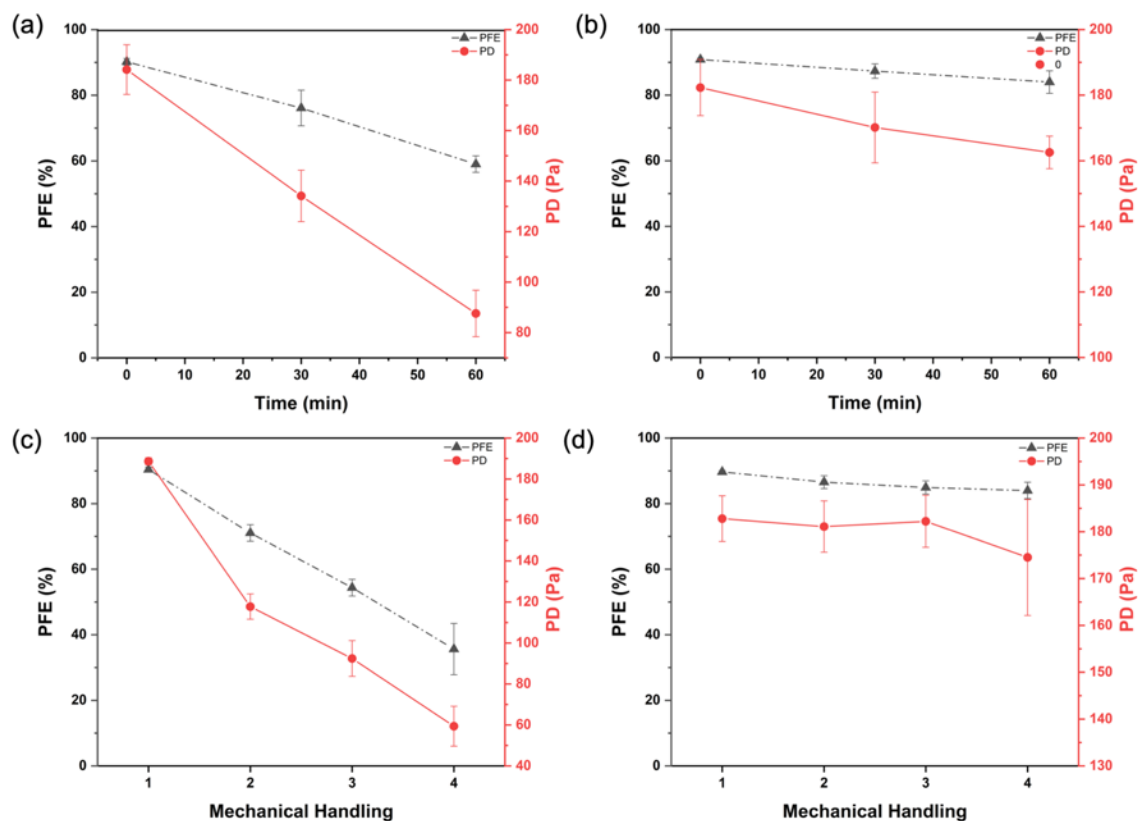


**Figure 3.4** PFE and PD of a) uncrosslinked zein filter with different time of conditioning; (b) crosslinked zein filter with different time of conditioning; (c) uncrosslinked; and (d) crosslinked zein filter after mechanical handling.

### 3.3 Air filtration performance of pleated electrospun filter

To improve filtration performance, we applied a pleated filter format as previously investigated in cartridge air filters[24] to facemasks or respirators. We investigated the effect of pleating by preparing pleated electrospun filters with varying pleat widths of 1, 5, 10 and 20 mm using crosslinked 30% zein filter material. The filtration efficiency and pressure drop observed for these are illustrated in Figures S3.2. The PFE is 88.48%, 84.26%, 82.76% and 78.43%, and PD is 138.9

Pa, 34.1 Pa, 36.7 Pa and 36.1 Pa, respectively for 1,5,10 and 20 mm pleat width filters. Size of folds smaller than 5 mm is not favourable for lowering air resistance likely because of relatively small increase of surface area and smaller effect on the flow profile of the aerosol. Pleat size with 5 mm was found to provide the best performance and utilized for further investigation. Although the samples with 10 mm and 20 mm pleats offered improved breathability over the flat sample, their PD values are still slightly higher than those of the 5 mm pleats. Preventing the larger pleats from collapsing onto one another and retaining the desired triangle pleating shape during testing was challenging, and may have influenced our observed results for larger size pleats. Therefore, the 5mm pleat size was used for investigating the effect of stacking layers of pleated filters.

We also find the PFE of pleated samples are slightly lower than that of their flat counterparts by 6.9% from 91.15% to 84.26% for the 5 mm pleat width sample. We expect that the pleat/crease lines influence the flatness of paper substrate while electrospinning leading to a gradation of fiber coverage along the pleat/crease line. Additionally, PD significantly decreased by 82.3% from 192.2 Pa of flat sample to 34.1 Pa of the pleated sample. The PD across a pleated filter material can be attributed to the PD caused by the filter fibers and that offered by the structure geometry.[25] By incorporating the pleated structure, the total filtration surface area increases, and the face velocity effectively decreases. The pleated sample area is 2.4 times higher than that of the flat sample which partially contributes to lowering the PD. The gradation of fiber coverage between the body and crease lines (trough and peak of accordion fold) on the pleated sample and the air flow profile (Figure S3.1c) may also play a role in lowering the resistance against aerosol flow and pressure drop. We expect that the aerosol flow tends to penetrate the pleats through the weak or thin wall of filter materials where the nanofiber coverage and airflow resistance is low.[26] Our results suggest that pleats are advantageous to lower the pressure drop from the dense nanofibrous.

Despite the high removal efficiency at 91.15% achieved by electrospun zein filter materials, the PD still high at 191.2 Pa. The excellent breathability from pleated zein sample indicates that introducing folded structures is favorable to lower overall airflow resistance while maintaining a high PFE. In addition, face velocity was considered when different filters were evaluated since the PFE and PD would be both influenced at higher face velocity.[27] Both parameters were tested under four different face velocities from 2 to 14 cm/s, as show in Figure S3.3d. The filtration efficiency remained around 95% when the face velocity increased, indicating the PFE remained consistent over a wide range of air flow velocity to support daily usage. Meanwhile, the PD of the tested composite filter linearly increased with the face velocity, from 18.4 Pa to 106.2 Pa.

### **3.4 Stacking of electrospun zein filters**

The improvement in the filtration efficiency and air flow resistance of the multilayered composite filter with flat, pre-pleated and pleated configuration is summarized in Figure 3.5a. All three configurations of zein filter have excellent filtration function with over 99% for multi-layer combinations. For flat and pre-pleated structures, the PFE is even over 99.9%, with extremely high PD at 1219.1 Pa and 591.0 Pa for five-layer stack. Although, the PD linearly increases with number of layers for all three structures, we observe that the pleated stacks have the lowest PD for any number of layers. The increment of PFE is smallest and its rate of increase with layers is lowest in pleated samples due to the high surface area. We observe that despite the stacking of layers, the PD of pleated stacks is only 1/5 that of flat filter stacks. Specifically, a 2-layer pleated stack offers a PFE of 95.4% and a PD of under 100 Pa, while a 2-layer flat stack offers a PFE exceeding 99% and PD of nearly 500 Pa. Our findings indicates that the pleated structure is beneficial in lowering PD of the electrospun samples even in a multilayer stack. Further, this composite pleated stack

meets requirements of a level 1 barrier face covering(20% PFE, 149 Pa PD) as well as may be suitable for creating an N95 respirator.

To compare the filtration performance of the filter material in this work with previous studies, the quality factor (QF, unit: Pa<sup>-1</sup>) is calculated based on the equation below:

$$QF = \frac{-\ln(1 - \eta)}{\Delta P}$$

Where  $\eta$  is particle removal efficiency,  $\Delta P$  is pressure drop of the air filter.

QF indicates the overall performance of filtration based on PFE and PD. a comparison of filtration efficiency with other air filters was summarized in Figure 3.6a. Although the testing parameters such as particle size, flow rate etc. varied in all those studies, our testing environment followed the ASTM F3502 standard which is more conservative. Even based the extremely high face velocity data at 14 cm/s (numbering in the x-axis data labels indicates face velocity in cm/s), QF of this work is higher than most of other previous studies. This further exhibit the comprehensive air filtration performance with high PFE and low PD producing by nanofibers and folding structures.

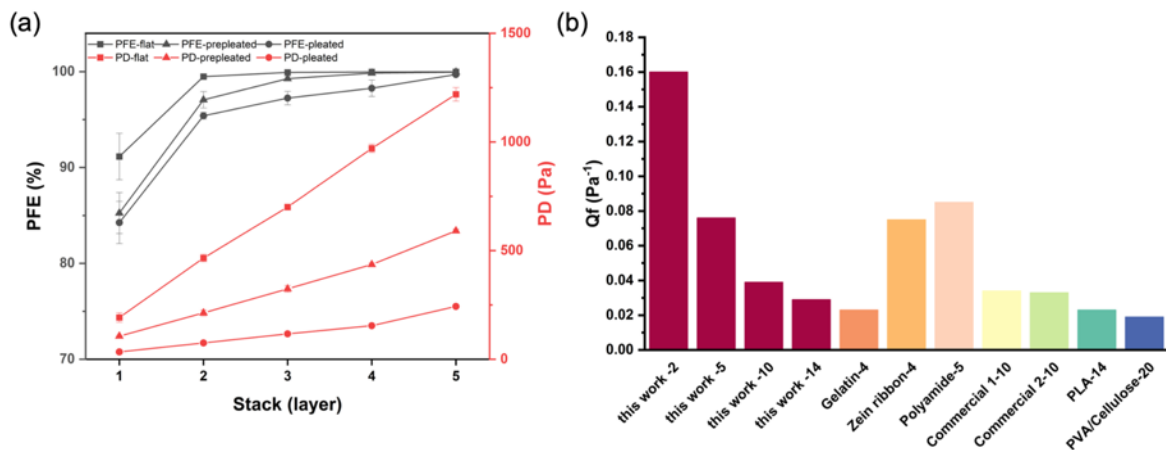


**Figure 3.5** (a) Stacking study of zein filter with flat, pre-pleated and pleated surface. (b) Comparison of quality factors (Qf) between this work with different flow rate and previous studies of synthetic polymer-based as well as natural polymer-based air filters [8, 28-31] The digit after the hyphen on data labels indicates the flow rate in cm/s used in these studies.

### **3.5 Extended filtration performance of composite zein filter**

To evaluate the filtration performance and the air flow resistance of the pleated air filter made of zein with different structures over longer duration of time, we conducted a 1-hour loading test for removing ultrafine salt particles. As shown in Figure 6a, PFE of most of filters are over 99% after long time exposure except pleated one-layer zein filter. The PFE of single layer pleated filter increased by 8.31 % from 87.11% after one hour of testing, whereas that of the flat sample increased by 7.04% from 92.86 % and the pre-pleated by 15.30% from 83.69% respectively. Interestingly, the pre-folded sample shows the highest increase, likely due to particles being trapped and attracted to open areas for aggregation, thus reducing the effect of inhomogeneous coverage. After the large open areas on pre-pleated structures are filled with fine particles, mechanical filtration dominates the loading process, and the efficiency continues to increase further. The advantage of the folded structure is more obvious in the pressure drop performance. After 1-hour loading test, the PD increased from 28.9 Pa to 39.1 Pa for the pleated sample, from 169.3 Pa to 327 Pa for the flat sample and from 103.2 Pa to 334.7 Pa for the pre-folded sample. The advantage of the pleating structure is further evident in the PD profiles for the pre-pleated and flat samples which despite their initial differences, start to perform similarly as they get loading and saturated with salt particles, and offer a higher resistance to air flow. Pleated structures therefore help lower the magnitude and the rate of increase in pressure drop during particle loading.

This reflects that the combination of nanofiber layer and pleating structures helps to achieve the improvement of ultrafine particle efficiency without excessive increase in airflow resistance in both short- and long-term use. Further, the PD increments of 10.2 Pa and 24.7 Pa for single- and 2-layer pleated stacks over the 1-hour loading test were almost linear with the number of layers. Additionally, 1-hour loading test was also performed on commercial Polypropylene (PP) filter layer to compare between flat and pleated structure and the results presented in Figure 6b. Pleats on the PP filter showed a significant improvement for both PFE and PD. The resistance was reduced by 78.6%, while the PFE was even up to 99.67% after loading tests. Therefore, the combination of nano-sized fibers and millimeter-scaled pleats is not dependent on the material or fiber processing method and could be universally applied to other polymer filters used in face masks.

To further interpret the effect of pleated filter structure, the distribution of particles after long-term testing was also investigated by SEM images captured from different filters. From the SEM results of pleated filter on three different positions: peak, sidewall, and trough (Figure 6c-h), the particles tended to predominantly accumulate on the peaks and troughs for both top and bottom of top layer filters. With a large height to width ratio of pleat structure and small pleat pitch, the dust particles are easily deposit in the trough of the pleat, and reduce the effective filtration area of the filter media which will contribute to the increase of pressure drop.[32] Based on SEM images, we observe slightly more particles on the peak area compared with the trough area which is different from micron size particles which deposit largely in the peak angle or trench region.[33] First, unlike larger microscopic particles that have considerable inertia and follow the centreline of the pleat, ultrafine particles utilized in our study likely follow the streamlines and can settle at the peak and throughout the pleat length.[26] Secondly, triangular shaped pleats have been shown to have

less pronounced settling in the trench due to the milder turn at the entrance of air flow at the pleat inlet. This geometry prevent the formation of ‘dead zone’ to some extent with relatively uniform distribution of air flow for the pleat peak and bottom.[26, 34] Further, based on the SEM images, the sidewalls of the pleats capture only a small number of particles leaving a considerable filtration area available even after long-term testing, indicating the pleated zein filter is long-lasting with stable air filtration performance. This likely also contributes to the low resistance of pleated filters during long term tests. As indicated by the SEM images, the upper filter layer performs most of the particle filtration, and bottom layer has almost clean and available filtration area even after one hour of continuous testing. In contrast, considerable amount of particle deposition and blockage of open surface area on flat and pre-pleated air filters (Figure S3.4) results in dramatically high air resistance.

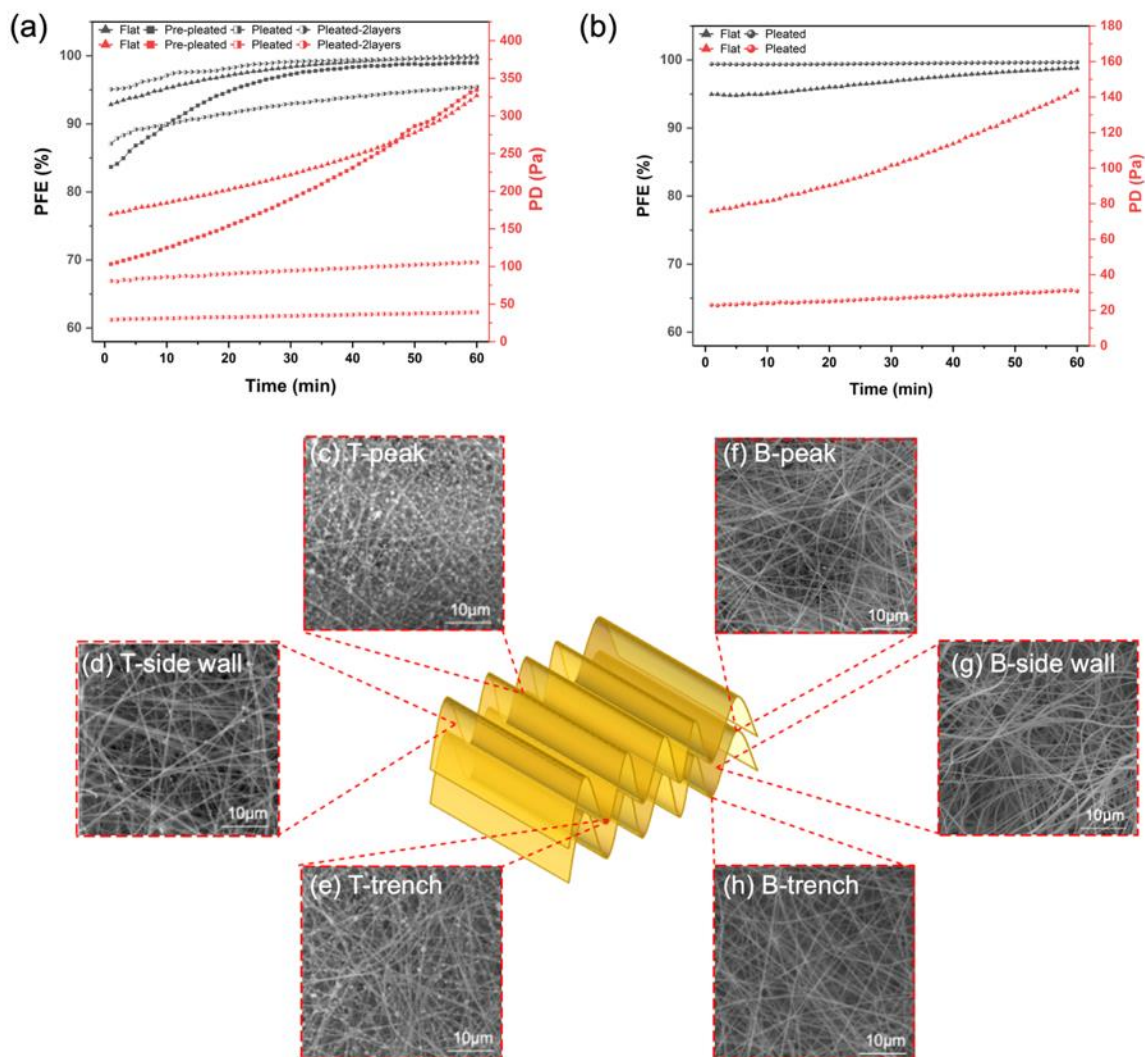


**Figure 3.6** (a) air filtration performance of 60-minute loading test of flat, pre-pleated, and pleated zein filter; (b) air filtration performance of 60-minute loading test of flat and pleated commercial Polypropylene mask filter; Schematic and SEM image of (c) peak, (d) side wall, and (e) trench of top pleated filter; (f) peak, (g) side wall, and (h) trench of bottom pleated filter.

### 3.6 Biodegradability

The zein composite filter with desired filtration efficiency in this study is made entirely of biodegradable, plant-derived materials including the paper substrate. Composted soil degradation

was selected to verify the biodegradability/compostability of zein air filter. Both zein filter and commercial cellulose filter paper were buried in the composting condition at  $58 \pm 2^\circ\text{C}$  according to ASTM standard D5338[25]. It has been found that the zein filter was fully decomposed in composting soil within 4 weeks by microorganisms as shown in Figure 3.7, while a small amount of residue remained in the cellulose filter material. Therefore, the zein composite filter has an excellent biodegradability and provides environmental-friendly solution to the disposal of waste filters.

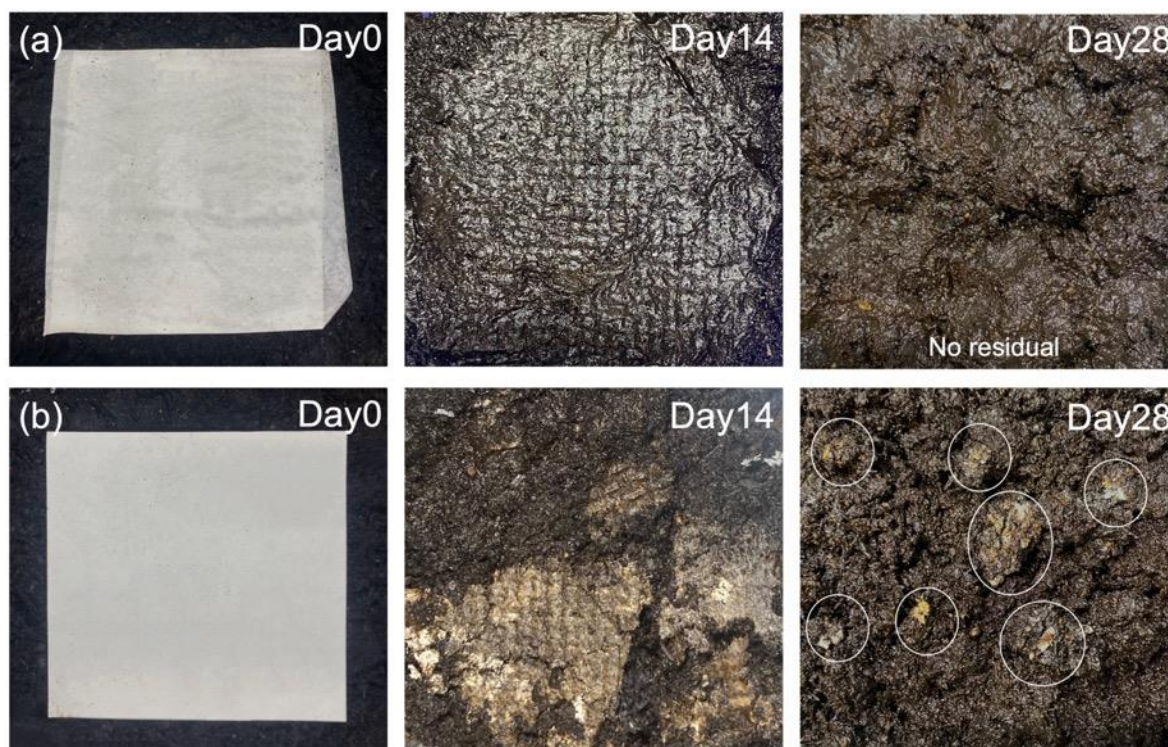


**Figure 3.7** Biodegradability of the developed composite zein filter (a) Zein filter degradation with 28 days (b) Cellulose filter paper degradation with 28 days.

#### 4. Conclusions

In this work, we have developed a compostable air filter material produced by electrospinning plant derived protein, zein on a craft paper-based substrate. The electrospun material is tailored to be humidity tolerant by crosslinking zein with citric acid and this in turn also enhances the mechanical durability of the filter material. The electrospun material inherently demonstrates a high PFE and a nominally high PD. We deployed a pleated structure to reduce the PD of the electrospun material and demonstrate that stacking several layers of pleated electrospun sheets can offer a simple solution in developing a composite nanofibrous filter with high PFE of  $95.4 \pm 0.34\%$  and good breathability of  $75.2 \pm 6.1$  Pa for 2-layer stack. This composite pleated stack meets requirements of a level 1 barrier face covering (20% PFE, 149 Pa PD) as well as may be suitable for creating an N95 respirator. Finally, long duration testing of this composite filter indicates that the PFE of the filter increases over the test duration. However, the increase in PD for pleated samples and stacks is far lower than of their flat or pre-pleated counterparts by more than 90%. In effect, pleating as an approach to reduce PD without significantly compromising PFE was demonstrated to be a strategy that can be applied to other filter materials.

**Author Contributions:** Rong Wu<sup>†</sup>, Sneha Shanbhag<sup>†</sup> contributed equally. Rong Wu and Sneha Shanbhag conducted experiments and wrote the initial draft of the manuscript. P. Ravi Selvaganapathy supervised the project, analyzed results, and revised manuscript. Rong Wu led the fabrication of electrospinning layer, participant in the filtration test, humidity conditioning, and mechanical handling test. Rong Wu also contribute the writing and interpreting results.

**Funding Sources:** Sneha Shanbhag would like to acknowledge the funding from Natural Sciences and Engineering Research Council of Canada Postdoctoral Fellowship. Rong Wu would like to

acknowledge the Ontario Graduate Scholarship and The Queen Elizabeth II Graduate Scholarship.

We also acknowledge funding from FedDev Ontario and Ontario Together Fund.

**Notes:** Any additional relevant notes should be placed here.

**Acknowledgments:** We acknowledge RONCO Canada for providing melt-blown polypropylene fabric

## References

- [1] S. Sangkham, "Face mask and medical waste disposal during the novel COVID-19 pandemic in Asia," *Case Studies in Chemical and Environmental Engineering*, vol. 2, p. 100052, 2020/09/01/ 2020, doi: <https://doi.org/10.1016/j.cscee.2020.100052>.
- [2] Y. Deng, T. Lu, J. Cui, S. Keshari Samal, R. Xiong, and C. Huang, "Bio-based electrospun nanofiber as building blocks for a novel eco-friendly air filtration membrane: A review," *Separation and Purification Technology*, vol. 277, p. 119623, 2021/12/15/ 2021, doi: <https://doi.org/10.1016/j.seppur.2021.119623>.
- [3] Y. Zhang, "Effect of Electret Process Parameters on Filtration Performance of Polypropylene Melt-Blown Nonwoven Fabric," *Journal of Physics: Conference Series*, vol. 1622, no. 1, p. 012049, 2020/09/01 2020, doi: 10.1088/1742-6596/1622/1/012049.
- [4] J. Zhang, G. Chen, G. S. Bhat, H. Azari, and H. Pen, "Electret characteristics of melt-blown polylactic acid fabrics for air filtration application," *Journal of Applied Polymer Science*, vol. 137, no. 4, p. 48309, 2020, doi: <https://doi.org/10.1002/app.48309>.

- [5] X. Y. D. Soo *et al.*, "Polylactic acid face masks: Are these the sustainable solutions in times of COVID-19 pandemic?," *Science of The Total Environment*, vol. 807, p. 151084, 2022/02/10/ 2022, doi: <https://doi.org/10.1016/j.scitotenv.2021.151084>.
- [6] D. Lv *et al.*, "Green Electrospun Nanofibers and Their Application in Air Filtration," *Macromolecular Materials and Engineering*, vol. 303, no. 12, p. 1800336, 2018, doi: <https://doi.org/10.1002/mame.201800336>.
- [7] C. Ding *et al.*, "A Super-breathable “Woven-like” Protein Nanofabric," *ACS Applied Bio Materials*, vol. 3, no. 5, pp. 2958-2964, 2020/05/18 2020, doi: 10.1021/acsabm.0c00008.
- [8] X. Fan *et al.*, "Morphology engineering of protein fabrics for advanced and sustainable filtration," *Journal of Materials Chemistry A*, 10.1039/C8TA08717B vol. 6, no. 43, pp. 21585-21595, 2018, doi: 10.1039/C8TA08717B.
- [9] J. Hu, Z. Xiong, Y. Liu, and J. Lin, "A biodegradable composite filter made from electrospun zein fibers underlaid on the cellulose paper towel," *International Journal of Biological Macromolecules*, vol. 204, pp. 419-428, 2022/04/15/ 2022, doi: <https://doi.org/10.1016/j.ijbiomac.2022.02.029>.
- [10] S. Lin, X. Fu, M. Luo, and W.-H. Zhong, "Tailoring bimodal protein fabrics for enhanced air filtration performance," *Separation and Purification Technology*, vol. 290, p. 120913, 2022/06/01/ 2022, doi: <https://doi.org/10.1016/j.seppur.2022.120913>.
- [11] J. Liu, C. Ding, F. O. Dunne, Y. Guo, X. Fu, and W.-H. Zhong, "A Bimodal Protein Fabric Enabled via In Situ Diffusion for High-Performance Air Filtration," *Environmental Science & Technology*, vol. 54, no. 19, pp. 12042-12050, 2020/10/06 2020, doi: 10.1021/acs.est.0c02828.

- [12] Q. Jiang, N. Reddy, and Y. Yang, "Cytocompatible cross-linking of electrospun zein fibers for the development of water-stable tissue engineering scaffolds," *Acta Biomaterialia*, vol. 6, no. 10, pp. 4042-4051, 2010/10/01/ 2010, doi: <https://doi.org/10.1016/j.actbio.2010.04.024>.
- [13] S. Koombhongse, W. Liu, and D. H. Reneker, "Flat polymer ribbons and other shapes by electrospinning," *Journal of Polymer Science Part B: Polymer Physics*, vol. 39, no. 21, pp. 2598-2606, 2001, doi: <https://doi.org/10.1002/polb.10015>.
- [14] S. C. Coelho, P. Benaut, S. Laget, B. N. Estevinho, and F. Rocha, "Optimization of electrospinning parameters for the production of zein microstructures for food and biomedical applications," (in eng), *Micron (Oxford, England : 1993)*, vol. 152, p. 103164, Jan 2022, doi: 10.1016/j.micron.2021.103164.
- [15] N. Bhardwaj and S. C. Kundu, "Electrospinning: a fascinating fiber fabrication technique," (in eng), *Biotechnology advances*, vol. 28, no. 3, pp. 325-47, May-Jun 2010, doi: 10.1016/j.biotechadv.2010.01.004.
- [16] A. Haider, S. Haider, and I.-K. Kang, "A comprehensive review summarizing the effect of electrospinning parameters and potential applications of nanofibers in biomedical and biotechnology," *Arabian Journal of Chemistry*, vol. 11, no. 8, pp. 1165-1188, 2018/12/01/ 2018, doi: <https://doi.org/10.1016/j.arabjc.2015.11.015>.
- [17] Q. Jiang, N. Reddy, and Y. Yang, "Cytocompatible cross-linking of electrospun zein fibers for the development of water-stable tissue engineering scaffolds," (in eng), *Acta Biomater*, vol. 6, no. 10, pp. 4042-51, Oct 2010, doi: 10.1016/j.actbio.2010.04.024.

- [18] N. Reddy, Y. Li, and Y. Yang, "Alkali-catalyzed low temperature wet crosslinking of plant proteins using carboxylic acids," *Biotechnology Progress*, vol. 25, no. 1, pp. 139-146, 2009, doi: <https://doi.org/10.1002/btpr.86>.
- [19] X. Yu *et al.*, "Hydrophobic cross-linked zein-based nanofibers with efficient air filtration and improved moisture stability," *Chemical Engineering Journal*, vol. 396, p. 125373, 2020/09/15/ 2020, doi: <https://doi.org/10.1016/j.cej.2020.125373>.
- [20] H. Souzandeh, L. Scudiero, Y. Wang, and W.-H. Zhong, "A Disposable Multi-Functional Air Filter: Paper Towel/Protein Nanofibers with Gradient Porous Structures for Capturing Pollutants of Broad Species and Sizes," *ACS Sustainable Chemistry & Engineering*, vol. 5, no. 7, pp. 6209-6217, 2017/07/03 2017, doi: 10.1021/acssuschemeng.7b01160.
- [21] H. Souzandeh *et al.*, "Cross-Linked Protein Nanofilter with Antibacterial Properties for Multifunctional Air Filtration," *ACS Applied Materials & Interfaces*, vol. 9, no. 27, pp. 22846-22855, 2017/07/12 2017, doi: 10.1021/acsami.7b05796.
- [22] J. J. Huang, Y. Tian, R. Wang, M. Tian, and Y. Liao, "Fabrication of bead-on-string polyacrylonitrile nanofibrous air filters with superior filtration efficiency and ultralow pressure drop," *Separation and Purification Technology*, vol. 237, p. 116377, 2020/04/15/ 2020, doi: <https://doi.org/10.1016/j.seppur.2019.116377>.
- [23] N. Reddy, Y. Li, and Y. Yang, "Wet cross-linking gliadin fibers with citric acid and a quantitative relationship between cross-linking conditions and mechanical properties," (in eng), *Journal of agricultural and food chemistry*, vol. 57, no. 1, pp. 90-8, Jan 14 2009, doi: 10.1021/jf802341u.

- [24] C.-W. Chen, S.-H. Huang, C.-M. Chiang, T.-C. Hsiao, and C.-C. Chen, "Filter Quality of Pleated Filter Cartridges," *The Annals of Occupational Hygiene*, vol. 52, no. 3, pp. 207-212, 2008, doi: 10.1093/annhyg/men008.
- [25] B. H. Park, M. H. Lee, Y. M. Jo, and S. B. Kim, "Influence of pleat geometry on filter cleaning in PTFE/glass composite filter," (in eng), *Journal of the Air & Waste Management Association (1995)*, vol. 62, no. 11, pp. 1257-63, Nov 2012, doi: 10.1080/10962247.2012.696530.
- [26] S. Fotovati, S. A. Hosseini, H. Vahedi Tafreshi, and B. Pourdeyhimi, "Modeling instantaneous pressure drop of pleated thin filter media during dust loading," *Chemical Engineering Science*, vol. 66, no. 18, pp. 4036-4046, 2011/09/15/ 2011, doi: <https://doi.org/10.1016/j.ces.2011.05.038>.
- [27] Y. Bian, L. Zhang, and C. Chen, "Experimental and modeling study of pressure drop across electrospun nanofiber air filters," *Building and Environment*, 2018.
- [28] Q. Zhang, Q. Li, T. M. Young, D. P. Harper, and S. Wang, "A Novel Method for Fabricating an Electrospun Poly(Vinyl Alcohol)/Cellulose Nanocrystals Composite Nanofibrous Filter with Low Air Resistance for High-Efficiency Filtration of Particulate Matter," *ACS Sustainable Chemistry & Engineering*, vol. 7, no. 9, pp. 8706-8714, 2019/05/06 2019, doi: 10.1021/acssuschemeng.9b00605.
- [29] Z. Yang *et al.*, "Airflow Synergistic Needleless Electrospinning of Instant Noodle-like Curly Nanofibrous Membranes for High-Efficiency Air Filtration," *Small*, vol. 18, no. 14, p. 2107250, 2022, doi: <https://doi.org/10.1002/sml.202107250>.

- [30] Z. Wang, C. Zhao, and Z. Pan, "Porous bead-on-string poly(lactic acid) fibrous membranes for air filtration," *Journal of Colloid and Interface Science*, vol. 441, pp. 121-129, 2015/03/01/ 2015, doi: <https://doi.org/10.1016/j.jcis.2014.11.041>.
- [31] D. Buivydiene, A. M. Todea, C. Asbach, E. Krugly, D. Martuzevicius, and L. Kliucininkas, "Composite micro/nano fibrous air filter by simultaneous melt and solution electrospinning," *Journal of Aerosol Science*, vol. 154, p. 105754, 2021/05/01/ 2021, doi: <https://doi.org/10.1016/j.jaerosci.2021.105754>.
- [32] S. Li *et al.*, "Influence of pleat geometry on the filtration and cleaning characteristics of filter media," *Separation and Purification Technology*, vol. 210, pp. 38-47, 2019/02/08/ 2019, doi: <https://doi.org/10.1016/j.seppur.2018.05.002>.
- [33] K. Cheng, J. Zhu, F. Qian, B. Cao, J. Lu, and Y. Han, "CFD–DEM simulation of particle deposition characteristics of pleated air filter media based on porous media model," *Particuology*, vol. 72, pp. 37-48, 2023/01/01/ 2023, doi: <https://doi.org/10.1016/j.partic.2022.02.003>.
- [34] N. Anantharamaiah, H. V. Tafreshi, and B. Pourdeyhimi, "A study on flow through hydroentangling nozzles and their degradation," *Chemical Engineering Science*, vol. 61, no. 14, pp. 4582-4594, 2006/07/01/ 2006, doi: <https://doi.org/10.1016/j.ces.2006.01.038>.

## **Supplementary Information**

### Supplementary background

In the context of air filters, especially for facemask applications, standards and regulations such as ASTM F2100 (medical face masks or surgical masks), ASTM F3502 (barrier face coverings), [1] or regulations such as 42 CFR Part 84 (NIOSH N95 respirators) [2] provide testing guidelines and performance criteria. These tests characterize the filter materials' particle filtration efficiency and pressure drop under instantaneous conditions, high salt loading and high humidity.

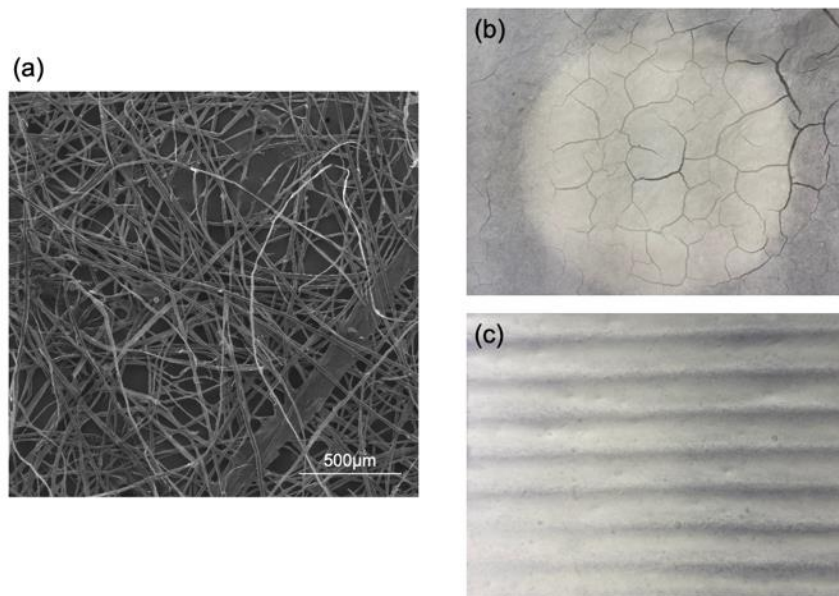


**Figure S3.1** (a) SEM figure of crafted tissue paper substrate (b)Cracks on uncrosslinked zein filter after humidity conditioning for 1 hour; (c) un-uniform coverage of pleated filter along the fold lines.

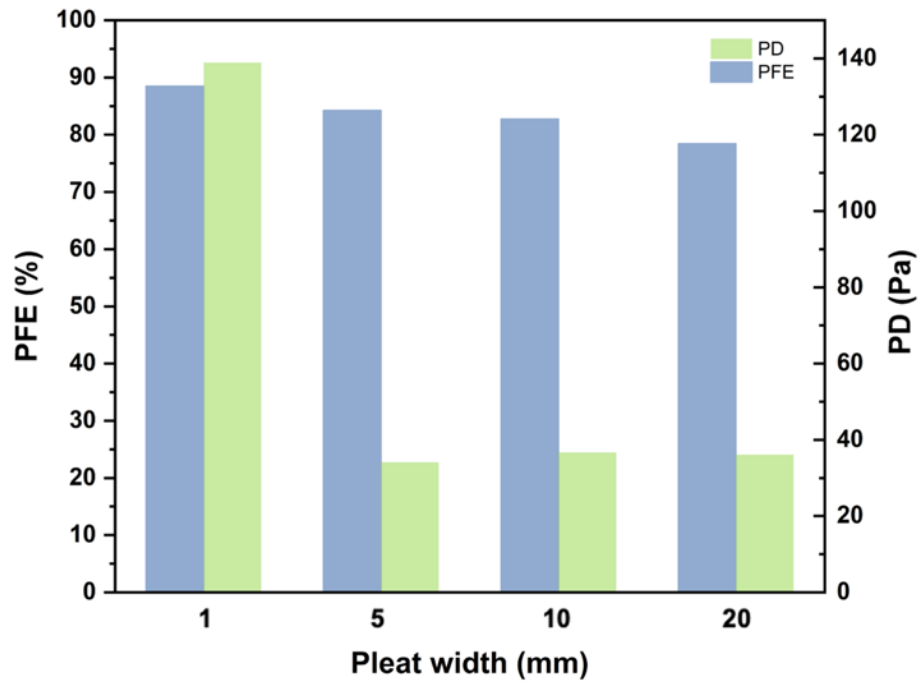


**Figure S3.2** PFE and PD performance with different pleat width.

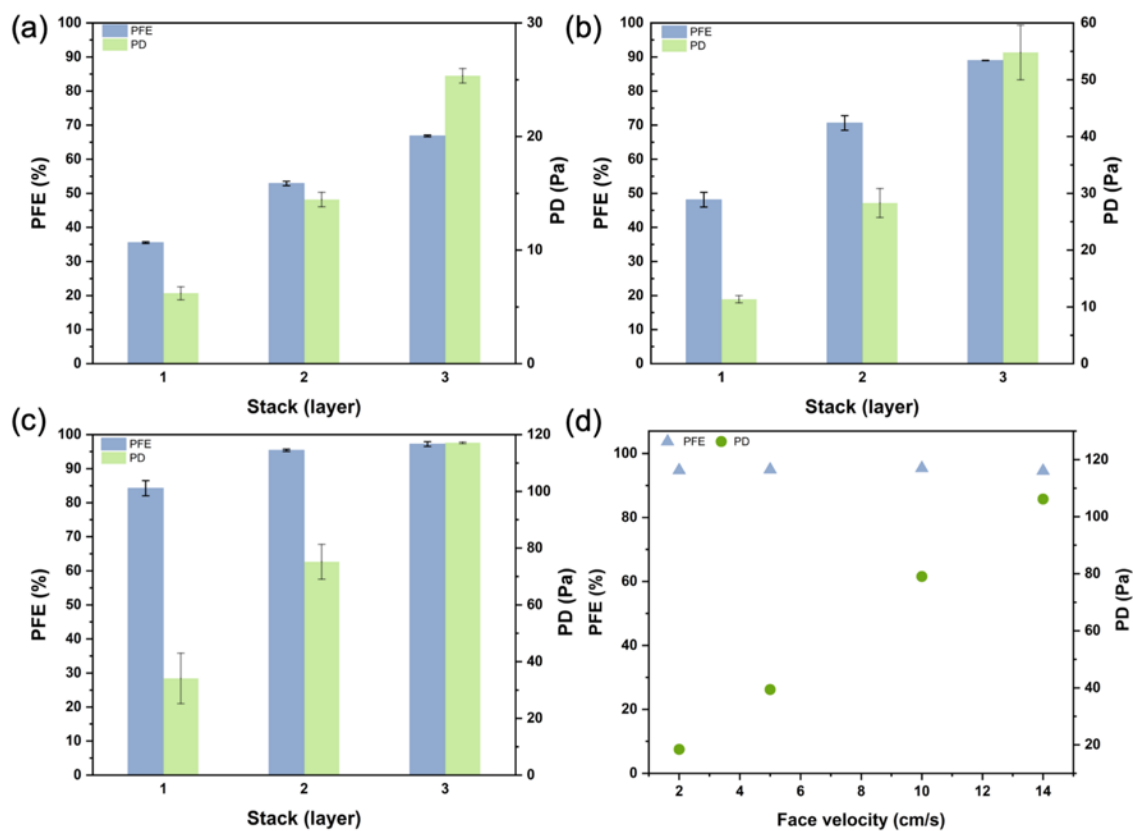


**Figure S3.3** PFE and PD of pleated crosslinked zein filter at (a) 5 min; (b) 15 min; (c) 25 min, (d) PFE and PD of 2-layer stack of pleated zein filter at various face velocities.

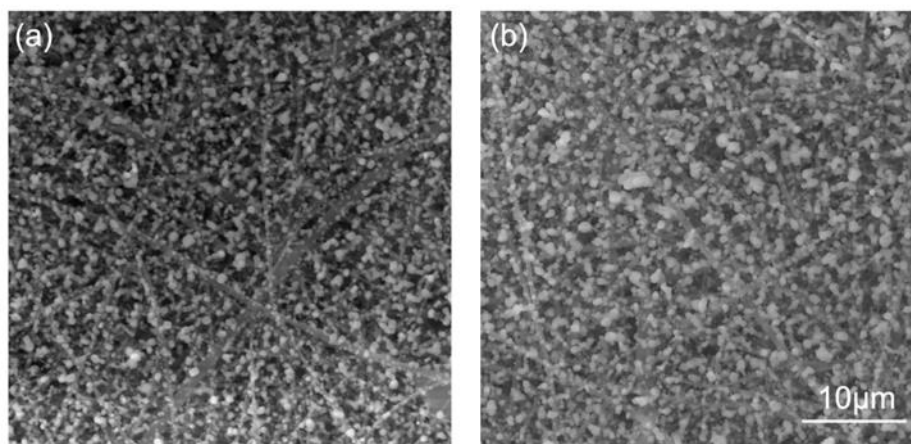


**Figure S3.4** SEM images of (a) flat zein filter, (b) pre-pleated zein filter, after one hour loading test.

We also characterized the craft paper substrate, uncrosslinked filter, crosslinked filter materials by FTIR. The FT-IR spectra of those samples were measured via a Fourier transform infrared spectrometer, Bruker Vertex 70 spectrometer (Bruker Ltd., Germany) from  $4000$  to  $500\text{ cm}^{-1}$ . The crosslinked zein and uncrosslinked zein filter with paper substrate provided similar response under FTIR. The peak at  $1481$ ,  $1566$ , and  $1633$  matched with previous study indicated the similar compounds in both samples[3].

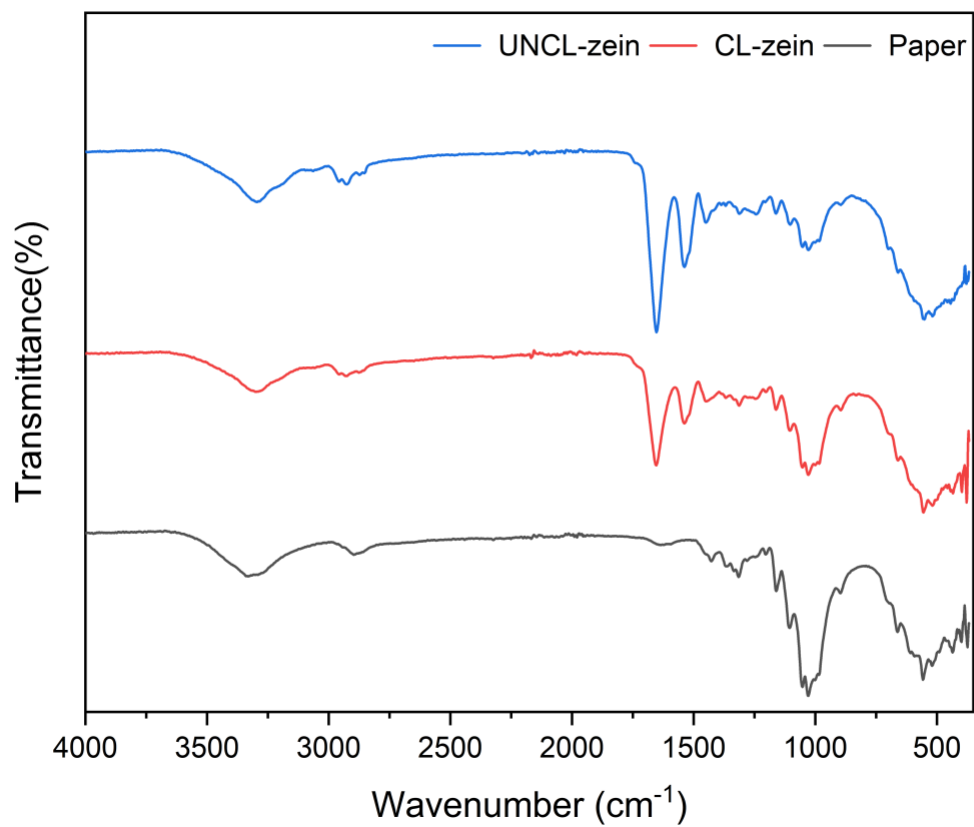


**Figure S3.5** FTIR spectrum of paper substrate, crosslinked and uncrosslinked zein electrospun layer with paper substrate.



**Figure S3.6** Photograph of NE300 electrospinner.



**Figure S3.7** Photograph of TSI 8130A for filtration.

**Reference**

- [1] *Standard Specification for Barrier Face Coverings*, A. S. f. T. a. Materials, February 15, 2021 2021.
- [2] *Approval of respiratory protective devices*, T. N. I. f. O. S. a. Health, 1995.
- [3] S. Ali, Z. Khatri, K. W. Oh, I.-S. Kim, and S. H. Kim, "Zein/cellulose acetate hybrid nanofibers: Electrospinning and characterization," *Macromolecular Research*, vol. 22, pp. 971-977, 2014.

## **Chapter 4 Porous biocompatible colorimetric nanofiber-based sensor for selective ammonia detection on personal wearable protective equipment**

R. Wu<sup>a</sup>, P.R. Selvaganapathy<sup>\*a,b</sup>

<sup>a</sup> *Department of Mechanical Engineering, McMaster University, Hamilton L8S 4L8*

<sup>b</sup> *Department of Biomedical Engineering, McMaster University, Hamilton L8S 4L8*

\*Authors to Whom Correspondence Should Be Addressed

E-mail: selvaga@mcmaster.ca

**Keywords:** ammonia gas; colorimetric sensor; core-shell nanofiber; gas detection; one-step fabrication

**Status:** Under review-Sensors and Actuators B: Chemical (Submission date: March 20<sup>th</sup>)

**Contribution:** To fulfill the active function of next generation of PPE, this chapter developed the colorimetric ammonia sensor with eye-readable sensing response. The electrospinning sensor can be directly fabricated with one-step and combined with filter material without compromising of filter performance. It also demonstrate the excellent resistance to both gas and liquid phase of interferences which are commonly presented in human breath and working environment.

## **Abstract**

The colorimetric sensor is an economical, facile, and power-free material for gas detection. Ammonia is widely involved in various industries and overexposure will lead to death. In this study, we showed a one-step fabrication of a colorimetric sensitive and selective ammonia platform. This sensor was based on simple pH-indicator immobilization electrospun mat with naked eye readable sensitivity and was able to detect concentrations of ammonia as low as 0.5 ppm in a fast response time of 10 sec. The core-shell bi-polymer nanofiber mat was produced based on single nozzle electrospinning setup with biocompatible polymers. We highlighted the durable stability under gaseous interference of VOCs and high pH liquid interference which is important in combination with Personal Protective Equipment in industrial environments. The detection range is adjustable and extendable by combining different ratios of dual polymer sensors without compromising the other performances of the sensor. PPE with integrated colorimetric sensors could potentially be equipped on workers in different industries to indicate the presence of ammonia in a visual way to provide a comprehensive protection.

## 1. Introduction

As air pollution has increased over the past few decades, the urgent need for environmental monitoring has become increasingly important [1]. Occupational Safety and Health Administration (OSHA) restricts exposure to many toxic gases used in chemistry, agriculture, medical, food production and other industrial applications including ammonia which is widely used as a catalyst or reagent in various industries [2, 3]. OSHA has set regulatory limits of exposure and determined that ammonia concentration greater than 25 ppm can cause nasal irritation, and long-term exposure to concentrations greater than 35 ppm can lead to acute toxicity in humans. Exposure to ammonia gas above 300 ppm is known to cause death. Therefore, the sensitive detection of ammonia is of great importance in environmental monitoring, personnel protection and industrial process control.

A variety of sensing technologies are available for  $\text{NH}_3$  detection currently including metal oxide-based sensors [4, 5], conducting polymer sensors [6], optical sensors [7], electrochemical sensors [8], surface acoustic wave sensors [9]. However, the high sensitivity and selectivity of some of these sensors rely on expensive, non-portable ancillary instruments or power supplies, which limits their widespread use in day-to-day applications. Colorimetric sensors have attracted great interest as a promising detection technology because they are low-cost, simple, easy to fabricate, and can be visualized by eye without additional instrumentation and power consumption [10-12]. The underlying principle of operation is based on different mechanisms of color change, such as electrochromic, thermochromic, and halochromic principles [13, 14]. Conventionally, pH indicator is commonly used in the colorimetric ammonia detection due to its low cost and reliable halochromic reaction. Ammonia is generally a weak base and can accept a proton which makes it

convenient to use this mechanism for its sensing. However, it is also non-specific. The eye-readable colorimetric sensing platform is the simplest detection of ammonia that produces a color change upon contact with the gaseous analyte. For example, Bromophenol blue (BPB), a yellow pH indicator, has been used for both pH and ammonia detection as it donates a proton upon exposure to ammonia or other bases which results in its color change [15, 16]. Achieving a reliable and highly sensitive sensor depends on the immobilization and homogeneous distribution of the dye in the sensing medium. The incorporation of these dye-based colorimetric gas sensors into personal protective equipment is an innovative and fascinating application, and can be part of a new generation of smart PPE for monitoring a variety of volatile chemicals in the environment. Equipping PPE (e.g., masks) that currently only protect against particulate matter to sense the presence of other toxic contaminants such as ammonia present in the environment can add another level of safety and prevent accidental exposure. One of the challenges is to integrate the responsive materials in the form factor of non-wovens for application in PPEs.

In recent years, electrospun nanofibers have attracted a great interest as a support medium for gas sensors [17-19]. Micro or nanofibrous electrospun membranes greatly increase the surface-to-volume ratio and allow uniform immobilization of the dye, which is beneficial for the sensor performance. Additionally, the morphology and structure of electrospun membranes are tunable by changing the process parameters. Based on previously studies, electrospinning is a feasible way to encapsule colorimetric dyes to build gas sensors. For instance, Ding et al. developed a colorimetric sensor by incorporating methyl yellow dye into nylon6 electrospun membranes for formaldehyde detection with a low detection limit of 50 ppb [20]. Similarly, Hoang et al. fabricated the polyacrylonitrile mats by electrospinning with bromocresol green to detect ammonia [21]. This colorimetric sensor showed excellent selectivity among common volatile organic solvents, less

than 1 minute response time and 1ppm detection limit. Nevertheless, this sensor is not selective and will be responsive to other bases that may be present and is pH responsive. Alternatively, Kim et al. developed a dye-loaded smart yarn with multi-gas detection by lead-based dyes ( $\text{PbI}_2$ ) on supporting wire with 1 ppm level detection and reaching maximum response within 20s [22]. However, this sensor is not applicable for PPEs as the use of Pb nanoparticles, which is a harmful aerosol contaminant, in masks where the air flow through it is breathed in can lead to accidental exposure in situations where damage masks can become damaged in use. Due to the non-selectivity of the pH and ammonia sensitive colorimetric dyes, it is important to coat them with a selective membrane that will only allow ammonia to permeate and allow color change to occur. This should be done without compromising the response time of the colorimetric sensor.

In this study, we developed a one-step fabrication of a colorimetric sensing platform for sensitive and selective ammonia detection based on simple pH-indicator immobilization with fast response time. The sensing nanofiber mat was prepared by single-nozzle based electrospinning to fabricate a self-assembling core-shell like bi-polymer structure made of an air-permeable, water repellent Polydimethylsiloxane (PDMS) outer shell and an inner core of the colorimetric dye (BPB) in a carrier of Polycaprolactone (PCL). This electrospun layer was deposited on the spunbond Polypropylene for mechanical support. The fabricated mat was fully biocompatible with good mechanical durability and water repellence. The sensor showed high sensitivity and was able to detect concentrations of ammonia as low as 0.5 ppm to more than 50 ppm in a fast response time of 10 sec. It was able to successfully prevent interference from other bases in the liquid and aerosol form that could cause interference. It also did not show any interference from other volatile organic solvents that could penetrate the PDMS outer shell. Finally, the sensor was able to be reused multiple times and did not show hysteresis. This low cost, visually readable and no-power

sensor can be implemented on PPEs such as facemasks to provide rapid and instantaneous detection of toxic chemicals in the environment. The platform of coaxial PDMS encased colorimetric sensing non-wovens can be used for other gas sensing applications.

## **2. Experimental section**

### **2.1 Materials**

Polycaprolactone (Mw 80,000 g/mol), Bromophenol blue (ACS reagent), Dichloromethane (anhydrous,  $\geq 99.8\%$ ), N,N- dimethylformamide (ACS reagent,  $\geq 99.8\%$ ) were procured from Sigma–Aldrich Inc. Polydimethylsiloxane (PDMS, Sylgard 184) was obtained from Dow Corning, USA. Reagent-grade Acetone, Methanol was purchased from ACP Chemicals Inc. Ethyl alcohol (Ethanol, anhydrous) was sourced from Commercial alcohols by Greenfield Global. The Spunbonded Polypropylene (PP, 50 g/m<sup>2</sup>) fabric supplied by Nolar Industries Ltd Canada was used as the substrate of sensor.

### **2.2 Preparation of electrospinning sensors**

The process flow diagram of nanofiber-based sensor fabrication process is illustrated in Figure 4.1a. First, a 10 wt% PCL solution was prepared by dissolving PCL polymer in the solvent mixture of DCM, DMF and ethanol with ratio of 4.5:4.5:1. Bromophenol blue (BPB) was added in the solution within the range of 0.5-3 wt%. The solution was stirred and heated to 50°C for 2 hours and cooled down to room temperature. PDMS was prepared by mixing curer and base in a weight ratio of 1:10. The mixture was then degassed in a vacuum desiccator to extract and eliminate air bubbles in the mixture and then added in the prepared PCL solution with ratio of 1:1, 1:2, 1:3 and 1:4 between PCL and PDMS with 1hour stirring. The resultant homogeneous solution was loaded in the 10ml syringe with 18-gauge needle. The schematic of self-built electrospinning setup is

provided in Figure 4.1b. The electrospinning solution was supplied at a flow rate of 3 ml/h via a syringe pump (Pico plus elite, Harvard Apparatus, US) to feed solution in the electric field provided by a high voltage supply (EQ-30P1, Matsusada Precision Inc, Japan) of 14 kV to form nanofibers. A flat aluminum board collector covered by 10cm x 10cm PP nonwoven fabric was mounted with a 10cm distance to the syringe tip. Bi-polymer nanofibers were collected for 15 minutes. Subsequently, the bi-polymer mat on nonwoven fabric was dried and cured at room temperature before sensing characterization. A PDMS spin coated sample on PCL electrospinning fabric was fabricated as comparison with 1000 rpm for 30 s.

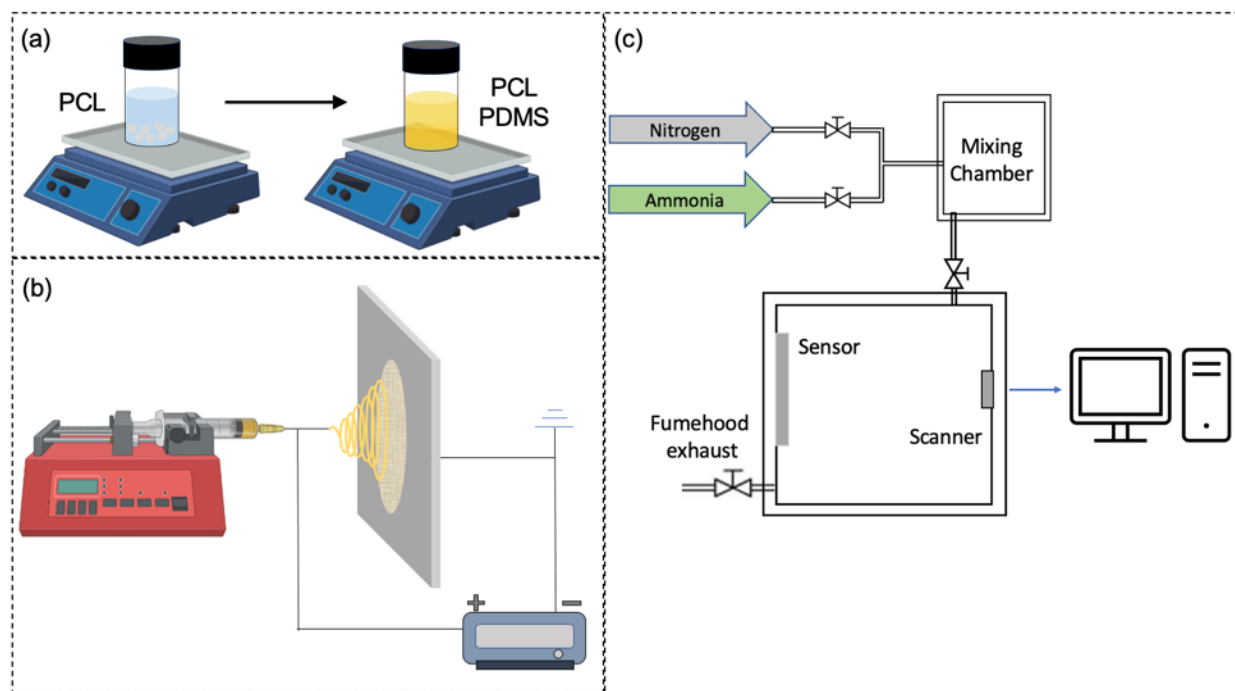


**Figure 4.1** (a) Schematic showing the bi-polymer solution preparation. First, 10 wt% of PCL was prepared and then BPB, PDMS with different ratio to PCL was added into the solution for continuous stirring. (b) Schematic of electrospinning setup. A horizontal configuration was used consisting of syringe pump, flat PP covered aluminum collector and a high voltage supply. (c)

Schematic of test chamber setup. The prepared gases were controlled by MFC and mixed in the mixing channel then exposed to sensors in the test chamber with camera monitoring.

### **2.3 Sensor Surface characterizations**

Scanning electron microscopy (SEM) images were collected to investigate the surface and fiber morphology of the electrospun samples using a TESCAN VEGA -II LSU SEM. Electrospun fabric samples were coated with 10 nm layer of gold using a sputter coater to enhance the surface conductivity. SEM images were captured for electrospun samples of various PDMS concentration conditions. Fiber diameter distributions were obtained based on the SEM images. Fiber diameters were measured manually for over hundred measurements by ImageJ and plotted accordingly. The FT-IR spectra of sensor surfaces were measured via a Fourier transform infrared spectrometer, Bruker Vertex 70 spectrometer (Bruker Ltd., Germany) from 4000 to 500  $\text{cm}^{-1}$ . Optical images of sensor surfaces were captured by PC controlled Raspberry Pi Camera (Raspberry Pi, US) and iPhone.

### **2.4 Colorimetric ammonia detection of bi-polymer sensors**

The real time color change behavior of colorimetric sensors with different configurations were evaluated by utilizing a gas test system with specific concentration of target analyte. The schematic of setup is illustrated in Figure 4.1c and S4.1. Gaseous ammonia was produced by chemical reaction of ammonium chloride and sodium hydroxide with different amount and external heat at 80°C and dried by sodium hydroxide in the sealed container and then mixed with  $\text{N}_2$ . Based on the internal volume of the entire system, mass flow controllers (MFC) were used to control flow rate of  $\text{N}_2$  and  $\text{NH}_3$  that were delivered into the mixing channel fulfilled with air. The gas measurement chamber was built with a plastic box to achieve constant illumination level and prompt the

reliability and repeatability of color change analysis. The as-prepared sensors with nonwoven fabric were manually placed on the sample stage against camera and the ammonia gas was continuously introduced into the testing chamber with 1.5L size. A constant illumination was provided with configuring a 6000lux LED white light source. All the measurements were collected in ambient conditions at a room temperature at 22 °C. Camera connected to the remote PC captured the color change every 5 s for 5-10 minutes. Subsequent measurements of mean RGB values were extracted via Image J. The obtained RGB values were converted to equivalent L\*a\*b\* value which is a measure that is more representative of color change and its sensitivity to the human eye. In this mode the L\* represents lightness, a\* represents red/green and b\* represents yellow/blue [22]. Change of L, a, b value was calculated before and after ammonia exposure at each condition. The total color change value ( $\Delta E$ ) of sensor was defined and calculated using eq.1. It is worth noting that  $\Delta E$  equal to or greater than 3.3 is considered color change that can be detected by the naked eye of a normal person [23].

$$\Delta E = \sqrt{(\Delta L)^2 + (\Delta a)^2 + (\Delta b)^2} \quad (1)$$

### **3. Results and discussion**

#### **3.1 Spincoated PDMS for water repellent sensor performance**

One way of preventing non-specific response of the ammonia sensing layer to changes in pH is to protect it using a coating that is permeable to gases but not to ions. PDMS is such a water repellent coating that is both ion impermeable and gas permeable. We first used spincoating to produce 100  $\mu\text{m}$  PDMS layer on electrospinning PCL nanofiber mat with BPB which served as the colorimetric response layer. After ammonia exposure, the bright yellow color of sensor samples changed to a dark blue color tone gradually as shown in the optical images of spincoated sensor obtained before

and after exposure (Figure 4.2a). Protonation of the pH indicator caused by the reaction with  $\text{NH}_3$  determines the color change. However, the blue color was uneven and heterogenous in its distribution even with 300s exposure which could be due to the uneven distribution of the PDMS over the electrospun non-woven material. The sensing performance was evaluated at various gas concentrations between 0.5 to 20 ppm and shown in Figure 2b. The sensor was not as responsive to concentrations below 2.5 ppm and did not stabilize within 300 sec (5 min) for higher concentrations. The best performance was found to be between 5-10 ppm which is in the range of regulatory limits for sensing of ammonia. Even at high concentrations of 20 ppm it took more than a minute to start responding. The time for stabilization of the color which will determine the response time was found to be dependent on the concentration of the exposure and it did not stabilize even after 10 minutes for an exposure concentration of 100 ppm ammonia gas. For spincoated thick PDMS layers, the kinetics of color change is limited by the rate of diffusion of  $\text{NH}_3$  gas molecules through the PDMS layer. Due to unevenness of the electrospun layer, the spin coating process leads to retention of more PDMS in certain regions and less in others which results in the heterogenous color change that is seen in Figure 4.2a. Moreover, the thick layer of PDMS to completely cover the non-woven material and seal in the dye also results in slow response. Therefore, an alternative way of fabricating coated non-woven sensors can increase sensitivity and also decrease the response time.

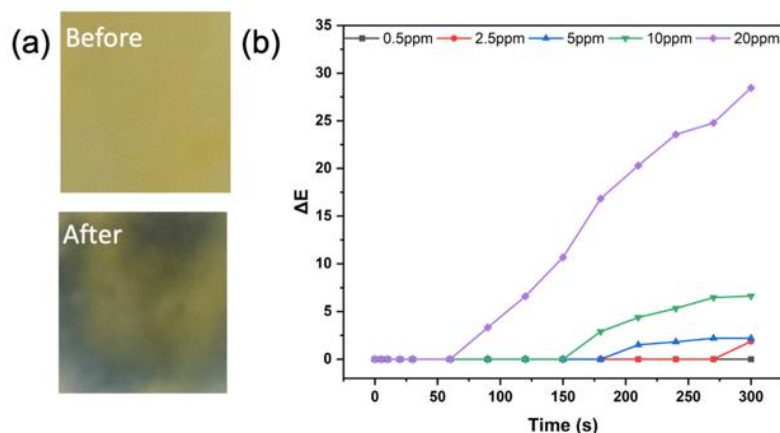


**Figure 4.2** (a) Optical photographs of sensor with spin-coated PDMS on electrospun PCL before and after ammonia exposure. (b) Spin-coated sensor response curve to various concentrations of ammonia.

### 3.2 Fabrication of bi-polymer co-axial nanofiber sensors

In order to develop a coating of the individual fibers rather than the entire mat, we utilized one-step electrospinning to produce self assembled coaxial bi-polymer nanofiber-based non-woven using a PCL loaded with the dye and PDMS as the starting mixture. First, we characterized the morphologies of electrospun fibers prepared from different ratio of PDMS to PCL respectively using SEM to identify the compositions that will produce a suitable coaxial coating of PDMS. The distributions of the fiber diameter of bi-polymer nanofibers were obtained from the SEM images. As shown in Figure 4.3, the fiber structures and diameters are significantly different for various ratios. The SEM image of electrospinning PCL shown in Figure 3a shows the typical morphology of a nonwoven film composed of randomly oriented nanofibers with similar diameters. It can be seen from Figure 4.3a that the fibers from 100% PCL solution consist of clean and independent ultrafine fibers, whereas the fibers fused at their junction when PDMS was introduced into the

composition of the solution as in Figure 4.3b-e. Ratios of 1:2 and 1:3 PCL: PDMS still produced porous non-woven membranes as seen from the SEM images while higher PDMS ratio (1:4) results in a non-porous continuous film of PDMS interspread with fibers of PCL.

The fiber diameter distributions of fibers in each sample under various conditions were analyzed and plotted in Figure 4.3f-h. The average diameters of sample 1-3 are 0.27  $\mu\text{m}$ , 0.56  $\mu\text{m}$ , and 0.58  $\mu\text{m}$ , respectively. Fiber diameters could not be calculated for those compositions where the ratio was 1:3 and 1:4, as they produced continuous PDMS films. However, the 1:1 and 1:2 ratios had good porosity and high surface to volume ratio that facilitates the efficient contact area suitable for gas sensing and ensures air permeability for PPE applications. To determine the organization of the nanofibers, we immersed the cut fibers into acetone that will partially dissolve the PCL and will not affect the PDMS. Cross section of these partially dissolved fibers observed under SEM (Figure 4.4) show a hollow tubular structure of PDMS demonstrating the formation of a co-axial arrangement with PCL in the inner core and PDMS in the outer layer. Some of the fibers collapsed into flat ribbon like layers due to complete removal of PCL. This structure may be formed during the drying process, when solvent evaporates after dissolution of the PCL and the flexible PDMS is pulled together due to capillary forces. Eventually, a core-shell like structure was formed after the sensing film was completely dried. Such structures provide the surface with good water repellent properties to prevent interference in the form of liquids, which will be discussed later.

Typically, core-shell fibers are produced using coaxial nozzles. However, here we have successfully produced core-shell fibers composed of PCL inner core and PDMS outer sheath using a single nozzle setup and a homogenous mixture of PDMS and PCL at various ratios. To our best knowledge this is the first production of core shell fibers using PCL and PDMS combinations.

Previous attempts have used block co-polymers consisting of PCL and PDMS ends and electrospinning to create such arrangements [24]. The formation of core-shell configuration can be due to the different rates of polymerization of the two components. The PCL solidifies rapidly as it loses solvent during the electrospinning process and ends up forming the core layer providing structural support to the still uncrosslinked PDMS. The PDMS solidifies much later due to slower crosslinking. Increase in PDMS ratio results in the pores of the electrospun membrane filled with the uncrosslinked PDMS before it cures lead to a continuous film. However, the appropriate ratio of PDMS ensures adequate coating of the individual fibers will prevent the filling of the pores results in usable nanofibrous mat suitable for filtration and sensing purposes. The PDMS provides mechanical elasticity that enables a robust and stable sensor. Notably, both PDMS and PCL are biocompatible synthetic polymers that have numerous applications in biomedicine, cell culture, etc., which makes them safe and potentially harmless for use in contact with human skin.

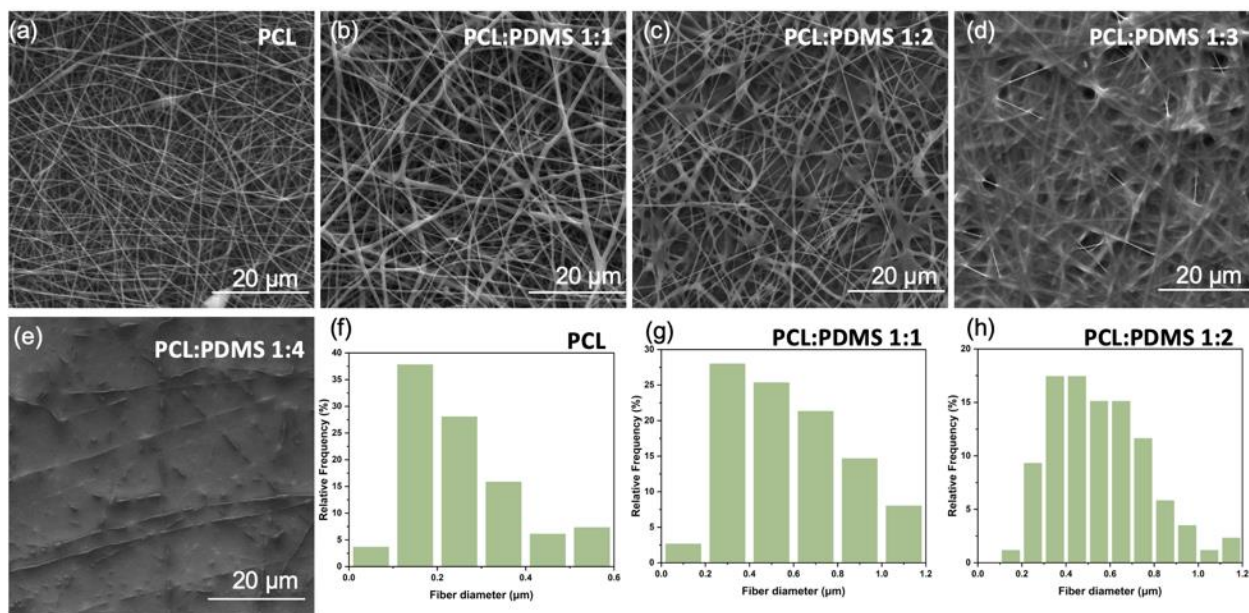


**Figure 4.3** (a)-(e) SEM images of samples with various ratio of PCL and PDMS. (f)-(h) Fiber diameter distribution of samples with various ratio of PCL and PDMS.

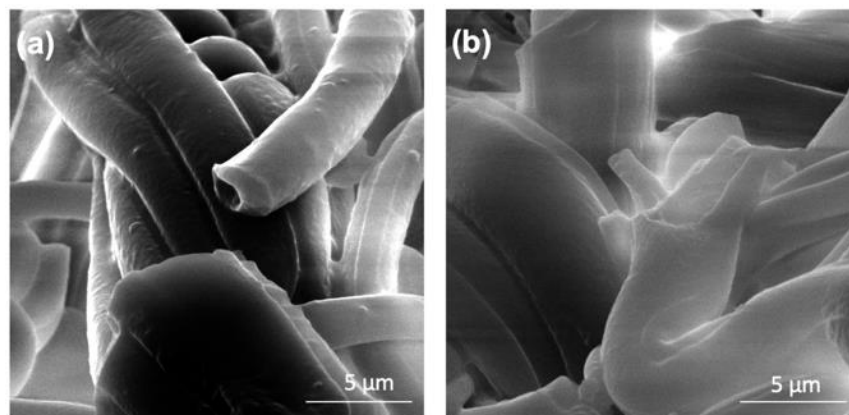


**Figure 4.4** SEM of bi-polymer fiber after acetone immersion.

We also conducted FTIR spectroscopy on electrospun nanofiber samples with various ratio of PDMS and PCL to as shown in Figure 4.5. The spectrum shows the band at  $1042\text{ cm}^{-1}$  which can be attributed to the stretching vibration of the Si-O bond in Si-O-Si straight chain. There are characteristic Si-C-H and Si-C stretching in the spectra at  $824$  and  $1245\text{ cm}^{-1}$ . These bands also appear in the FTIR spectrum of samples with PDMS in the electrospinning solution, which indicates the presence of the PDMS uniformly distributed on the PCL nanofibers formed. The stretching vibration of the carbonyl group appears at  $1725\text{ cm}^{-1}$ , which is attributed to the ester structural unit in the PCL. Previous studies on electrospinning of PDMS have shown that PDMS on its own cannot be electrospun but requires a carrier polymer [25]. However, the carrier polymer, poly vinyl alcohol (PVA) was introduced as the outside sheath using a coaxial nozzle. Here, we show that the complex co-axial geometry is not required and the PDMS can form a shell due to differences in cross linking and solidification times. From the FTIR results, PDMS in four different ratios of solutions were successfully electrospun and attached to the substrates with PCL. The assignment of all FTIR peaks agrees well with the literature values[26, 27].

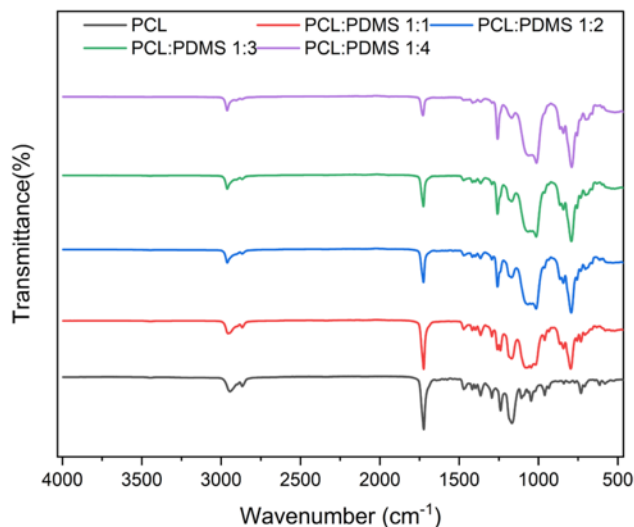


**Figure 4.5** FTIR of samples with PCL and PCL/PDMS with different ratios.

### 3.3 Sensitivity performance of colorimetric ammonia sensor

To evaluate the sensor performance, the electrospun sensors with different dye ratios was fabricated and evaluated in the test chamber. Color changes were continuously monitored and recorded. Figure 4.6a shows the room temperature optical photo of colorimetric sensors with different dye concentration. As mentioned before, D1-0.5%, D2-1%, D3-2% and D4-3% of dye concentration was evaluated. From the optical images, the starting  $L^*a^*b^*$  value were different with increasing concentration of dye. The optical color changes after ammonia exposure were also captured by photograph and illustrated in Figure 4.6b. After ammonia exposure, the bright yellow color of electrospun sensor samples changed to a dark blue color more uniformly compared with spincoated samples. The intensity of the final saturated blue color varied with different amount of dye added. A concentration dependent kinetic study was performed to investigate the color changing process of BPB-bi-polymer nanofiber sensors to determine the stabilized color change value which was important to obtain reliable results from the sensing measurements. The stabilized

color change values (90% of maximum value) were plotted in Figure 4.6c. Dye concentrations from 0.5 to 3% (D1-D4) were tested and evaluated and all samples exhibited a distinguishable value of maximum  $\Delta E$ . The value of the stabilized  $\Delta E$  is almost proportional to the concentration of dye in the solution. Interestingly, the maximum sensitivity of the sensor was not significantly affected by the dye content, with a saturation concentration of about 20 ppm, implying that the ratio of the bi-polymer is the dominant factor related to the sensitivity of the proposed sensor. At low dye content (0.5%),  $\Delta E$  reached stabilized value at lowest value. From Figure 4.6c, stabilized value of  $\Delta E$  increases by 4.1% at saturation stage of 1% dye concentration and 11.4% for both 2% and 3% dye concentration. Although the absolute values are higher at 3% concentration compared with 2%, the change of color can be detected by naked eyes to a similar degree for both. Hence, the 2% dye concentration was chosen as the optimum for subsequent experiments.

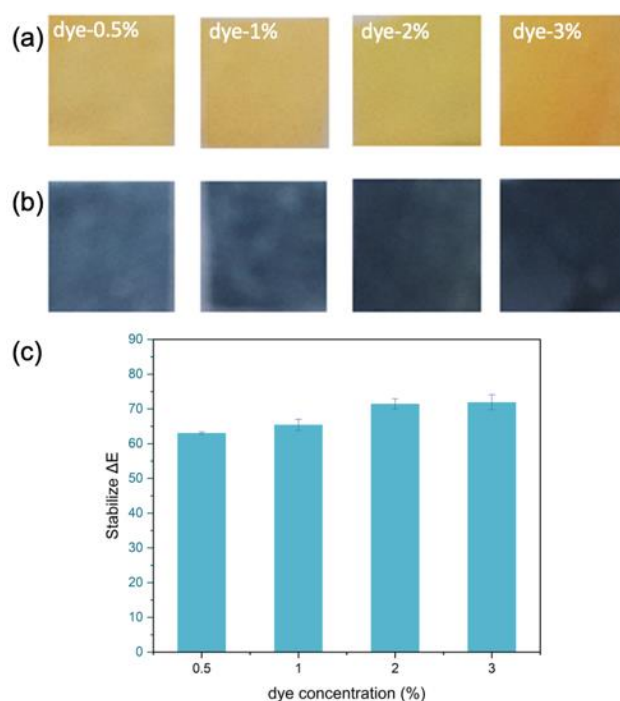


**Figure 4.6** The room temperature optical photos of colorimetric sensors with different dye concentration from D1-0.5%, D2-1%, D3-2%, D4-3% (a) before and (b) after ammonia exposure. (c) Relationship of the color change to the dye concentration.

We further evaluated the effect of polymer ratio from 1:1 to 1:4 on sensor performance with optimized dye concentration. Color change responses ( $\Delta E$ ) of sensors with time-dependent variations produced from different ratio of bi-polymer are shown in Figure 4.7. In comparison with spincoated sensors, electrospun nanofiber-based sensors exhibited a much more rapid change in color and achieved stability within 5 minutes for all ratios. Notably, the  $\Delta E$  of samples are eye-readable even at low concentration except R4 (ratio 1:4 which results in a continuous PDMS film) which means the sensor response can be detected without any extra equipment but naked eyes. The reaction time is defined based on eye-readability of sensor response which is within 10 s with 0.5 ppm. The degree of color change and saturation time was plotted in Figure 4.8. The final intensified color change values as shown in Figure 4.8a remain stable with various ratio of two polymers. Therefore, the stabilized discoloration value is mainly determined by the dye concentration rather than the polymer ratio. It can be found in Figure 4.8b that the maximum response time which is defined as the time taken to reach 90% of the maximum color change, is proportional to the increase in the PDMS ratio. This is attributed to the increase of fiber diameter and non-porous membrane formation for ratio 1:3 and 1:4. Thus, these results demonstrate that BPB dye and dual polymer nanofibers-based sensors have capability to detect the presence of ammonia through change in color depending on the analyte concentration and exposure time.

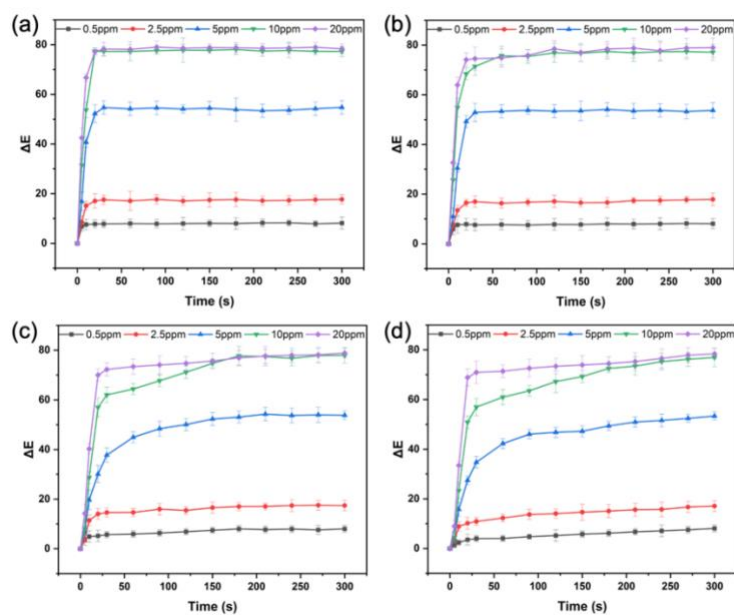


**Figure 4.7** Time-dependent color change of bi-polymer sensor with different ratio of PDMS to PCL (a) R1-1:1, (b) R2-2:1, (c) R3-3:1, (d) R4-4:1, when exposed to various concentration of ammonia.

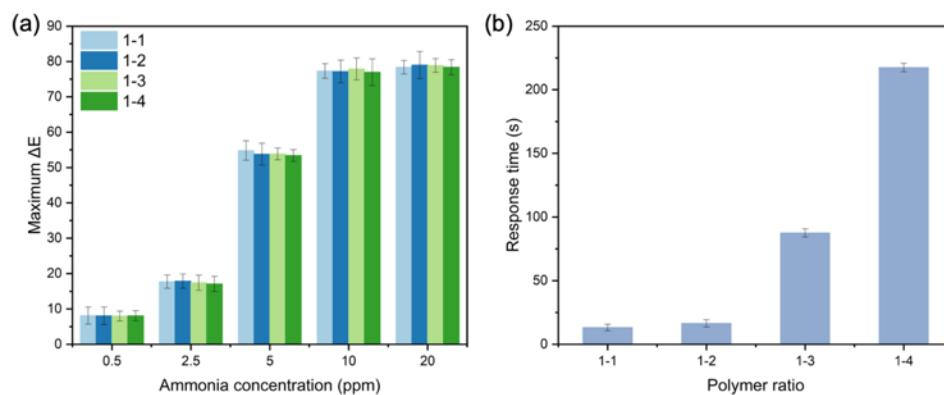


**Figure 4.8** (a) Maximum color change of samples with polymer ratio from 1:1 to 1:4. (b) Maximum response time of samples with polymer ratio from 1:1 to 1:4.

To evaluate the detection range of the BPB-bi-polymer sensor with various configurations, the 100ppm concentration of ammonia was introduced to the test chamber and the instantaneous value of  $\Delta E$  was recorded dynamically. The color of the sensor gradually changed from yellow to blue and then intensified as the ammonia concentration increased, and  $\Delta E$  was plotted accordingly in Figure 4.9a. Sensors with different ratio of PDMS was exposed to gaseous ammonia resulting in various performance. All samples reached the maximum  $\Delta E$  value below 50ppm. For 1:1 sample, the the range over which color change occurs was 0-5ppm, followed by a saturated plateau in the region after 7 ppm. The low detected concentration is highly beneficial in the practical circumstances during daily usage considering limits of human exposure by OSHA and other safety issues. The significant increasing when the sensor encountered ammonia gas indicates that ammonia detection is more effective with a steep slope of the curve especially for the samples with low ratio because the sensitivity of the detection process corresponds to the slope of the curve. The highly sensitivity can be attributed to the geometry and surface area of sensor where the fibers having lower thickness of the PDMS have a faster response time. In contrast, as the PDMS thickness increases, the slope is less providing an expanded detection range. Even though the range is enlarged by 73.3%, 76.5% and 80.1% for 1:2-1:4 samples, the sensitivity of 1:3 and 1:4 samples were smaller than the 1:1 or 1:2 samples due to their non-porous structure and thicker PDMS coating. Therefore, sample with PDMS-PCL ratio 2:1 is the best configuration with adequate extended detection range without remarkable compromise of sensitivity. The LOD of sample with ratio 2:1 was calculated to be 0.7 ppm. Additionally, a combination of sensors with different ratios can be used to provide a comprehensive colorimetric platform with high sensitivity, and a broad detection range.

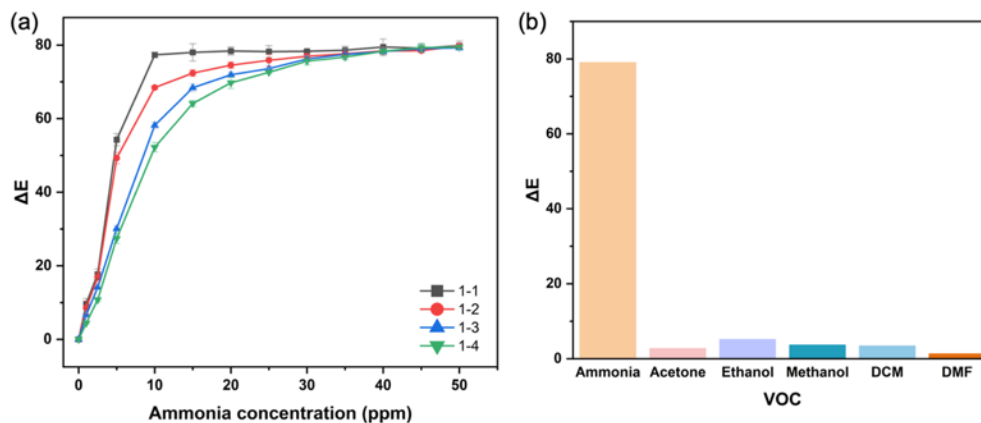


**Figure 4.9** (a) Concentration dependent color change of bi-polymer sensor with different ratio of PDMS to PCL. (b) The color change ( $\Delta E$ ) of bi-polymer sensor to different VOCs exposure.

### 3.4 Detection selectivity and interference performance of colorimetric ammonia sensor

We investigated the selectivity of the bi-polymer colorimetric sensor to explore the capability of selective detection of  $\text{NH}_3$  against many common volatile organic solvents found in industrial settings. The sensors were exposed to over 100 ppm vapor concentration of ethanol, acetone, methanol, DCM, DMF by evaporation from liquid phase within a closed container. The magnitude of color changes  $\Delta E$  were recorded and reported in Figure 4.9b.  $\Delta E$  of VOCs were distributed in the range of 1.3 to 5.1 which were more than 15 times smaller than the response of sensor exposed to ammonia. Even though the proposed sensor can solve most of interference, the other acidic vapor compound (e.g. Acetic acid) will also cause the reaction, however the BPB is acidic based pH sensitive dye which will not change color significantly with acidic vapor. In this case, there will not be a misleading of sensor response. The highly selective performance of the sensor is due to the fact that BPB is not deprotonated in non-aqueous reagents. This indicates that this dual polymer sensor has a good selectivity for gaseous interferences.

We also tested the effect of humidity on response of the bi-polymer sensor, the results of which are shown in Figure 4.10. In this experiment, we exposed a subset of sensors with various dye concentration to air with RH of 0%, 30%, 50%,  $95 \pm 5\%$  at  $24\text{ }^{\circ}\text{C}$  for 30 minutes using an environmental chamber (ESPEC North America Inc., ESL-2CW). The color change response of bi-polymer sensor was in the range of 2.6 to 4.9 over this large range of humidity (20-95%) that is typically encountered in the environment. In comparison, the response caused by humidity change was only up to 5% compared to its response to exposure to 20 ppm ammonia. This result shows that the response of the bi-polymer sensor to humidity changes is minimal due to the presence of a protective sheath of PDMS on top of the sensitive layer, making it suitable for practical applications.

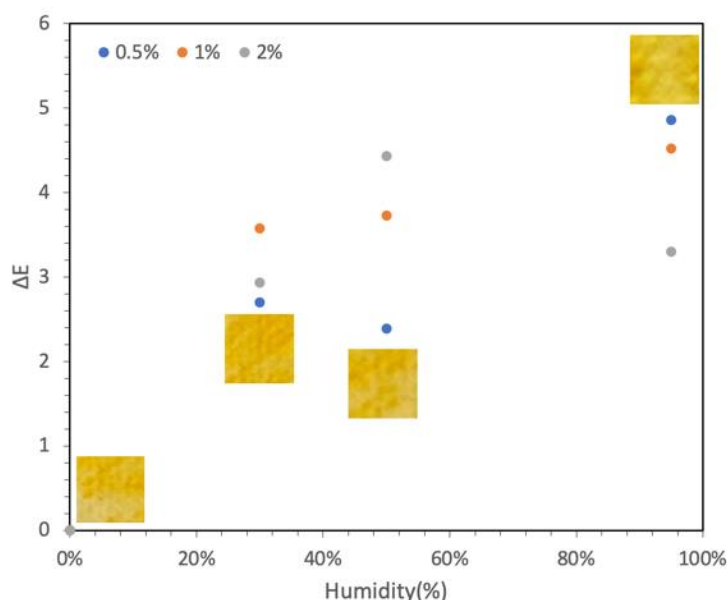


**Figure 4.10** Humidity dependence (from 0%, 30%, 50% up to 95%) of sensor response with different dye concentration from 0.5% to 2%. The inserts are the optical images of sensor with 1% dye concentration exposed to various relative humidity levels.

Besides gas interferences, we also evaluated the selectivity of the bi-polymer sensor for liquid interference. As shown in Figure 4.11, drops of basic pH buffer (pH = 12) were placed on the surface of the single polymer and the bi-polymer sensor with varying dye concentrations. The captured optical images indicate that the single-polymer PCL electrospun sensor immediately displayed a significant color change, while the bi-polymer sensor remained bright yellow for 5 minutes regardless of the concentration of the dye. Interfering liquids with high pH values were selected because for BPB dye-based sensors are responsive pH sensors and deprotonate at high pH conditions. This clearly shows that the bi-polymer sensor with PDMS coating has excellent robustness against liquid interference, which is not offered by single polymer (PCL) nanofiber-based sensors. Similarly, aerosolized spray of liquid with high pH also demonstrated a color change response with PCL electrospun layer infused with the dye. Due to the good water resistance and ion impermeability of PDMS, all PCL nanofibers encapsulated by it were not directly exposed to high pH solution [28]. This particularly important in PPEs such as face masks where the pH of the human breath is slightly alkaline and can be in the range of 5-8 and the colorimetric dyes for ammonia sensing such as BCB have a color change in the same range.

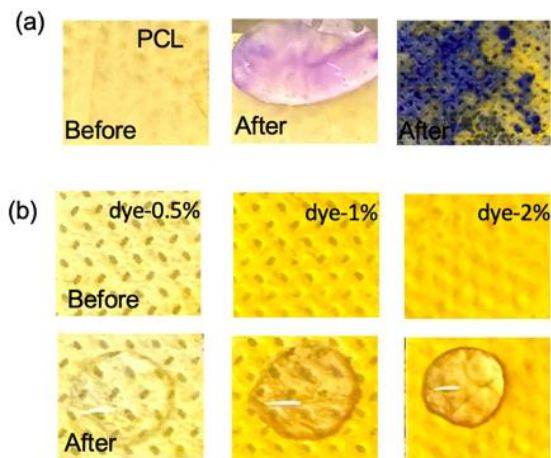


**Figure 4.11** (a) Optical photograph of the sensor exposed to liquids with high pH solution of (a) bare PCL sensor and (b) bi-polymer sensor with various dye ratio samples.

### 3.5 Reversibility performance of colorimetric ammonia sensor

To assess the reversibility of the sensing process, the bi-polymer sensor was subjected to four replicate measurements of 20 ppm ammonia exposure for 1 minutes and up to 4 minutes for stabilization of the reading followed by a 30-minute recovery period. The calculated maximum  $\Delta E$  value was  $78.2 \pm 1.5$  for four repeated cycles. It can be noticed that the response of the sensor is almost identical in the multi-cycle tests. These similar peak value of  $\Delta E$  indicates the stable and robust response of sensor with multi-usage. The protonation reaction conducted by BPB leads to a change in the color of the sensor from blue to yellow after air exposure. The recovery time is marginally affected by PDMS due to the high air permeability of the PDMS in the dual polymer sensor. As a result, our colorimetric bi-polymer sensors demonstrate robust and stable reversibility for multiple uses with a recovery time of 30 minutes.

#### **4. Conclusion**

In this paper, we reported a novel one-step, bi-polymer colorimetric ammonia sensor consisting of electrospun nanofiber encapsulated pH indicator. The core-shell biopolymer nanofiber mat was produced based on single nozzle electrospinning setup. This sensor has naked eye readable sensitivity with ammonia exposure with 0.5 ppm level, fast reaction time within 10 s, and reversibility. Our sensors can be incorporated into nonwoven-based PPE in one electrospinning step, with no additional procedure. We highlighted the durable stability of the sensor under gaseous interference of VOCs and high pH liquid interference which is necessary in combination with PPE in industrial environments. The detection range can be adjusted and extended by combining different ratios of dual polymer sensors without affecting the other performances of the sensor. PPE with integrated colorimetric sensors could potentially be equipped on workers in different industries and factories to indicate the presence of ammonia in a simple visual way.

#### **Funding**

Rong Wu would like to acknowledge the Ontario Graduate Scholarship and The Queen Elizabeth II Graduate Scholarship. We acknowledge funding from FedDev Ontario and Ontario Together Fund.

#### **Author Contributions**

Rong Wu conducted experiments, conceptualization, data analysis, validation, visualization and wrote the initial draft of the manuscript. P. Ravi Selvaganapathy supervised the project, analyzed results, and revised manuscript.

#### **Declaration of Competing Interest**

The authors declare that they have no known competing financial interests or personal relationships that could have appeared to influence the work reported in this paper.

### Acknowledgments

We also acknowledge the Centre of Excellence in Protective Equipment and Materials (CEPEM), McMaster, for the equipment.

### Reference

- [1] B. G. Ghule *et al.*, "Natural Carbonized Sugar as a Low-Temperature Ammonia Sensor Material: Experimental, Theoretical, and Computational Studies," *ACS Applied Materials & Interfaces*, vol. 9, no. 49, pp. 43051-43060, 2017/12/13 2017, doi: 10.1021/acsami.7b13122.
- [2] G. Hussain, L. Aldous, and D. S. Silvester, "Preparation of platinum-based 'cauliflower microarrays' for enhanced ammonia gas sensing," *Analytica Chimica Acta*, vol. 1048, pp. 12-21, 2019/02/07/ 2019, doi: <https://doi.org/10.1016/j.aca.2018.09.055>.
- [3] B. Timmer, W. Olthuis, and A. v. d. Berg, "Ammonia sensors and their applications—a review," *Sensors and Actuators B: Chemical*, vol. 107, no. 2, pp. 666-677, 2005/06/29/ 2005, doi: <https://doi.org/10.1016/j.snb.2004.11.054>.
- [4] Y. Zeng *et al.*, "Enhanced ammonia sensing performances of Pd-sensitized flowerlike ZnO nanostructure," *Sensors and Actuators B: Chemical*, vol. 156, no. 1, pp. 395-400, 2011.
- [5] P.-G. Su and L.-Y. Yang, "NH<sub>3</sub> gas sensor based on Pd/SnO<sub>2</sub>/RGO ternary composite operated at room-temperature," *Sensors and Actuators B: Chemical*, vol. 223, pp. 202-208, 2016.

- [6] D. Kwak, Y. Lei, and R. Maric, "Ammonia gas sensors: A comprehensive review," *Talanta*, vol. 204, pp. 713-730, 2019.
- [7] X. Guo *et al.*, "A portable sensor for in-situ measurement of ammonia based on near-infrared laser absorption spectroscopy," *Optics and Lasers in Engineering*, vol. 115, pp. 243-248, 2019.
- [8] P. K. Sekhar and J. S. Kysar, "An electrochemical ammonia sensor on paper substrate," *Journal of The Electrochemical Society*, vol. 164, no. 4, p. B113, 2017.
- [9] Z. Bielecki, T. Stacewicz, J. Smulko, and J. Wojtas, "Ammonia Gas Sensors: Comparison of Solid-State and Optical Methods," *Applied Sciences*, vol. 10, no. 15, 2020, doi: 10.3390/app10155111.
- [10] A. Piriya V.S, P. Joseph, K. Daniel S.C.G, S. Lakshmanan, T. Kinoshita, and S. Muthusamy, "Colorimetric sensors for rapid detection of various analytes," *Materials Science and Engineering: C*, vol. 78, pp. 1231-1245, 2017/09/01/ 2017, doi: <https://doi.org/10.1016/j.msec.2017.05.018>.
- [11] T. A. Khattab, S. Dacrory, H. Abou-Yousef, and S. Kamel, "Smart microfibrillated cellulose as swab sponge-like aerogel for real-time colorimetric naked-eye sweat monitoring," *Talanta*, vol. 205, p. 120166, 2019/12/01/ 2019, doi: <https://doi.org/10.1016/j.talanta.2019.120166>.
- [12] P. A. Gale and C. Caltagirone, "Fluorescent and colorimetric sensors for anionic species," *Coordination Chemistry Reviews*, vol. 354, pp. 2-27, 2018/01/01/ 2018, doi: <https://doi.org/10.1016/j.ccr.2017.05.003>.

- [13] J. Geltmeyer *et al.*, "Dye modification of nanofibrous silicon oxide membranes for colorimetric HCl and NH<sub>3</sub> sensing," *Advanced Functional Materials*, vol. 26, no. 33, pp. 5987-5996, 2016.
- [14] H. J. Oh *et al.*, "Washable Colorimetric Nanofiber Nonwoven for Ammonia Gas Detection," *Polymers (Basel)*, vol. 12, no. 7, Jul 16 2020, doi: 10.3390/polym12071585.
- [15] D. Gonçalves, "Preparation and characterization of cellulose paper/polypyrrole/bromophenol blue composites for disposable optical sensors," *Open Chemistry*, vol. 14, no. 1, pp. 404-411, 2016, doi: doi:10.1515/chem-2016-0043.
- [16] A. Alshoabi and S. Islam, "Synthesis and characterization of bromophenol blue encapsulated silica and silica-titania nanocomposites for detection of volatile organic vapors," *Physica B: Condensed Matter*, vol. 614, p. 413026, 2021/08/01/ 2021, doi: <https://doi.org/10.1016/j.physb.2021.413026>.
- [17] W. Han *et al.*, "Fabrication of nanofibrous sensors by electrospinning," *Science China Technological Sciences*, vol. 62, no. 6, pp. 886-894, 2019.
- [18] Z. Pang, J. Fu, L. Luo, F. Huang, and Q. Wei, "Fabrication of PA6/TiO<sub>2</sub>/PANI composite nanofibers by electrospinning–electrospraying for ammonia sensor," *Colloids and Surfaces A: Physicochemical and Engineering Aspects*, vol. 461, pp. 113-118, 2014.
- [19] V. Kumar, A. Mirzaei, M. Bonyani, K.-H. Kim, H. W. Kim, and S. S. Kim, "Advances in electrospun nanofiber fabrication for polyaniline (PANI)-based chemoresistive sensors for gaseous ammonia," *TrAC Trends in Analytical Chemistry*, vol. 129, p. 115938, 2020.

- [20] X. Wang, Y. Si, J. Wang, B. Ding, J. Yu, and S. S. Al-Deyab, "A facile and highly sensitive colorimetric sensor for the detection of formaldehyde based on electro-spinning/netting nano-fiber/nets," *Sensors and Actuators B: Chemical*, vol. 163, no. 1, pp. 186-193, 2012/03/01/ 2012, doi: <https://doi.org/10.1016/j.snb.2012.01.033>.
- [21] A. T. Hoang, Y. B. Cho, J.-S. Park, Y. Yang, and Y. S. Kim, "Sensitive naked-eye detection of gaseous ammonia based on dye-impregnated nanoporous polyacrylonitrile mats," *Sensors and Actuators B: Chemical*, vol. 230, pp. 250-259, 2016, doi: 10.1016/j.snb.2016.02.058.
- [22] D. H. Kim *et al.*, "Colorimetric Dye-Loaded Nanofiber Yarn: Eye-Readable and Weavable Gas Sensing Platform," *ACS Nano*, vol. 14, no. 12, pp. 16907-16918, Dec 22 2020, doi: 10.1021/acsnano.0c05916.
- [23] W. Mokrzycki and M. Tatol, "Color difference Delta E - A survey," *Machine Graphics and Vision*, vol. 20, pp. 383-411, 04/01 2011.
- [24] D. Kai *et al.*, "Elastic poly ( $\epsilon$ -caprolactone)-polydimethylsiloxane copolymer fibers with shape memory effect for bone tissue engineering," *Biomedical Materials*, vol. 11, no. 1, p. 015007, 2016.
- [25] H. Niu, H. Wang, H. Zhou, and T. Lin, "Ultrafine PDMS fibers: preparation from in situ curing-electrospinning and mechanical characterization," *RSC Advances*, 10.1039/C4RA00232F vol. 4, no. 23, pp. 11782-11787, 2014, doi: 10.1039/C4RA00232F.
- [26] J. Yang, Q. Zhou, K. Shen, N. Song, and L. Ni, "Controlling nanodomain morphology of epoxy thermosets templated by poly(caprolactone)-block-poly(dimethylsiloxane)-block-

poly(caprolactone) ABA triblock copolymer," *RSC Adv*, vol. 8, no. 7, pp. 3705-3715, Jan 16 2018, doi: 10.1039/c7ra12826f.

- [27] S. Hamouni, O. Arous, D. Abdessemed, G. Nezzal, and B. Van der Bruggen, "Alcohol and Alkane Organic Extraction Using Pervaporation Process," *Macromolecular Symposia*, vol. 386, no. 1, 2019, doi: 10.1002/masy.201800247.
- [28] P. Bian, Y. Wang, and T. J. McCarthy, "Rediscovering Silicones: The Anomalous Water Permeability of "Hydrophobic" PDMS Suggests Nanostructure and Applications in Water Purification and Anti-Icing," (in eng), *Macromol Rapid Commun*, vol. 42, no. 5, p. e2000682, Mar 2021, doi: 10.1002/marc.202000682.

#### Appendix 4 Supplementary Information

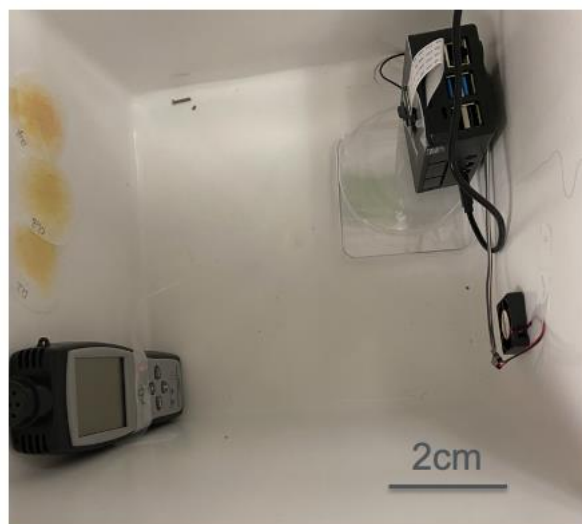


**Figure S4.1** Photograph of the chamber for sensor response monitoring.

## **Chapter 5 Highly conductive superhydrophobic laser-induced porous hierarchical graphene film from polycarbonate and applications**

Rong Wu<sup>a</sup>, Mehraneh Tavakkoli Gilavan<sup>b</sup>, Md Ali Akbar<sup>c</sup>, Liang Fan<sup>d</sup>, P. Ravi Selvaganapathy\*<sup>a,b</sup>

<sup>a</sup> *Department of Mechanical Engineering, McMaster University, 1280 Main St W, Hamilton L8S 4L8, Canada*

<sup>b</sup> *School of Biomedical Engineering, McMaster University, 1280 Main St W, Hamilton L8S 4L8, Canada*

<sup>c</sup> *Department of Chemistry and Chemical Biology, McMaster University, 1280 Main St W, Hamilton L8S 4L8, Canada*

<sup>d</sup> *College of Environmental Science and Engineering/Sino-Canada R&D Centre on Water and Environmental Safety, Nankai University, Tianjin 300350, China*

\*Authors to Whom Correspondence Should Be Addressed

E-mail : selvaga@mcmaster.ca

**Status:** In preparation

**Contribution:** This chapter focus on the wearer’s physiological condition-glucose monitoring sensor which further fulfill the function of PPE. It is necessary for special working industry like mining or under water operation. Instead of attaching sensing material, we developed a one-step fabrication method of both sensing and electrode material on Polycarbonate which is widely used in PPE field. The fabricated sensor demonstrated excellent glucose sensing performance and it eased the complexity for adhesion and sensor integration.

## 1. Introduction

Three-dimensional (3D) graphene has been widely investigated in many fields including energy storage, sensors, biomedical devices, water treatment because of its high electrical and thermal conductivity, large surface area, excellent thermal and chemical stability, as well as its adequate mechanical robustness and biocompatibility[1-5]. Conventional synthesis methods of 3D graphene commonly involve high temperature processing, mechanical and chemical exfoliation, 3D printing, and chemical vapor deposition process[6-8]. However, those methods are limited by the complex synthesis steps, high cost, and extreme processing conditions. Recently, laser-assisted processing has been found to directly form porous 3D graphene from commercial polyimide (PI) polymer, and also from polytetrafluoroethylene, polysulfone, poly(ether sulfone) and poly(ether imide)[9-11]. The CO<sub>2</sub> infrared laser can readily convert sp<sup>3</sup> to sp<sup>2</sup> carbon bonds resulting in the formation of laser induced graphene (LIG). The LIG offers advantages such as cost-effectiveness, environmental friendliness, rapid and robust one-step processing. Additionally, the laser irradiation enables roll to roll manufacturing of graphene which will significantly improve its production throughput. Based on those remarkable benefits, LIG has been successfully incorporated as supercapacitors, electrocatalysts, biosensors, and other environmental applications [12-16]. Typically, LIG prepared from PI or other polymers in air or O<sub>2</sub> environment is superhydrophilic. It can be prepared in hydrophobic form by laser treatment in H<sub>2</sub> or Ar environment which requires specialized chambers and gas flow control [17].

Polycarbonate (PC) is an excellent engineering thermoplastic owes to its excellent mechanical property, high chemical resistance, high temperature resistance and cost-effectiveness. PC is the second most widely used thermoplastic by volume and has been applied in the fields of food

packaging, electronics, optics, vehicles, piping, and many other industries[18, 19] However, LIG generation on PC has not been demonstrated before and in fact early work showed that LIG was not generated on PC [9]. Although PC is recyclable it requires significant amount of energy and therefore often ends in landfill [20]. A way to upcycle PC into a more valuable product can potentially enhance the recycle and reuse of PC.

Here, we demonstrate the successful superhydrophobic LIG formation fabricated from PC under ambient conditions using CO<sub>2</sub> laser irradiation. To the best of our knowledge, this is the first LIG formation using Polycarbonate. The effect of various laser parameters was also evaluated. The PC-LIG showed excellent conductivity with a sheet resistance of 0.8  $\Omega$  sq<sup>-1</sup> and superhydrophobicity with contact angle as high as 175.4° by single laser scribing. Moreover, we also show the versatility of fabricated PC-LIG by incorporating in different applications. We then used the single step treatment to modify the PC-LIG with gold nanoparticles for biosensors aimed at glucose detection. The proposed sensor shows good sensitivity and linearity as AuNPs modified, non-enzymatic, LIG-based glucose sensor. The PC-LIG was found to form excellent contact electrodes for carbon nanotube films for chemiresistive detection of free chlorine in water due to their excellent electrical conductivity and chemical resistance. It's good thermal stability and thermal conductivity was used to fabricate temperature sensor and electrical heater as well. Due to its low-cost, hydrophobicity, electrical and thermal conductivities, the PC-LIG can be a cost-effective electrode material in energy, battery, medical, and environmental applications.

## **2. Materials and methods**

### **2.1 Materials**

The polycarbonate film with thickness of 0.02” and 0.125” and was obtained from McMaster-Carr,

U.S. The sodium chloride (NaCl, 99.5%, Catalog No. 447300010) and the Corning™ frosted microscope slides were purchased from Thermo Fisher Scientific, Canada. The transfer 24K triple gold leaf was procured from L.A. Gold Leaf Wholesaler, U.S. Potassium chloride (KCl), potassium hexacyanoferrate II ( $K_4[Fe(CN)_6]$ ), potassium hexacyanoferrate III ( $K_3[Fe(CN)_6]$ ), sodium hydroxide (NaOH), glucose, single-walled carbon nanotube (SWCNT) and sodium hypochlorite solution (10-15% available chlorine) was sourced from Sigma-Aldrich, Canada. Sodium bicarbonate ( $NaHCO_3$ ) was purchased from ACP chemicals. Carbon paste (Product #128-07) was purchased from Creative Materials.

## **2.2 Fabrication of LIG on PC polymer**

First, PC films were attached on the microscope slide by double side type as a weight balance. For the generation of LIG on PC films, a 40 W CO<sub>2</sub> laser as shown in Figure S5.8(10.6 μm, Glowforge Basic) was used in the air at room temperature using the scan speed ranging from 32.8 mm/s to 204 mm/s, various scan powers (16% - 60%), spot size with 0.2mm and focus height of 1.5mm and 2.5mm, respectively. An outlet provided inside the instrument is used to route the generated fumes to the fume hood exhaust and to ensure air circulation.

## **2.3 Characterization**

Scanning electron microscopy (SEM) images were collected to investigate the surface and fiber morphology of the electrospun samples using FEI Versa 3D, USA. The transmission electron microscopy (TEM) images were collected from the JEM-2100 FS microscope (JEOL, Japan). The X-ray diffraction (XRD, Bruker D8, UK) with Cu K $\alpha$  radiation ( $\lambda = 1.54 \text{ \AA}$ ) and UV-vis spectrophotometer (SpectraMax M2, USA) were performed to investigate the fabricated PC-LIG. The sheet resistance information of formed PC-LIG was carried out by Accent HL5500 Hall effect

measurement system (Nanometrics, USA). The electrochemical characterization of PC-LIG was obtained by the PalmSens electrochemical analyzer (PalmSens4, The Netherlands). The video-based, fully automated, high-speed contact angle measuring instrument OCA35 (DataPhysics Instruments GmbH, Germany) was used to obtain surface contact angles.

### **3. Results and discussion**

#### **3.1 PC-LIG formation and laser parameters optimization**

The graphene was successfully induced from polycarbonate film with laser scribing. As depicted in Figure 5.1a, a commercial PC film was irradiated using a CO<sub>2</sub> laser in ambient environment to produce LIG attached to the underlying PC polymer film. Laser with speed at 64 mm/s and power at 8 W was used to produce PC-LIG on PC in the proof-of-concept study. To investigate the surface morphology after laser treatment, we characterized the surface morphology of PC-LIG under SEM as illustrated in Figure 5.1b-c under different magnifications. We observed porous structures with flakes existed on the PC-LIG surface. Such porous structures may result from the abrupt release of gases during laser scribing, such as CO and CO<sub>2</sub>[21]. The hierarchical structure of produced graphene consists of nanosphere structures loaded micrometer flake structures, that contributes to the physical properties of PC-LIG such as hydrophobicity that will be discussed later. The high laser power used to produce PC-LIG might be the reason to further break the structure of PC and re-structured to graphene. To prove the formation of graphene, we conducted the high-resolution TEM as shown in Figure 5.1d. The HRTEM image of PC-LIG showed the clear graphene lattice fringes and the d-spacing with 0.34nm. The lattice space of PC-LIG corresponded to the distance between two neighboring (002) planes in the graphite material [9]. This in addition indicated the formation of LIG structure from PC film. Inspired by the hierarchical structure on the formed PC-

LIG, we also characterized the wettability and electric conductivity. The contact angle measurement images were shown in Figure 5.1e with 10  $\mu\text{L}$  water droplet on the corresponding PC and PC-LIG surfaces. The contact angle of PC-LIG under the setting indicated before was  $170.6^\circ \pm 8.8^\circ$  with ultra-high conductivity at  $4.61 \pm 0.33 \Omega \text{ sq}^{-1}$ . The sliding angle of PC-LIG under this condition was  $3.8^\circ$  sitting in the superhydrophobic range with excellent water repellence property. The wettability of solid surface strongly depends on both the physical surface roughness and surface chemistry[22]. The unique hierarchical structure was the domain effect to result the superhydrophobicity of PC-LIG similar with lotus leaf effect [23]. Additionally, we characterized the PC and PC-LIG with Raman spectroscopy and XRD. The produced PC-LIG provided completely different spectrum compared with PC film. The Raman spectrum of PC-LIG in Figure 5.1f showed three main characteristic peaks associated with graphene, whereas the spectrum of PC showed significantly different trend and peaks. The peak at  $\sim 1330 \text{ cm}^{-1}$  (D peak) is induced by disordered bending or defects of the  $\text{sp}^2$  carbon bonds, whereas the peak at  $\sim 1580 \text{ cm}^{-1}$  (G peak) is associated with the lattice vibration of the  $\text{sp}^2$  carbon and 2D peak at  $\sim 2660 \text{ cm}^{-1}$  originates from second order zone-boundary phonons[11, 24]. The presence of those peaks confirmed the formation of graphene from PC by laser treatment. The lattice result of graphene agreed with the XRD results as shown in Figure 5.1g. The intense peak located at  $2\theta$  in the XRD pattern centered at  $26^\circ$  (002) indicated a significant level of graphitization. The second peak located at  $2\theta = 42.8^\circ$  corresponded to the 100 graphitic crystal phase plane[25]. The importance of PC-LIG synthesis under ambient environment rests on the extensive use of PC polymers. In addition, PC polymers, in the form of films, sheets, rolls and other forms with various thicknesses and customized geometries, are readily accessible in the market. The low cost of PC polymers, less than 12.5% of the price of PI and PEI films that are commonly used to produce LIG, makes PC-LIG more cost

effective than other commercial polymers. Although PC has been previously claimed to be non-graphitized under laser, PC-LIG requires higher laser power compared to conventional LIG formation from PI or PEI films which did not fall into the tested range in the previous study[9]. We have concluded that the formation of LIG on PC films is strongly correlated to the structural features-aromatic rings in PC which is also mentioned by previous studies[9]. The laser scribing can lead to extremely high localized temperature in the target point to more than 2500 °C[9]. The energy induced could easily break the bonds following by the recombination and release of atoms. During the laser irradiation, the carbons in the aromatic rings are rearranged in the form of graphene structures with highly conductive  $sp^2$  hybrid carbon[26]. The molecular dynamic (MD) simulations in previous studies further support that the heating temperature and pressure, and duration of heat preservation from laser ensure the conversion to LIG[26, 27].

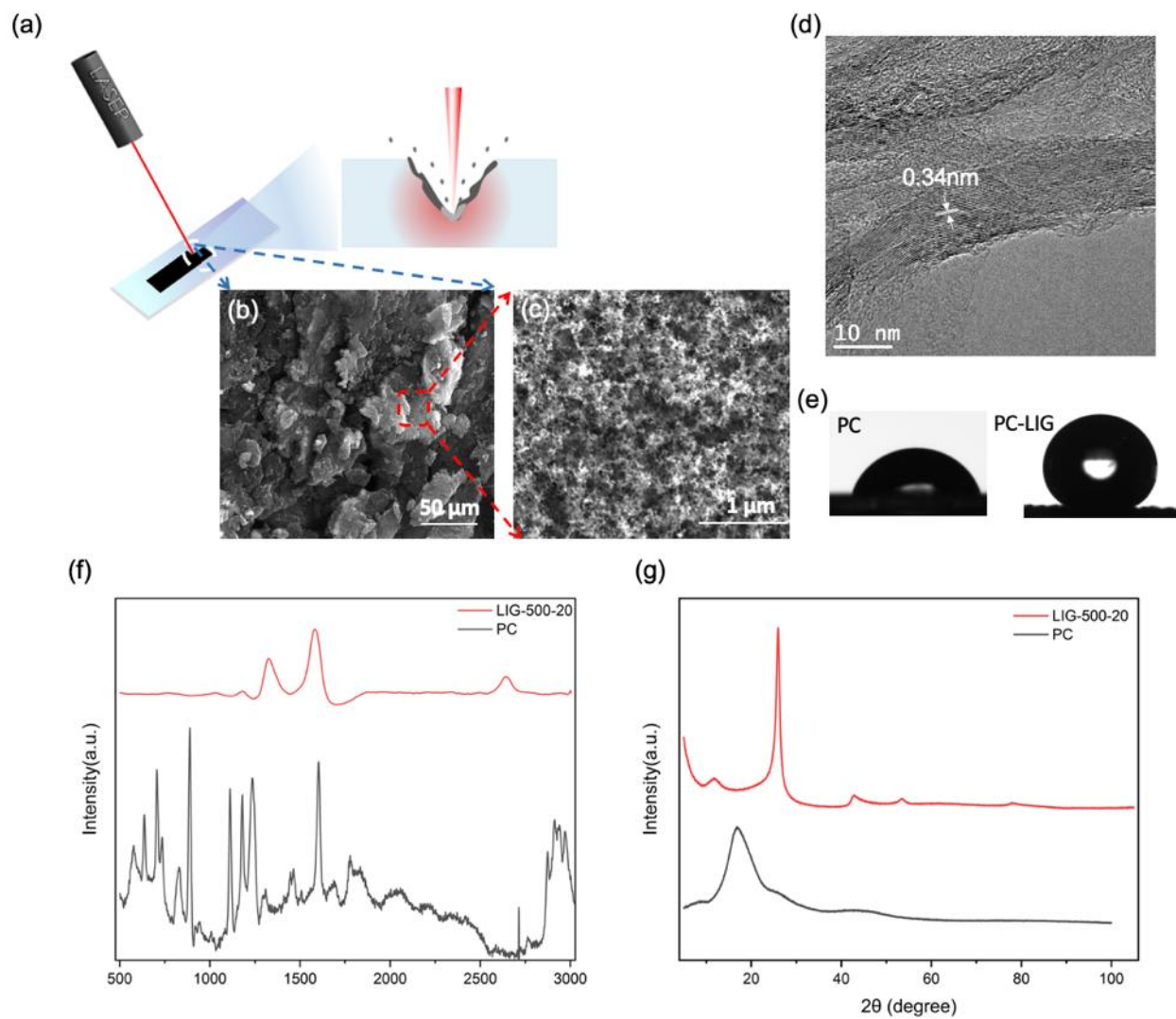


**Figure 5.1** (a) Schematic of laser irradiation on polycarbonate film; (b-c) Characterization of surface morphology of PC-LIG-500-20 under SEM with different magnifications; (d) HRTEM images PC-LIG-500-20 showing graphene crystalline; (e) Wettability of PC and PC-LIG with sessile water droplet; (f) Raman spectra of PC film and LIG-500-20; (g) XRD spectra for PC film and LIG-500-20.

Laser intensity, depending on scanning speed and laser power, is a key point in the generation of graphene on PC films. The laser fluence is proportional to the laser power and pulse duration with

the fixed effective focal area according to the formula of laser fluence in previous study[28]. The effect of laser parameters in controlling the morphology and structure of the formed material was investigated by varying the laser power setting from 4% (1.6 W) to 80% (32 W) and the scanning speed from 32.8 mm/s to 204 mm/s. the Resulting materials are termed as LIG-X-Y, where X signified the scan speed following the converting table in Table S5.1 and Y represented the laser power in percentage of full power. As shown in Figure 5.2a, PC films were not graphitized and remained non-conductive with laser parameters sitting in the light blue region. The transformation process (Figure 5.2b) includes three stages starting with engraving and surface burning, and eventually forming inherently black LIG. In the light blue un-graphitized region, the surface of PC film remained clear with laser path engraved gently. The localized temperature was elevated over the melting point of PC with increasing of laser power led to the yellow color on the surface caused by uncompleted burning and the black spot might resulted from the un-uniformed heating leading to the carbonization. The localized heat produced by laser was not enough to graphitize the PC entirely until reaching the minimum requirement of laser power at 6.4 W. After the transaction process, laser parameters in the white region represent conditions with higher energy for the successful formation of PC-LIG. Then, the LIG can be directly and readily written into different designed patterns with computer-controlled laser scribing. The results show that as the laser scanning speed increases, the laser power needs to be increased simultaneously to meet the energy requirements of graphitization on PC films. The PC-LIG can be produced in a broad range of laser power from 6.4W to 24W with various scan speed. With further increasing of laser energy, the parameters in the purple region resulted burn-out of PC films. The film was burn through with the extra high localized temperature produced by high laser power.

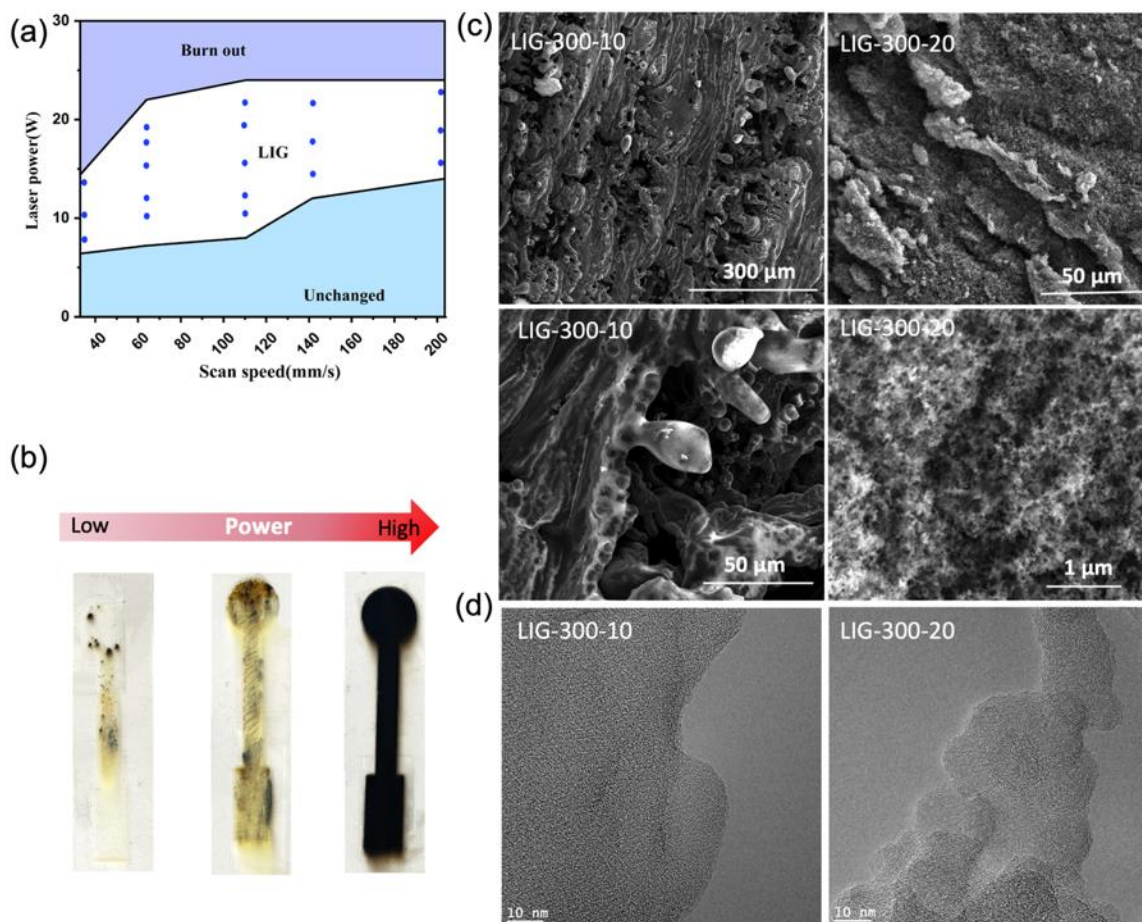


**Figure 5.2** (a) The relationship between laser scanning speeds and powers to achieve graphitization on polycarbonate film. (b) Transformation process of polycarbonate film under various laser power from low to high. (c) SEM Characterization of surface morphology of PC- under different magnification of LIG-300-10, and LIG-300-20. (d) HRTEM images of LIG-300-10, and LIG-300-20 showing graphene crystalline and amorphous carbon structures.

### 3.2 Analytical characterization of PC-LIG

To better understand the relationship between LIG creation and quality, and laser parameters, we characterized and assessed the PC-LIG based on LIG-300-10, LIG-300-20, compared to LIG-500-20 using SEM, TEM, XRD and Raman spectroscopy. The characterizations of LIG-500-20 have

been illustrated in the previous discussion. We first investigated the surface morphology of PC-LIG under SEM as illustrated in Figure 5.2c under various magnifications. We noticed that morphology of LIG-300-10 differed noticeably from LIG-300-20 and LIG-500-20 because PC films receiving 300-10 laser treatment were going through a transitional phase at the time. The 3D hierarchical porous graphene structure existed on both LIG-300-20 and LIG-500-20 samples under SEM. It can be noticed that on the LIG-300-20 there were fluffy nanostructures existed on the surface of flakes which was like the LIG-500-20. The structure on LIG-300-10 were only in micro size range resulted from the melting of PC surface. We also performed TEM characterization on the produced LIG, as depicted in Figure 5.2d and Figure S5.1 with lower magnification. Since LIG-300-10 was in the transitional stage of graphitization, many amorphous structures were found on its samples, while more crystallized structures were found under the other two conditions. Wrinkle-like flakes exhibit on the LIG- 300-20 and LIG-500-20 that is similar with PI based LIG [29]. Interestingly, there are nanosphere graphene structure produced on PC-LIG simultaneously. This might be attributed to the higher energy applied during laser irradiation, which breaks the graphene flake and forms smaller nanospheres. Similar to LIG-500-20, the clear graphene lattice fringes and same d-spacing was found under high resolution TEM of LIG-300-20 which indicated the graphene formation. The morphology of PC-LIG under TEM corresponded to SEM with both sheet-like and nanosphere-like graphene structures. Based on the observation of all three conditions, there were more amorphous structure on LIG-300-10 over crystallized graphene whereas the opposite on the samples under other two conditions. It indicated that high quality graphene was formed with higher laser power with better conversion efficiency without amorphous carbon. Therefore, the transformation process started from surface melt and burn, and then amorphous carbon formation followed by the highly graphitized LIG formation on the PC

film with increasing of laser power. The XRD spectrum as shown in Figure 5.3a matched the information from the TEM regarding to the lattice result of graphene. The more intense peak located at  $2\theta$  in the XRD pattern centered at  $26^\circ$  (002) indicated better graphitization on both LIG-300-20 and LIG-500-20, which agreed to the findings from TEM images.

To compare the quality of LIG, we performed the Raman spectroscopy on the samples with various laser conditions. The Raman spectrum of LIG-300-20, LIG-500-20 and LIG-500-40 showed three main characteristic peaks associated with graphene as shown in Figure 5.3b. Even though inherent black material formed on LIG-300-10, it can be found that the structure is more amorphous carbon over graphene without significant 2D peak. It was observed that the  $I_D/I_G$  ratio reduced from 0.79 of LIG-300-20 to 0.69 of LIG-500-40 and then 0.54 of LIG-500-20, indicating that the degree of graphene formation was enhanced with the increasing of speed and optimized laser power. The  $I_{2D}/I_G$  reached maximum of LIG-500-20, suggesting the stacking of fewest layered graphene formation[30]. The  $I_D/I_G$  ratio in Raman spectra suggested the high degree of graphene formation and  $I_{2D}/I_G$  indicated the good graphitization and high quality of graphene formation in the PC-LIG[31, 32]. Therefore, LIG-500-20 was selected and used for further studies in various applications.

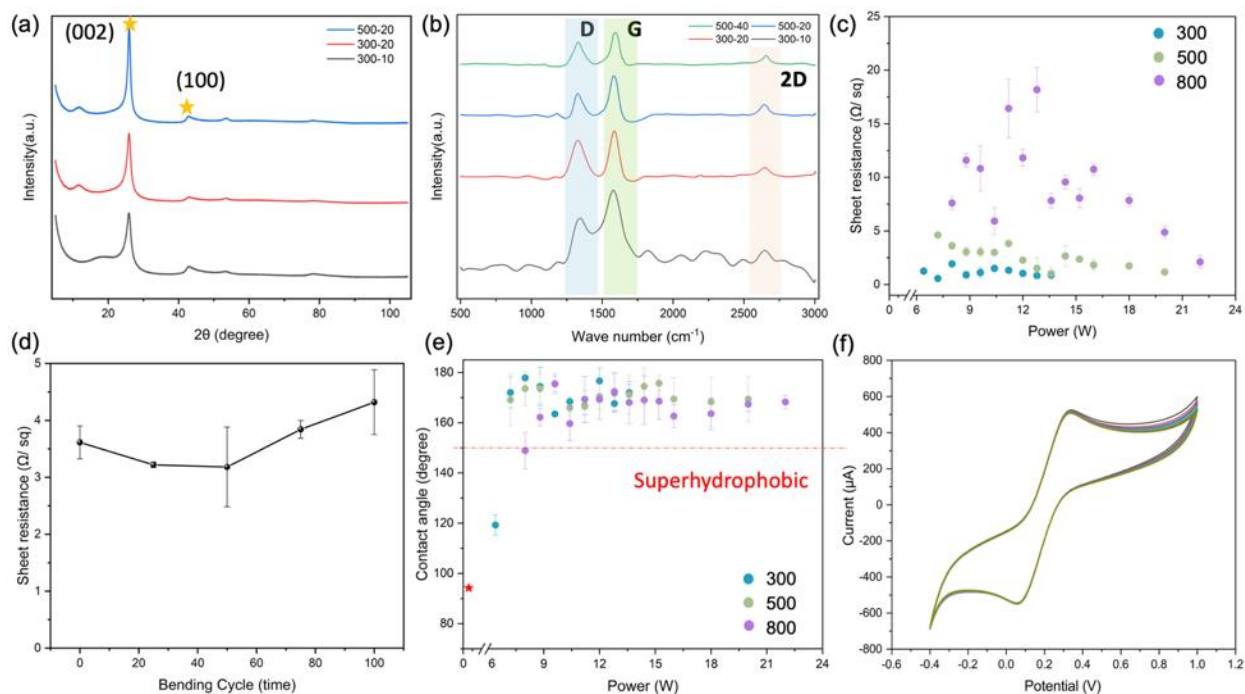


**Figure 5.3** Characterization and properties of LIG-PC produced with various laser settings. (a) XRD spectra for LIG-300-10, LIG-300-20, and LIG-500-20; (b) Raman spectra of LIG-300-10, LIG-300-20, LIG-500-20 and LIG-500-40; (c) Sheet resistance of PC-LIG under various laser parameters within graphitization range; (d) Sheet resistance change of LIG-500-20 with 100 bending cycles; (e) contact angle of PC-LIG under various laser parameters within graphitization range (f) The electrochemical CV response of LIG-500-20 sample with 10 cycles.

### 3.3 Properties of PC-LIG

Graphene has been used in tremendous applications owes to its advantageous electrical conductivity. We characterized the sheet resistant of the fabricated PC-LIG with a wide range of scan speed and laser power for further analysis, as shown in Figure 3c. The sheet resistance of PC-LIG ranged from  $0.82\text{-}18.17 \Omega \text{ sq}^{-1}$ , indicating its high conductivity with a broad range of laser parameters. The conductivity of produced surfaces highly relies on the quality of graphene and the

transformation process. It is also noteworthy that the conductivity of the PC-LIG is proportional to the scan speed. A lower scan speed allows for a longer duration of laser beam irradiation, leading to a higher local energy delivery and a better conductivity due to the transition of LIG from amorphous carbon to graphene. The sheet resistance of PC-LIG is significantly lower than that of the LIG produced from different sources in previous studies, indicating a better electrical conductivity of PC-LIG [33-35]. This might result from the higher power selected during the laser irradiation compared to other LIGs. To evaluate robustness against mechanical bending, we also conducted sheet resistance characterization with up to 100 bending cycles manually, as shown in Figure 5.3d. The PC-LIG remained excellent conductivity with sheet resistance at  $4.32 \pm 0.27 \Omega \text{ sq}^{-1}$  after 100 bending cycles. This indicated good flexibility and excellent conductive robustness of the produced PC-LIG. Repeat treatments on the same sample up to four times after removing the treated LIG layer were also performed, followed by the sheet resistance measurement. The results were plotted in Figure S5.2, that revealed the ability of the PC film to handle repeat treatments and maintain high conductivity. This is important in practical applications, where the top layer may wear over time and require re-treatment to form the LIG with the same performance. Thus, the one-step, low-cost PC-LIG has excellent electrical conductivity, making it suitable for applications such as electrochemical sensors, electrode material, biosensors, and other relevant fields.

Given the significance of applications such as biosensors and microfluidic channels, the surface wettability has been evaluated and depicted in Figure 5.3e. Nearly all PC-LIG samples exhibit superhydrophobic properties with contact angles higher than  $150^\circ$ , whereas PC film had a contact angle of  $94.2^\circ \pm 0.5^\circ$ , excluding the initial stage of LIG formation. The average range of contact angle of PC-LIG was  $153.5^\circ - 175.4^\circ$ . The cyclic voltammetry response of the corresponding LIG-

500-20 as working electrode versus Ag/AgCl in 5 mM Fe (CN)<sub>6</sub><sup>3-/4-</sup> containing 0.1 M KCl solutions with 50 mV s<sup>-1</sup> scan rate in Figure 5.3f. The high peak current value indicated that the hydrophobicity had nearly no effect on the electron transfer kinetics. The superhydrophobic PC-LIG formation remains unchanged regardless of laser power and scan speed, offering the flexibility to tune other properties by adjusting laser settings. In this case, the high contact angle results from the hierarchical structures on the PC-LIG sample. It should be noted that the PI-LIG is superhydrophilic with 0° of contact angle without additional treatment[36]. There were various methods developed to tune the graphene into hydrophobic and even superhydrophobic surface with contact angle including using an inert gases chamber (142° - 162°) for laser treatment, structure engraving by tuning pulse density (149.3° - 164.2) etc.[17, 37, 38]. Here, we present the PC-LIG with superior superhydrophobicity with simple one-step laser treatment in ambient air with better water repellent performance. The hierarchical structure named as ‘fluffy graphene’ was clear under SEM as shown in Figure 5.1b-c and Figure S5.3. The micro-scale flakes/layers with nano-spheres sitting on the top resulting to the superhydrophobic property of PC-LIG. This structure benefited the hydrophobicity of surface by trapping air with surface cavities as described in the Cassie-Baxter model[39]. With the existence of gas-liquid interface, the contact area of solid-liquid interface was significantly reduced resulting in greater contact angle and smaller sliding angle. The excellent superhydrophobicity has also been evaluated by dynamic water impact test as shown in Figure 5.4. The bouncing back of a water droplet on the surface of LIG-500-20 indicates the non-wetting behavior of the fabricated graphene. Moreover, we tested the durability of such wettability by immersing the LIG-500-20 sample in water over 48 hours. The surface remained the non-wetting performance continuously that supported the robustness of superhydrophobicity of PC-LIG as shown in Figure S4. The repeated test has been done after 15 days in the ambient

environment showed nearly no effect on the wettability with less than 3% variance. Therefore, the PC-LIG exists outstanding and robust superhydrophobicity with a wide range of scan speed and laser power.

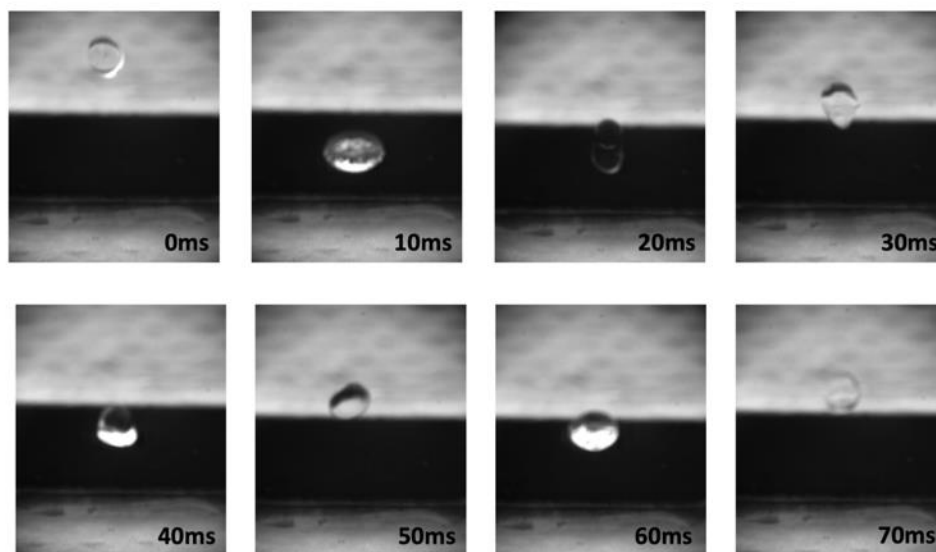


**Figure 4.** Dynamic water impact test under high-speed camera on LIG-500-20 sample showing droplet bounces.

#### 4. Applications

LIG has been widely explored and studied for a variety of applications including electrochemical sensors, piezoresistive sensors, chemiresistive sensors, environmental pollution purifications, supercapacitors, and other fields [40-44]. To demonstrate the versatility, and potential of PC-LIG, we performed the preliminary tests on various applications in different fields as shown in Figure 5.5 due to the physical properties of PC-LIG and excellent chemical resistance of PC film.

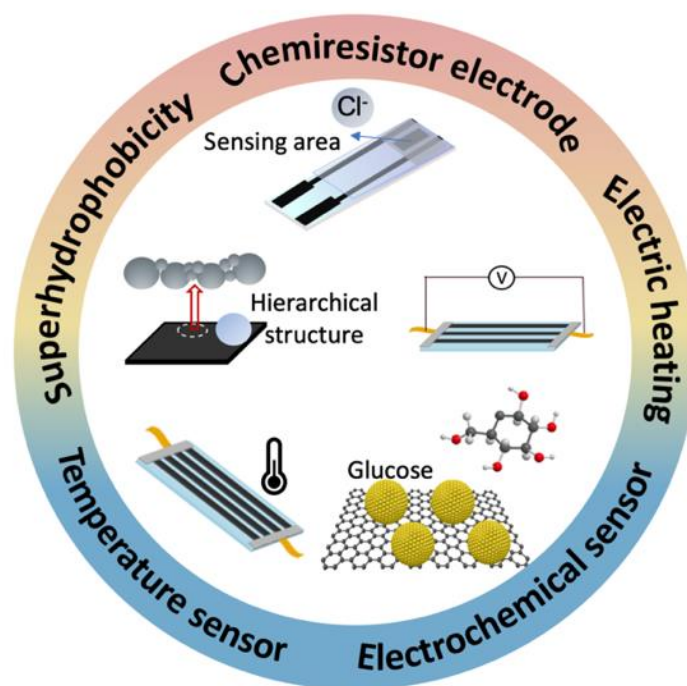


**Figure 5.5** Potential applications of PC-LIG

#### 4.1 Electrochemical glucose sensor

The combination of various functional materials is a common strategy for enhancing performance of electrochemical sensors [45]. LIG provides the suitable loading platform owing to its high specific surface area and electron transfer capability [46]. Electrochemical LIG sensors are fabricated by integration of nanomaterials to enhance the performance and introduce new functionality. Metal nanoparticles like AuNPs, AgNPs, CuNPs, PtNPs are generally incorporated to the LIG using electrochemical deposition, sputtering, chemical precursors solutions which requires complex and expensive instruments, time-consuming and strictly controlled environments [14, 47, 48]. Here, we demonstrate that the low-cost electrochemical glucose sensor can be fabricated via one-step, solid-state laser irradiation on metal film covered PC films. The fabrication process is described in Figure 5.6a. The 24k gold leaf was transferred on the PC film

with manually rolling. The AuNPs modified PC-LIG electrode was fabricated by the CO<sub>2</sub> laser with scan speed of 64 mm/s, 8 W of the laser power with a designed area of 0.8 cm × 1.2 cm. The residual metal leaves were blown off by compressed air subsequently. Copper tape was attached on the glass substrate at the edges of AuNPs modified PC-LIG sensing area to make contact pads for testing clip contact. Finally, a parafilm film with 2.5 cm × 3 cm area aligned to the edge of Au-PC-LIG was assembled to provide coverage of copper tape. The assembled sensor was encapsulated by heat treatment at 70 °C for 20 s. The produced Au-PC-LIG was characterized by High-angle annular darkfield scanning TEM (HAADF-STEM) and EDX elements mapping as shown in Figure 5.6b-e. It has shown that the AuNPs were successfully introduced and evenly distributed on the surface of PC-LIG with average diameter of 4.8nm with one-step laser scribing. We also characterize the Au-PC-LIG under XRD as shown in Figure 5.6f. Apart from the presence of graphene peaks as discussed before, there were additional new peaks obtained located at 38.4°, 44.5° and 64.8°, corresponding to the (111), (200) and (220) crystalline planes of Au, which further confirmed the formation of AuNPs [49].

The fabricated sensor was then evaluated as non-enzymatic glucose sensor as working electrode with Ag/AgCl reference electrode (1 M KCl), and Pt counter electrode. The testing analyte used was 0.1 M NaOH solution with consecutive addition of 0.01 mM to 50 mM glucose under continuously stirring and the sensor was tested using the amperometric method with an optimized applied potential at 0.15V (Figure S5.5). Figure 5.6g-h presented the response profile of Au-PC-LIG sensor and the corresponding glucose standard curve, which showed an excellent linear relationship over the glucose concentration ranging from 0.01 mM to 10 mM with a regression equation of  $y (\mu\text{A cm}^{-2}) = 70.144x (\text{mM}) + 9.88$  and a correlation coefficient ( $R^2$ ) of 0.99. Thus, the sensitivity of the Au-PC-LIG sensor was  $70.1 \mu\text{A mM}^{-1} \text{cm}^{-2}$ . The results reveal the proposed

AuNPs loaded PC-LIG has the capability to electrocatalyse glucose oxidation at low applied potential with one-step fabrication, lower-cost, better sensitivity, comparable detection range compared with other non-enzymatic AuNPs modified LIGs[50, 51]. This might contribute to both the high conductivity of the PC-LIG and the robust integration and adhesion of AuNPs under laser compared with other methods.

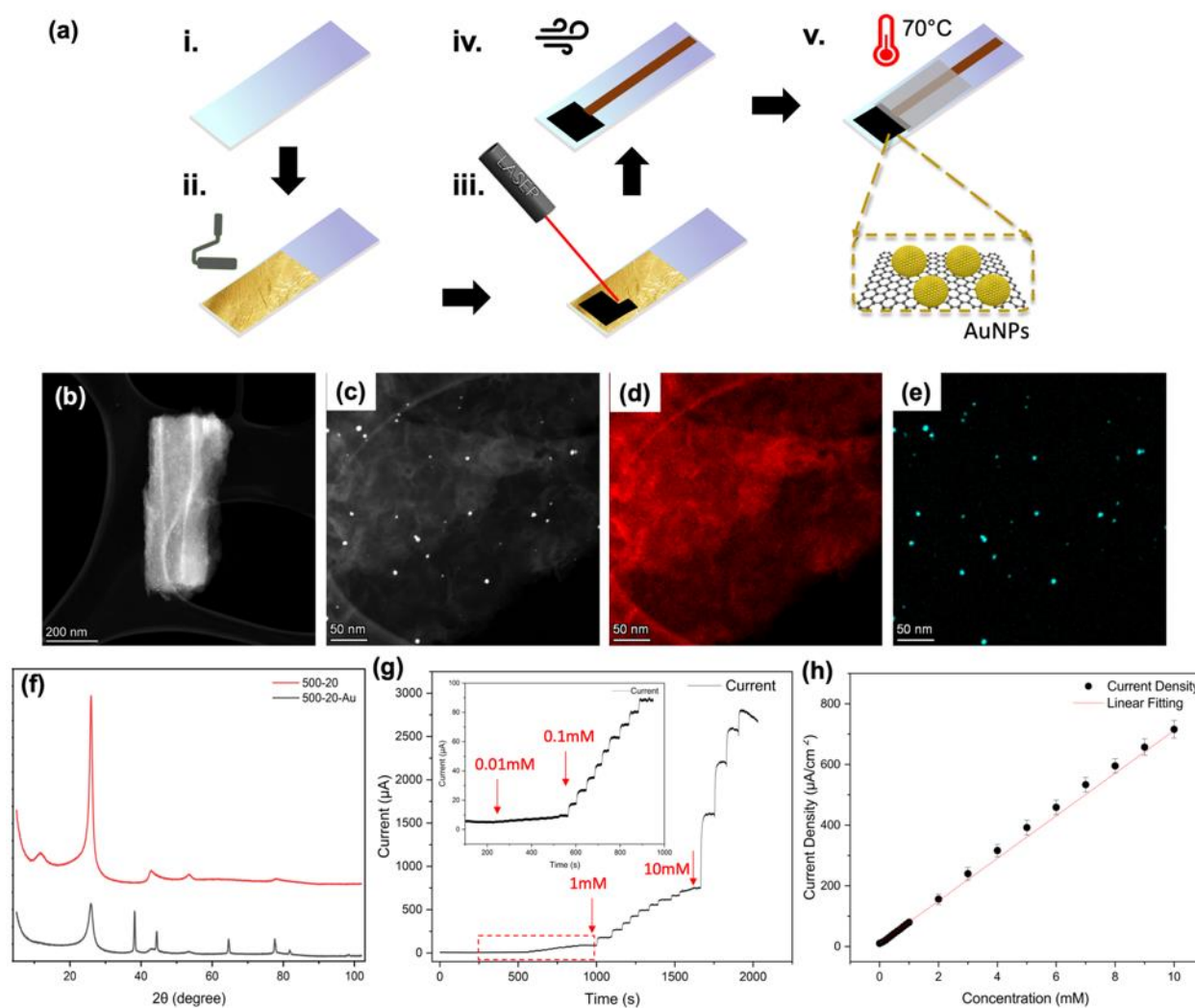


**Figure 5.6** (a) Schematic of the synthesis of PC-LIG with AuNPs for glucose sensing; (b) TEM images of Au-PC-LIG; (c) The high-resolution HAADF-STEM diagram of Au-PC-LIG and

EDX color mapping of (d) C, (e) Au; (f) XRD spectra for PC-500-20 and Au-PC-LIG; (g) Amperometric response of the Au-PC-LIG sensor to different concentrations of glucose. The inset illustrated a partial magnification of glucose measurement at low concentrations. (h) The corresponding glucose standard curve of Au-PC-LIG sensor ( $n = 3$ ).

#### **4.2 Contact electrodes for chemiresistive sensor**

Chemiresistive sensors are one type of sensor that works based on the change in electrical signals. In these types of sensors, the interaction between the sensing material and the target analytes after exposure can lead to a change in the sensor's resistance. By constantly monitoring these characteristics, the concentration of the target analyte can be measured. One of the main components of these sensors is the contact electrodes. Contact electrodes will be connected to the measurement device and are used to measure the resistance across the sensor. Unstable and poor contact can lead to noisy and unreliable responses and deteriorate the sensitivity of the sensors[52]. Metal electrodes are usually the popular option for making chemiresistive sensors. There are various studies that used gold as the contact electrode by utilizing sputter coating and lithography[53-55]. This process can be complicated, and the cost of equipment is usually very high. Screen printing is another technique to fabricate contact electrodes. Although the process is simple, the variation between different samples can be high. Also, the resistance of electrodes fabricated with this technique is higher than metal electrodes. These drawbacks can lead to low reproducibility and poor performance in these sensors.

Due to the excellent electrical conductivity of PC-LIG and chemical resistance of PC, we also evaluated the produced graphene as contact electrodes for chemiresistive sensor. First, the carbon nanotube (CNT) ink was made from 95% semiconducting SWCNTs dispersion in methanol. The

mixture was sonicated at a constant temperature for 6 hours at 80 kHz to facilitate the breakdown of the large nanotube bundles. The schematic of fabrication of sensor was illustrated in Figure 5.7a. The substrate in all the cases was polycarbonate, and contact electrodes were engraved on the surface of substrates with laser irradiation with scan speed of 64 mm/s, 8 W of the laser power. After the fabrication of contact electrodes, an airbrush pen was used to spray the CNT ink on the surface of the polycarbonate substrates. After CNT deposition, the sensors were dried at 100°C for 15 minutes to evaporate the residual methanol. Finally, a layer of parafilm film was used as the insulator for the contact electrodes to prevent shorting in measurements. The parafilm was patterned by using a bench-top cutter (Cricut) to define the sensing area of the sensors. The patterned parafilm was pressed gently to the surface at 70°C to adhere and passivate the contact electrodes. The as-prepared sensors were then tested as a free chlorine sensor. All the measurements were done with a QUAD ISOPOD e-DAQ system with 10 mV as applied potential. The instrument was set to Biosensor mode with a data acquisition rate of 30/min and a current range of 20000 nA. The background solution contained a mixture of 100 ppm sodium bicarbonate and 100 ppm sodium chloride in DI water. The sensors were immersed in the background solution for 24 hours to ensure a stable current. For the free chlorine measurements, the sensors were immersed in the background solution for 30 minutes, and then the solution was spiked with different free chlorine concentrations (range: 0.04 to 0.26 ppm). The free chlorine concentration was measured with a DR-900 colorimeter after each spike. The free chlorine solutions were prepared by diluting the sodium hypochlorite stock solution. The change in sensor response for different free chlorine concentrations was calculated based on the following equation: Eq.1:

$$\text{Sensor response} = \frac{I - I_0}{I_0} \times 100 \quad (\text{Eq. 1})$$

Where  $I_0$  is current at 0 ppm, and  $I$  is the current through the sensor after exposure to free chlorine in each step. These currents are the average of the last 30 measured points before adding the free chlorine in each step. The time between each spiking and the following measurement is 30 minutes.

Since the PC-LIG are highly conductive and stable, they are a promising candidate for contact electrodes in chemiresistive sensors. Moreover, the ability to design and engrave various patterns with the laser enables the possibility of different geometries for these sensors. Free chlorine was selected as the analyte for these sensors since it is a strong oxidizing reagent in water and its concentration needs to be monitored constantly. Figure 5.7b shows the sensor response to addition of free chlorine in each step. The sensors indicate an increase in current by increasing the free chlorine concentration, over a range of 0.04 ppm to 0.26 ppm. The sensor response for 0.04 ppm, 0.06 ppm, and 0.1 ppm free chlorine concentration is  $11 \pm 0.8\%$ ,  $17 \pm 1.2\%$  and  $20 \pm 1.5\%$  respectively. For concentrations above 0.1 ppm, the change in sensor response is not noticeable and it is around  $21 \pm 1.3\%$  and  $22 \pm 2\%$  for 0.14 ppm and 0.26 ppm of free chlorine respectively. Therefore, these sensors are an ideal candidate for concentrations lower than 0.1 ppm.

As a comparison, carbon paste was also used to make the electrodes on the polycarbonate substrate. The electrodes were fabricated by screen printing and then dried at  $70^\circ\text{C}$  for 30 minutes to remove the solvents. The measured resistance for carbon paste electrodes was  $757.13 \pm 19.82$  and for LIG electrodes was  $62.63 \pm 3.22$  and the variance in measured resistance for these electrodes was 83% higher compared to LIG electrodes. Based on the results, LIG electrodes are highly conductive and more reliable which makes them a promising candidate for fabrication of chemiresistive sensors.

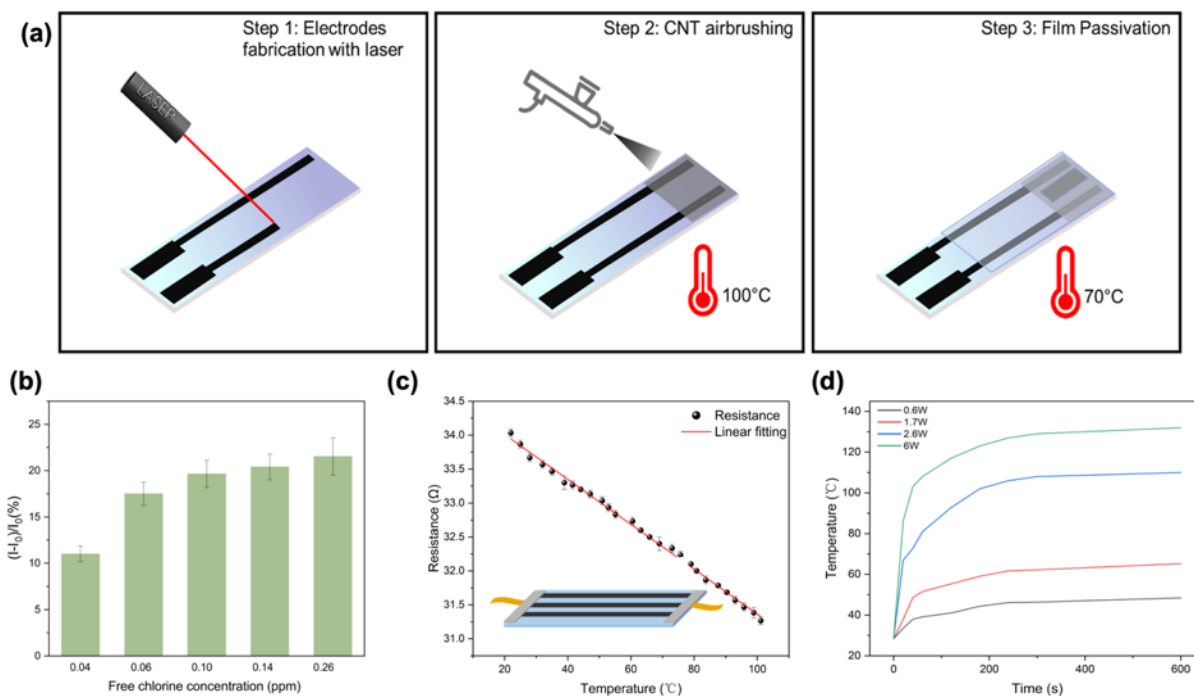


**Figure 5.7** (a) Schematic of fabrication of chemiresistive sensors on polycarbonate substrate with LIG contact electrodes and airbrushed CNT; (b) Sensor response for 5 different free chlorine concentrations (n=4); (c) The correlation between resistance and temperature of PC-LIG based temperature sensor (n=3). (d) Temperature variation of PC-LIG electrical heater under different electrical powers.

### 4.3 Others

Body temperature is an important diagnostic indicator of disease control and metabolic disorders. LIG based temperature sensor was widely used based on the correlation between temperature and resistance. The electro-phonon scattering speed and electron thermal velocity is increased with higher temperature, leading to the better conductivity of LIG [56]. LIG based sensors eased the additional step of conventional temperature sensors incorporating noble metals. Here, we selected the parallel line design for the PC-LIG based temperature sensor with copper tape as contact for

external clips connected by silver paste as shown in Figure S5.6. The temperature was evaluated by hot plate and monitored by direct touching of thermometer (Leaton, China) while the resistance was measured by the multimeter (Fluke 117, Canada). The correlation between resistance and temperature was plotted in Figure 5.7c. It can be seen clearly that the resistance response corresponding to each temperature stage was fitting with linear regression with an equation of  $y$  ( $\Omega$ ) =  $-0.033x$  ( $^{\circ}\text{C}$ ) + 34.67 and a  $R^2$  of 0.997. The PC-LIG sensor showed good linearity with wide range of detection from 22 to 100  $^{\circ}\text{C}$ . The performance of PC-LIG sensor is following the same trend of other LIG with advantages like better mechanical robustness, versatile application circumstances, and lower cost[57, 58]. Additionally, the temperature sensor was also evaluated by various humidity conditions from 0 to 90%. Interestingly, the resistance of proposed sensor rarely effected by the change of humidity. The reason is still under investigation for further study.

Due to the excellent superhydrophobicity, the fabricated PC-LIG film has the great potential to be used as membrane for water-oil separation, desalination, water treatment with antifouling property as mentioned in previous studies. Besides, the high electrical and thermal conductivity of graphene enables its possibility to be used as electrical heater. The preliminary results of the heater under different electrical powers as shown in Figure 5.7d and Figure S5.7. Based on the widely use of PC in different circumstances, functionalized the PC parts with one-step simple laser scribing will benefit from various perspectives.

## 5. Conclusion

In summary, we have successfully formed LIG from PC, a widely used polymer, through a single-step, solvent- and reagent-free laser treatment. The resulting PC-LIG exhibits excellent electrical conductivity, superhydrophobicity, thermal conductivity, chemical resistance, and robustness.

This approach offers both environmental and economic benefits, as PC can be transformed into LIG instead of being recycled. We have also demonstrated the versatility of PC-LIG as an electrochemical sensor, contact electrode, and temperature sensor. Further investigations of its potential applications in water treatment, electrical heating, biomedical, and energy fields will be conducted in future work.

### **Author Contributions**

Rong Wu conducted experiments, conceptualization, data analysis, validation, visualization and wrote the initial draft of the manuscript. Rong Wu conducted the fabrication, characterization of PC-LIG, and glucose sensor fabrication and measurement. Mehraneh Tavakkili Gilavan conducted the free chlorine sensor fabrication and measurement. Md Ali Akbar contributed to the Raman spectroscopy. Liang Fan participate in the glucose sensing measurement. P. Ravi Selvaganapathy supervised the project, analyzed results, and revised manuscript.

### **Reference**

- [1] D. Bitounis, H. Ali-Boucetta, B. H. Hong, D. H. Min, and K. Kostarelos, "Prospects and challenges of graphene in biomedical applications," *Advanced Materials*, vol. 25, no. 16, pp. 2258-2268, 2013.
- [2] Y. Sun, Q. Wu, and G. Shi, "Graphene based new energy materials," *Energy & Environmental Science*, vol. 4, no. 4, pp. 1113-1132, 2011.

- [3] M. F. El-Kady, V. Strong, S. Dubin, and R. B. Kaner, "Laser scribing of high-performance and flexible graphene-based electrochemical capacitors," *Science*, vol. 335, no. 6074, pp. 1326-1330, 2012.
- [4] S. Kabiri Ameri *et al.*, "Graphene electronic tattoo sensors," *ACS nano*, vol. 11, no. 8, pp. 7634-7641, 2017.
- [5] Y. Zhao, X.-g. Li, X. Zhou, and Y.-n. Zhang, "Review on the graphene based optical fiber chemical and biological sensors," *Sensors and Actuators B: Chemical*, vol. 231, pp. 324-340, 2016.
- [6] K. S. Novoselov *et al.*, "Electric field effect in atomically thin carbon films," *science*, vol. 306, no. 5696, pp. 666-669, 2004.
- [7] S. Stankovich, R. D. Piner, X. Chen, N. Wu, S. T. Nguyen, and R. S. Ruoff, "Stable aqueous dispersions of graphitic nanoplatelets via the reduction of exfoliated graphite oxide in the presence of poly (sodium 4-styrenesulfonate)," *Journal of Materials Chemistry*, vol. 16, no. 2, pp. 155-158, 2006.
- [8] X. Li *et al.*, "Large-area synthesis of high-quality and uniform graphene films on copper foils," *science*, vol. 324, no. 5932, pp. 1312-1314, 2009.
- [9] J. Lin *et al.*, "Laser-induced porous graphene films from commercial polymers," *Nature communications*, vol. 5, no. 1, p. 5714, 2014.
- [10] R. Ye *et al.*, "Laser-induced conversion of teflon into fluorinated nanodiamonds or fluorinated graphene," *ACS nano*, vol. 12, no. 2, pp. 1083-1088, 2018.

- [11] S. P. Singh, Y. Li, J. Zhang, J. M. Tour, and C. J. Arnusch, "Sulfur-doped laser-induced porous graphene derived from polysulfone-class polymers and membranes," *ACS nano*, vol. 12, no. 1, pp. 289-297, 2018.
- [12] C. M. Tittle, D. Yilman, M. A. Pope, and C. J. Backhouse, "Robust superhydrophobic laser-induced graphene for desalination applications," *Advanced Materials Technologies*, vol. 3, no. 2, p. 1700207, 2018.
- [13] H. Wang *et al.*, "In situ synthesis of molybdenum carbide nanoparticles incorporated into laser-patterned nitrogen-doped carbon for room temperature VOC sensing," *Advanced Functional Materials*, vol. 31, no. 46, p. 2104061, 2021.
- [14] Z. You *et al.*, "Laser-induced noble metal nanoparticle-graphene composites enabled flexible biosensor for pathogen detection," *Biosensors and Bioelectronics*, vol. 150, p. 111896, 2020.
- [15] C. Zhang *et al.*, "High-energy all-in-one stretchable micro-supercapacitor arrays based on 3D laser-induced graphene foams decorated with mesoporous ZnP nanosheets for self-powered stretchable systems," *Nano Energy*, vol. 81, p. 105609, 2021.
- [16] J. Zhang, M. Ren, L. Wang, Y. Li, B. I. Yakobson, and J. M. Tour, "Oxidized laser-induced graphene for efficient oxygen electrocatalysis," *Advanced Materials*, vol. 30, no. 21, p. 1707319, 2018.
- [17] Y. Li *et al.*, "Laser-induced graphene in controlled atmospheres: from superhydrophilic to superhydrophobic surfaces," *Advanced Materials*, vol. 29, no. 27, p. 1700496, 2017.

- [18] D. Wu *et al.*, "Prediction of polycarbonate degradation in natural atmospheric environment of China based on BP-ANN model with screened environmental factors," *Chemical Engineering Journal*, vol. 399, p. 125878, 2020.
- [19] C. C. Liang, C. H. Lin, T. C. Cheng, J. Shieh, and H. H. Lin, "Nanoimprinting of flexible polycarbonate sheets with a flexible polymer mold and application to superhydrophobic surfaces," *Advanced Materials Interfaces*, vol. 2, no. 7, p. 1500030, 2015.
- [20] E. Antonakou and D. Achilias, "Recent advances in polycarbonate recycling: A review of degradation methods and their mechanisms," *Waste and Biomass Valorization*, vol. 4, pp. 9-21, 2013.
- [21] S. C. Barman *et al.*, "A polyallylamine anchored amine-rich laser-ablated graphene platform for facile and highly selective electrochemical IgG biomarker detection," *Advanced Functional Materials*, vol. 30, no. 14, p. 1907297, 2020.
- [22] L. S. Hall *et al.*, "All-graphene-based open fluidics for pumpless, small-scale fluid transport via laser-controlled wettability patterning," *Nanoscale Horizons*, vol. 6, no. 1, pp. 24-32, 2021.
- [23] V. Zorba *et al.*, "Biomimetic artificial surfaces quantitatively reproduce the water repellency of a lotus leaf," *Advanced materials*, vol. 20, no. 21, pp. 4049-4054, 2008.
- [24] R. R. Soares *et al.*, "Laser-induced graphene electrochemical immunosensors for rapid and label-free monitoring of *Salmonella enterica* in chicken broth," *ACS sensors*, vol. 5, no. 7, pp. 1900-1911, 2020.

- [25] Z. Peng *et al.*, "Flexible boron-doped laser-induced graphene microsupercapacitors," *ACS nano*, vol. 9, no. 6, pp. 5868-5875, 2015.
- [26] F. M. Vivaldi *et al.*, "Three-dimensional (3D) laser-induced graphene: structure, properties, and application to chemical sensing," *ACS Applied Materials & Interfaces*, vol. 13, no. 26, pp. 30245-30260, 2021.
- [27] Y. Chen *et al.*, "UV laser-induced polyimide-to-graphene conversion: modeling, fabrication, and application," *Small Methods*, vol. 3, no. 10, p. 1900208, 2019.
- [28] Z. Wan *et al.*, "Laser induced self-N-doped porous graphene as an electrochemical biosensor for femtomolar miRNA detection," *Carbon*, vol. 163, pp. 385-394, 2020.
- [29] R. Ye, D. K. James, and J. M. Tour, "Laser-induced graphene: from discovery to translation," *Advanced Materials*, vol. 31, no. 1, p. 1803621, 2019.
- [30] Z. Sun *et al.*, "Large-area Bernal-stacked bi-, tri-, and tetralayer graphene," *Acs Nano*, vol. 6, no. 11, pp. 9790-9796, 2012.
- [31] M. A. Pimenta, G. Dresselhaus, M. S. Dresselhaus, L. G. Cançado, A. Jorio, and R. Saito, "Studying disorder in graphite-based systems by Raman spectroscopy," *Physical Chemistry Chemical Physics*, 10.1039/B613962K vol. 9, no. 11, pp. 1276-1290, 2007, doi: 10.1039/B613962K.
- [32] A. C. Ferrari *et al.*, "Raman spectrum of graphene and graphene layers," *Physical review letters*, vol. 97, no. 18, p. 187401, 2006.
- [33] B. Kulyk *et al.*, "Laser-induced graphene from paper for mechanical sensing," *ACS Applied Materials & Interfaces*, vol. 13, no. 8, pp. 10210-10221, 2021.

- [34] R. Ye *et al.*, "Laser-induced graphene formation on wood," *Advanced Materials*, vol. 29, no. 37, p. 1702211, 2017.
- [35] B. Chen *et al.*, "Tuning the structure, conductivity, and wettability of laser-induced graphene for multiplexed open microfluidic environmental biosensing and energy storage devices," *ACS nano*, vol. 16, no. 1, pp. 15-28, 2021.
- [36] R. Ye, D. K. James, and J. M. Tour, "Laser-induced graphene," *Accounts of chemical research*, vol. 51, no. 7, pp. 1609-1620, 2018.
- [37] J. Nasser, J. Lin, L. Zhang, and H. A. Sodano, "Laser induced graphene printing of spatially controlled super-hydrophobic/hydrophilic surfaces," *Carbon*, vol. 162, pp. 570-578, 2020.
- [38] J. Zhu, X. Huang, and W. Song, "Physical and chemical sensors on the basis of laser-induced graphene: mechanisms, applications, and perspectives," *ACS nano*, vol. 15, no. 12, pp. 18708-18741, 2021.
- [39] A. Cassie and S. Baxter, "Wettability of porous surfaces," *Transactions of the Faraday society*, vol. 40, pp. 546-551, 1944.
- [40] Y. Yu, P. C. Joshi, J. Wu, and A. Hu, "Laser-induced carbon-based smart flexible sensor array for multiflavors detection," *ACS applied materials & interfaces*, vol. 10, no. 40, pp. 34005-34012, 2018.
- [41] A. F. Carvalho *et al.*, "Laser-induced graphene strain sensors produced by ultraviolet irradiation of polyimide," *Advanced Functional Materials*, vol. 28, no. 52, p. 1805271, 2018.

- [42] W. Yan, W. Yan, T. Chen, J. Xu, Q. Tian, and D. Ho, "Size-tunable flowerlike MoS<sub>2</sub> nanospheres combined with laser-induced graphene electrodes for NO<sub>2</sub> sensing," *ACS Applied Nano Materials*, vol. 3, no. 3, pp. 2545-2553, 2020.
- [43] C. Thamaraiselvan *et al.*, "Laser-induced graphene and carbon nanotubes as conductive carbon-based materials in environmental technology," *Materials Today*, vol. 34, pp. 115-131, 2020.
- [44] A. Lamberti, F. Clerici, M. Fontana, and L. Scaltrito, "A highly stretchable supercapacitor using laser-induced graphene electrodes onto elastomeric substrate," *Advanced Energy Materials*, vol. 6, no. 10, p. 1600050, 2016.
- [45] K. Dhara, R. Thiagarajan, B. G. Nair, and G. S. B. Thekkedath, "Highly sensitive and wide-range nonenzymatic disposable glucose sensor based on a screen printed carbon electrode modified with reduced graphene oxide and Pd-CuO nanoparticles," *Microchimica Acta*, vol. 182, pp. 2183-2192, 2015.
- [46] Y. Liang, Y. Li, H. Wang, and H. Dai, "Strongly coupled inorganic/nanocarbon hybrid materials for advanced electrocatalysis," *Journal of the American Chemical Society*, vol. 135, no. 6, pp. 2013-2036, 2013.
- [47] T. Beduk, J. I. de Oliveira Filho, A. Ait Lahcen, V. Mani, and K. N. Salama, "Inherent Surface activation of laser-scribed graphene decorated with au and ag nanoparticles: Simultaneous electrochemical behavior toward uric acid and dopamine," *Langmuir*, vol. 37, no. 47, pp. 13890-13902, 2021.
- [48] Y. Zhang *et al.*, "A flexible non-enzymatic glucose sensor based on copper nanoparticles anchored on laser-induced graphene," *Carbon*, vol. 156, pp. 506-513, 2020.

- [49] X. Liu, H. Cheng, Y. Zhao, Y. Wang, and F. Li, "Portable electrochemical biosensor based on laser-induced graphene and MnO<sub>2</sub> switch-bridged DNA signal amplification for sensitive detection of pesticide," *Biosensors and Bioelectronics*, vol. 199, p. 113906, 2022.
- [50] Y. Luo *et al.*, "Stretchable and Flexible Non-Enzymatic Glucose Sensor Based on Poly(ether sulfone)-Derived Laser-Induced Graphene for Wearable Skin Diagnostics," *Advanced Materials Technologies*, vol. 7, no. 9, p. 2101571, 2022.
- [51] B. Zhu *et al.*, "Disposable and portable gold nanoparticles modified-laser-scribed graphene sensing strips for electrochemical, non-enzymatic detection of glucose," *Electrochimica Acta*, vol. 378, p. 138132, 2021.
- [52] V. Patel, P. Kruse, and P. R. Selvaganapathy, "A xurography based rapid prototyping method to fabricate low-cost and high quality metal thin film micropatterns using metal leaves," *Materials Today Communications*, vol. 30, p. 103132, 2022.
- [53] E. Hoque, L. H. Hsu, A. Aryasomayajula, P. R. Selvaganapathy, and P. Kruse, "Pencil-drawn chemiresistive sensor for free chlorine in water," *IEEE sensors letters*, vol. 1, no. 4, pp. 1-4, 2017.
- [54] L. H. Hsu, E. Hoque, P. Kruse, and P. Ravi Selvaganapathy, "A carbon nanotube based resettable sensor for measuring free chlorine in drinking water," *Applied Physics Letters*, vol. 106, no. 6, p. 063102, 2015.
- [55] L. Yang, M. Li, Y. Qu, Z. Dong, and W. J. Li, "Carbon nanotube-sensor-integrated microfluidic platform for real-time chemical concentration detection," *Electrophoresis*, vol. 30, no. 18, pp. 3198-3205, 2009.

- [56] Q. Shao, G. Liu, D. Teweldebrhan, and A. Balandin, "High-temperature quenching of electrical resistance in graphene interconnects," *Applied Physics Letters*, vol. 92, no. 20, p. 202108, 2008.
- [57] M. Marengo, G. Marinaro, and J. Kosel, "Flexible temperature and flow sensor from laser-induced graphene," in *2017 IEEE SENSORS, 2017: IEEE*, pp. 1-3.
- [58] B. Kulyk *et al.*, "Laser-induced graphene from paper by ultraviolet irradiation: humidity and temperature sensors," *Advanced Materials Technologies*, vol. 7, no. 7, p. 2101311, 2022.

**Appendix 5 Supplementary Information**

**Table S5.1** The scan speed conversion

X	Scan speed(mm/sec)
300	32.8
500	64.0
800	110.7
1000	141.8
1400	204

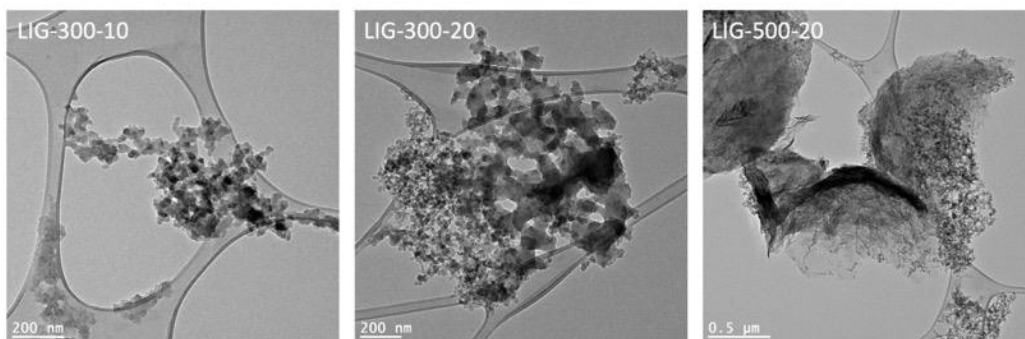


**Figure S5.1** TEM images of LIG-300-10, LIG-300-20, LIG-500-20.

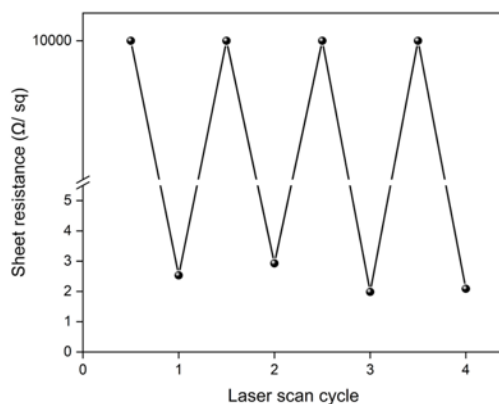


**Figure S5.2** Sheet resistance characterization of repeat treatments on same LIG-500-20 sample.

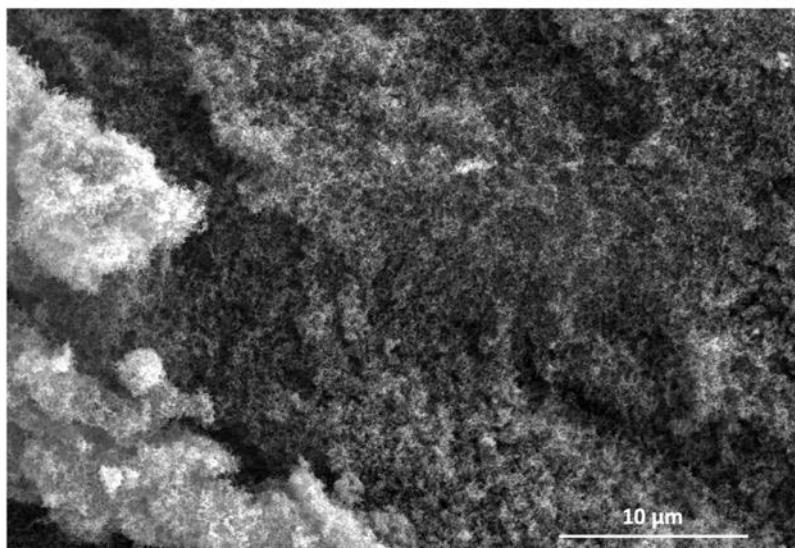


**Figure S5.3** SEM image with hierarchical fluffy graphene of LIG-500-20.

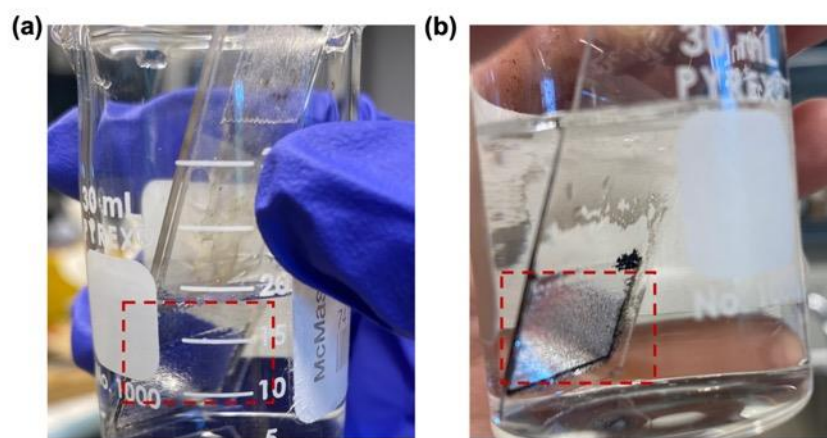


**Figure S5.4** Durability of superhydrophobicity of PC-LIG sample with (a) initial immersion in water; (b) 48 hours immersion in water. The surface of PC-LIG was covered by a clear air layer in water indicated the excellent superhydrophobicity of proposed sample.

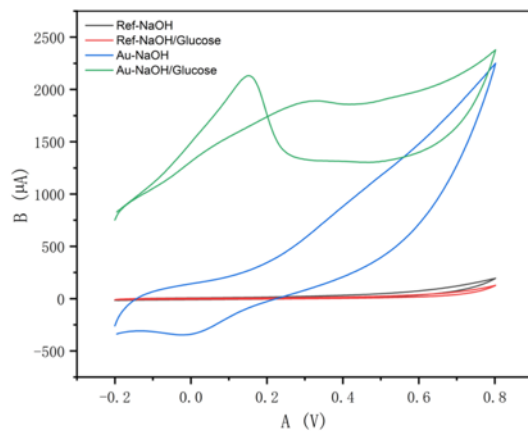


**Figure S5.5** CV response of Au-PC-LIG sensor with and without the addition of 1mM glucose in 0.1M NaOH solution.



**Figure S5.6** The parallel line design for the PC-LIG temperature sensor with copper tape connected by silver paste

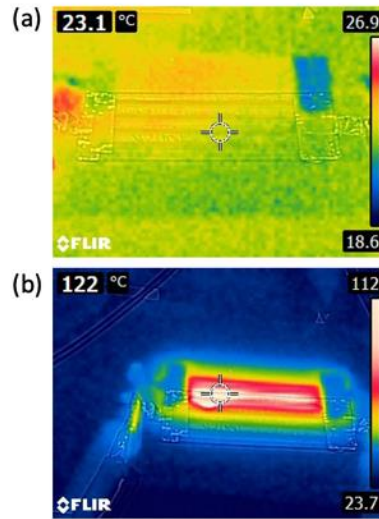


**Figure S5.7** Preliminary results of PC-LIG as electrical heater. (a-b) Temperature distribution of PC-LIG electrical heater with power supply.



**Figure S5.8** Photograph of Glowforge CO<sub>2</sub> laser machine.

## **Chapter 6 Conclusions and future direction**

### **1. Conclusions**

This thesis work was inspired by the current limitation and challenges of PPE and the importance of PPE during the COVID-19 pandemic. Here, we have demonstrated the development of new materials and manufacturing methods for next generation functional PPE. The active sensing function was achieved by two categories of sensor implementation: active protection with toxic gas-ammonia detection, and health monitoring function with glucose sensing in certain circumstances.

To provide comprehensive protection, PPEs are used as a combination such as face shield and face mask. However, both of equipment need industrial level equipment or special expertise to fabricate, which might lead to the significant shortage especially during the pandemic. A one-piece, full-head design of face shield was developed to provide sufficient filtration performance with better comfort level compared with the current state of art. Comprehensive protection could be provided by the proposed face shield instead of wearing both conventional facemask and face shield. The fitting of designed face shield was insignificantly affected by physical movement of the wearer. Additionally, this design eased the difficulty to access industrial equipment for fabrication which is important in emergency. Meanwhile, the clear exposure of full face with expressions can provide great help for the vulnerable people in our society including children, seniors, and deaf population.

For the filter material, most of commercialized filter materials are based on synthetic polymer which leads to the difficulty of disposable and recycle. Natural polymer-based filters were mainly fabricated by electrospinning. Even though the produced filter provided decent filtration efficiency, it also existed significant high pressure drop with dense micro/nanofibers. A fully-biodegradable,

plant derived biopolymer-based filter with high filtration efficiency and excellent breathability was developed. The proposed material had potential to solve the concerns of disposal and environmental implications brought by huge amount of single use devices based on non-composable synthetic polymer-based material. Cross-linked zein filter exhibited good robustness of mechanical handling and humidity. With the pleated design, the pressure drop was significantly lower than conventional electrospun filter consisted of nanofibers. This simple universal method can also be applied to other filter materials to improve the breathability without sophisticated modification.

Except of passive protection, PPE with active customized functions for various circumstances are the future direction and necessary. The next generation of PPE can not only protect users from hazardous substances exposure, but also sense the presence of such substances would be ideal to provide more comprehensive protection and monitor, For the detection of external harmful substance, we demonstrated a liquid-tolerant porous ammonia sensor with non-woven fabric substrate. The ammonia sensor was based on the core-shell bi-polymer nanofiber mat produced by single nozzle electrospinning setup with biocompatible polymers. This sensor was based on simple pH-indicator immobilization electrospun mat with naked eye readable sensitivity and was able to detect concentrations of ammonia as low as 0.5 ppm in a fast response time of 10 sec. We highlighted the long-lasting stability under gaseous interferences with volatile organic compounds and liquid interference with high pH, which is important for integration with personal protective equipment in industrial environments. By combining different ratios of dual polymer sensors, the detection range can be adjusted and extended without affecting the other properties of the sensor. PPE with integrated colorimetric sensors have the potential to be equipped to visually indicate the presence of ammonia to workers in different industries, offering full protection.

Also, the personal physiological measurements of wearers are important especially in extreme environments where immediate medical is not feasible such as in mining industry or under ocean exploration and so on. However, the integration of electrodes still remain challenging to combine with PPE. Here, we developed the glucose sensor by LIG fabrication from PC which is widely used in PPE such as face shield. The physical properties of LIG were investigated including wettability and electrical conductivity. We also showed the one-step synthetic glucose sensing platform with gold nanoparticle modified LIG. The fabricated LIG sensor demonstrated an excellent linear relationship over the glucose concentration ranging from 0.01 mM to 10 mM which fell into the glucose concentration in sweat. The proposed fabrication method solved the problem of electrode implement to the PPE by one-step directly laser writing. In conclusion, our work demonstrated next generation of PPE that is well designed, sustainable, and active in monitoring of external environmental and physiological parameters.

## **2. Future directions**

Despite the achievements of this thesis and its contribution to the field, there remains challenges that has not yet been fully solved and answered. The future research directions should focus on following few perspectives to improve the performance and fulfill more functions of next generation of PPE.

### **2.1 Functional natural polymer-based filter materials for face mask application**

Here, we proposed natural polymer-based filter material based on plant derived biopolymer zein. Other natural polymers suitable for electrospinning can also be investigated in the same manner to validate the performance. Meanwhile, incorporating nanoparticles such as silver nanoparticles is achievable by electrospinning process. The produced filter material will have the capability of

antibacterial function for long-term usage especially for usage in hospital. Also, the pleated structure was made manually which can be significantly improved by producing an automated system for automatic folding. This will improve the uniformity of pleats, throughput of filter material, and fabrication efficiency. Development of hierarchical structures to fabricate fibers with significant different dimensions can also be investigated with natural polymers. The nano-size fiber will be used to filter ultra-small size particles where micro-size fiber will be used as backbone and ensure the low pressure drop. For the application testing, a combination of natural-based filter materials and face shield design is required as next step to verify the performance. The fitting test with human wearer should be conducted to better understand the robustness of filter material and filtration performance.

## **2.2 Gas sensing**

In this thesis, the ammonia sensing platform with sensitive dye encapsulated was validated with decent performance of targeted gas. Inspired by the reaction with different ratio of PDMS, an array design with various configurations can be developed and investigated in the future work. By the sensing array, the performance will be enhanced with enlarged detection range. Meanwhile, a dose measurement platform can also be established in a mobile app format. User can easily get the precise exposure dose by the phone camera based on the logistic between color change and exposing dose. Also, there are other toxic gases that are present in other industries and circumstances. The developed bi-polymer electrospinning technique can be used by incorporating sensing materials aiming on those gases to prevent liquid interferences. The sensing performance needs to be validated with presence of harmful gases. This function can be more comprehensive

with multi-gas sensing platform which provide better detection of harmful gases and protection of wearer.

### **2.3 Physiological condition monitor**

In our work, we presented the glucose monitor with Au-PC-LIG sensor. There is another challenge about sweat collecting besides the electrode implement. The human test is necessary wearing functionalize face shield to evaluate the sweat collection situation. Except gold nanoparticles, copper and other alloy nanoparticles have shown significant high sensitivity to glucose which can be used to modify the PC-LIG by laser in the future work to enhance the performance[1, 2]. A flexible PDMS based-microfluidic hierarchical structured system can be integrated into the forehead part of face shield to extract sweat and flow to the sensing area. The volume of sweat collection also will effect the reliability of sensor. Since the microfluidic pad will directly contact with body fluid, the disinfection is also essential to reuse purpose. This could be achieved by flowing ethanol through the channel after usage or any other effective strategies. Furthermore, sensors with function to detect the other physiological parameters such as pH level, dopamine and so on can also be implemented in PPE to provide the comprehensive real-time diagnose of wearers under certain circumstances PH level in sweat also represents the health condition of human. Polyaniline (PANI) has been widely used as a pH-sensitive material since the ability to detect hydrogen ion by deprotonation[3]. The PC-LIG based electrode can be connected and modified with PANI sensing layer to achieve pH level detection in the sweat. Dopamine, as an important neurotransmitter involved in biological processing, is also very important element to be monitored. Both AuNPs and PtNPs showed the sensitive response to the dopamine in the body fluid[4]. The

interference of response to dopamine and glucose needs to be further investigated in the future study.

## Reference

- [1] X. Xuan, H. S. Yoon, and J. Y. Park, "A wearable electrochemical glucose sensor based on simple and low-cost fabrication supported micro-patterned reduced graphene oxide nanocomposite electrode on flexible substrate," *Biosensors and Bioelectronics*, vol. 109, pp. 75-82, 2018.
- [2] M. Adeel, M. M. Rahman, I. Caligiuri, V. Canzonieri, F. Rizzolio, and S. Daniele, "Recent advances of electrochemical and optical enzyme-free glucose sensors operating at physiological conditions," *Biosensors and Bioelectronics*, vol. 165, p. 112331, 2020.
- [3] S. Y. Oh *et al.*, "Skin-Attachable, Stretchable Electrochemical Sweat Sensor for Glucose and pH Detection," *ACS Appl Mater Interfaces*, vol. 10, no. 16, pp. 13729-13740, Apr 25 2018, doi: 10.1021/acsami.8b03342.
- [4] B. Patella *et al.*, "Electrochemical detection of dopamine with negligible interference from ascorbic and uric acid by means of reduced graphene oxide and metals-NPs based electrodes," *Analytica Chimica Acta*, vol. 1187, p. 339124, 2021.

